2021

Synthesis and characterization of ionic liquid electrolytes for use in electrical energy storage devices at elevated temperatures

BOSTON UNIVERSITY

GRADUATE SCHOOL OF ARTS AND SCIENCES

Dissertation

SYNTHESIS AND CHARACTERIZATION OF IONIC LIQUID ELECTROLYTES FOR USE IN ELECTRICAL ENERGY STORAGE DEVICES AT ELEVATED TEMPERATURES

by

JENNIFER CHAPMAN VARELA

B.S., Saint Mary's College of California, 2015

Submitted in partial fulfillment of the

requirements for the degree of

Doctor of Philosophy

2021

Approved by

First Reader _____

Mark W. Grinstaff, Ph.D.
Professor of Biomedical Engineering, Chemistry, Materials Science and Engineering, and Medicine

Second Reader _____

Emily Ryan, Ph.D.
Associate Professor of Mechanical Engineering and Division of Materials Science and Engineering

Third Reader _____

Linda Doerrer Ph.D.
Professor of Chemistry and Division of Materials Science and Engineering

ACKNOWLEDGEMENTS

It takes a village to raise a child and the same can be said for completing a Ph.D.; a myriad of people have offered support and guidance during my studies. First and foremost, I need to thank Prof. Mark Grinstaff, the opportunity to work on this project has been incredible. Your lab is diverse and multidisciplinary and I have learned more than I ever thought possible. I even learned about biology! I would also like to thank my committee members for their support and collaborations during this project; thank you Professors David Coker, Malika Jefferies-el, Linda Doerrer, and Emily Ryan. Access to your wide and varied expertise expanded and enriched the scientific work that I completed.

Thank you to everyone in the Grinstaff lab for being inviting and willing to brainstorm and share ideas. Both professionally and personally, everyone in the lab have been wonderful to work with, and I am glad to have gotten to know you. In particular, I would like to thank Jialiu Zeng, Ph.D., Jiaxi Song, Maria Varghese and Anant Belijepalli, Ph.D., for putting up with my singing and dancing in the lab. Thank you for always listening when I rambled about the glovebox. Thank you for being amazing labmates. Thank you to my collaborators at Samsung SAIT: Won-seok Chang, Ph.D, Lincoln Miara, Ph.D, and Chae-ah Kim, for being open and willing to answer my questions and troubleshoot. I appreciate how generous you were with your time and your offers of guidance during this process.

Lastly, I want to thank my family and friends who have supported me in every dream I have ever had. Thank you, mama and papa, for being the best parents I ever could

imagine. You always answered the phone, no matter how early in the morning, and you gave unflinching support when I announced my plans to start graduate school. Thank you to my three brothers, Jeremy, Josh, and Justin, for encouraging me to always try. Thank you, Nick Vigil and Alexandria Becker, for being the best of friends, and not giving up on our friendship even though I moved across the country. And last but not least, thank you Keith Florian and Florian Martial Art's Center for becoming a second home, passion, and life-line in the darkest moments of my life. Brazilian Jiu-Jitsu is now a part of who I will forever be, and whenever I need strength I look inwards to what I have learned from you, Keith. Thank you, all.

Jennifer, 2021

SYNTHESIS AND CHARACTERIZATION OF IONIC LIQUID ELECTROLYTES FOR USE IN ELECTRICAL ENERGY STORAGE DEVICES AT ELEVATED TEMPERATURES

JENNIFER CHAPMAN VARELA

Boston University Graduate School of Arts and Sciences, 2021

Major Professor: Mark W. Grinstaff, Ph.D., Professor of Biomedical Engineering and Chemistry

ABSTRACT

Electric energy storage (EES) devices like lithium ion batteries and supercapacitors have limited operational temperatures between 0 and 40 ^{o}C, preventing their use in demanding, high temperature applications. The principal limitation of these systems is the flammable and volatile carbonate-based solvent electrolyte. A significant barrier hindering the replacement of carbonate-based solvents is the inability to identify thermally stable solvents that display equivalent properties. Room temperature ionic liquids (RTILs) are ideal candidates to replace carbonate-based solvents to expand operational temperatures to 60 $^{\circ}$C and above. RTILs are nonvolatile, nonflammable, thermally and electrochemically stable but most RTILs do not meet current conductivity or viscosity standards to function effectively.

To this end, we generated a library of RTIL electrolytes to discover a structure-function relationship and to enable the design of RTILs with precise physiochemical properties. Modifications were made to a base RTIL structure and the resulting thermal and physical properties were evaluated. Specifically, the identity of the cation was

altered, an electronegative moiety was included, the alkyl chain lengths were varied, or different anionic components were utilized. It was found that a small anion with a delocalized negative charge when paired with an asymmetric cation generally produced a RTIL with the desired physicochemical properties.

Furthermore, RTILs were paired with anions with a delocalized negative charge and then binary, ternary, and quaternary RTIL and salt mixtures were created. The electrochemical behavior of the formulations was assessed via cyclic voltammetry and the relationship between the cation and anion of the RTIL and lithium salts was studied. The coordination strength between the anion of the lithium salt and the cation of the RTIL strongly dictated the electrochemical stability of the formulations. This highlighted the novel feature of RTILs to act both as an inert solvent and a mobile ion in an EES device.

Using the developed structure-function relationship, we fabricated two systems of supercapacitors that utilized RTIL electrolytes. The first is a piperidinium based electrolyte with a fluorinated lithium salt: the supercapacitor displayed sustained cycling for over 10,000 cycles at 100 ^{o}C with a discharge capacity of 28 F/g, while a traditional system failed after 3200 cycles. The second is a lithium free dicyanamide anion based RTIL electrolyte equipped supercapacitor. This system relies on the cations and anions of the RTIL to act as the medium of transport and as the mobile ions of the system to generate an electric double layer during charging/discharging. Our system cycled over 10,000 times at 60 ^{o}C with an average discharge capacity of 10 F/g for the last 5,000 cycles.

TABLE OF CONTENTS

LIST OF TABLES

LIST OF FIGURES

LIST OF ABBREVIATIONS

ΔV	window potential in volts
A	amp
A/g	amps per gram
AB	acetylene black
AC	activated carbon
AC_4Im	1-allyl-3-butyl-imidazolium
AC_4Im-Cl	1-allyl-3-butyl-imidazolium Chloride
AC_4Im-DCA	1-allyl-3-butyl-imidazolium dicyanamide
AC_4Im-PF_6	1-allyl-3-butyl-imidazolium hexafluorophosphate
AC_4Im-TFSI	1-allyl-3-butyl-imidazolium bis(trifluoromethanesulfonyl)imide
ACN	acetonitrile
AFM	atomic force microscopy
AgDCA	silver dicyanamide
APCI	atmospheric pressure chemical ionization source
BE	binding energies
BenzMIM-TFSI	1-benzyl-3-methylimidazolium
BMIM-BF_4	1-butyl-3-methylimidazolium tetrafluoroborate
BMP-BF_4	1-butyl-4-methylpyridinium tetrafluoroborate
C_s	discharge capacity
DCA^-	dicyanamide

DCM	dichloromethane
DFT	density functional theory
DI	deionized water
DSC	differential scanning calorimetry
E	energy density
EC	ethylene carbonate
EDL	electric double layer
EES	electrical energy storage
EMIM-FAP	1-ethyl-3-methylimidazolium tris(pentafluoroethyl)-trifluorophosphate
EMIM-TFSI	1-ethyl-3-methylimidazolium
ESI	electrospray ionization
ESW	electrochemical stability window
F/g	farad per gram
fs	full scale
$HMIM^+$	1-hexyl-3-methylimidazolium
Hz	hertz
I_{const}	constant current applied
IL	ionic liquid
J/m^3	joule per meter cubed
kcal/mol	kilocalories per mole
KCl	potassium chloride

LC/MS	liquid chromatography mass spectroscopy
LIB	lithium ion batteries
LiBOB	lithium bisoxalatoborate
LIC	lithium ion supercapacitor
LiDCA	lithium Dicyanamide
LiF	lithium fluoride
LiFSI	bis(fluorosulfonyl)imide
LiFTI	lithium (fluorosulfonyl)-(trifluoromethanesulfonyl)imide
$LiPF_6$	lithium hexafluorophosphate
LiTFSI	bis(trifluoromethanesulfonyl)imide
LTO	lithium titanate
LVR	linear viscoelastic region
m	mass
M	molar
mA	milliamp
MD	molecular dynamics
mg	milligram
MHz	megahertz
min	minute
mL	milliliter
mmol	millimole

MNIM-TFSI	1-methyl-3-nonylimidazolium bis(trifluoromethanesulfonyl)imide
mS/cm	millisiemen per centimeter
mV/s	millivolts per seconds
mV/s	millivolts per seconds
NaDCA	sodium dicyanamide
NMR	nuclear magnetic resonance
^{o}C	degree Celsius
^{o}C/min	degree Celsius per minute
OCP	open circuit potential
P	power density
P111	triethyl-propyl-phosphonium
P111-DCA	triethyl-propyl-phosphonium dicyanamide
P111-I	triethyl-propyl-phosphonium Iodide
P111-PF_6	triethyl-propyl-phosphonium hexafluorophosphate
P111-TFSI	triethyl-propyl-phosphonium bis(trifluoromethanesulfonyl)imide
P1o1	triethyl-methoxymethyl-phosphonium
P1o1-Br	triethyl-methoxymethyl-phosphonium bromide
P1o1-DCA	triethyl-methoxymethyl-phosphonium dicyanamide
P1o1-PF_6	triethyl-methoxymethyl-phosphonium hexafluorophosphate
P1o1-TFSI	triethyl-methoxymethyl-phosphonium bis(trifluoromethanesulfonyl)imide

P2F-TSFI	triethyl-3,3,3-trifluoro-propyl-phosphonium bis(trifluoro-methane-sulfonyl)imide
P2o1-TFSI	triethyl-methoxyethoxyethyl-phosphonium bis(trifluoro-methane-sulfonyl)imide
P2S-TFSI	triethyl-ethyl-methyl-sulfonyl-phosphonium bis(trifluoromethane-sulfonyl)imide
P4F-TFSI	tributyl-3,3,3-trifluoro-propyl-phosphonium bis(trifluoromethanesulfonyl)imide
P4S-TFSI	tributyl-ethyl-methyl-sulfonyl-phosphonium bis(trifluoromethane-sulfonyl)imide
P6F-TFSI	trihexyl-3,3,3-trifluoro-propyl-phosphonium bis(trifluoro-methane-sulfonyl)imide
P6S-TFSI	trihexyl-ethyl-methyl-sulfonyl-phosphonium bis(trifluoromethane-sulfonyl)imide
Pa.s	pascal seconds
PC	propylene carbonate
PF_6^-	hexafluorophosphate
$PFPB^-$	tetrakis(pentafluorophenyl)borate
ppm	parts per million
PYR_{14}-FAP	1-butyl-1-methyl-pyrrolidinium tris(pentafluoroethyl)-trifluorophosphate
PYR_{14}-TFSI	1-butyl-1-methyl-pyrrolidinium bis(trifluoromethanesulfonyl)imide
RTIL	room temperature ionic liquid
s	second
SC	supercapacitor

SEI	solid electrode interphase
SPE	solid polymer electrolyte
T_c	crystallization temperature
$TFSI^-$	bis(trifluoromethanesulfonyl)imide
T_g	glass transition temperature
TGA	thermal gravimetric analysis
THF	tetrahydrofuran
$THTDP^+$	trihexyl-tetradecylphosphonium
T_m	melting point
TTE	1,2,2-tetrafluoroethyl- 2,2,3,3-tetrafluoropropyl ether
µA	microamp
uL	microliters
um	micrometer
V	volt
Wh/kg	watt hour per kilogram
wt%	weight percent

Chapter 1: Electrode Material-Ionic Liquid Coupling for Electrochemical Energy Storage

Select sections were modified and adapted from: Wang, X.; Salari, M.; Jiang, D.; **Chapman Varela, J.**; Anasori, B.; Wesolowski, D. J.; Dai, S.; Grinstaff, M. W.; Gogotsi, Y. Electrode Material-Ionic Liquid Coupling for Electrochemical Energy Storage. *Nature Reviews Materials*. 2020, 5, 787-808.

1.1 Introduction

There is currently a strong demand for electrical energy storage (EES) devices which function with increased energy storage capacity while simultaneously providing improved safety and longer cycling stability to satisfy the growing industrial and consumer needs.[1-2] In particular, the market-dominant Li-ion batteries (LIBs) and supercapacitors (SCs) are of interest for use in automotive, mining, solar and wind energy, oil industry, military applications. Many of these applications necessitate the EES device to operate safely and efficiently at high temperatures (up to 300 °C; Fig. 1.1a) where thermal electrochemical instability lead to poor cycling and safety issues.[3]

In an EES device the electrolyte is an essential component that shuttles the ions between the positive and negative electrodes and the electrical energy storage process occurs at the interface between the electrode and the electrolyte. Typically, LIBs use an electrolyte composed of 1.0 M lithium hexafluorophosphate ($LiPF_6$) in ethylene carbonate (EC) and a linear carbonate ester: carbonate-based organic electrolytes decompose and form a Li^+-conductive solid electrolyte interphase (SEI) layer on the

graphite anode, preventing solvent co-intercalation and enabling stable operation of the battery within a 4-V window. Conventional SCs use an organic electrolyte comprised of ammonium cations and fluorinated anions in acetonitrile (ACN) that does not form a SEI layer and has a relatively narrow operating voltage window of <2.7 V. Conventional organic electrolytes fail at elevated temperatures and present safety concerns due to their high volatility and flammability and the $LiPF_6$ salt used in LIBs degrades above 55 °C, forming corrosive components, such as hydrofluoric acid.

Ionic liquids (ILs), molten salts composed of positive and negative ions, are a promising and safe alternative to conventional organic electrolytes due to their high electrochemical and thermal stability, negligible vapor pressure and non-flammability (Fig. 1.1b).[4-5] Typically, ILs exhibit high thermal stability, extending to temperatures above 300 °C. Compared with organic electrolytes, ILs exhibit superior electrochemical stability, enabling IL-based EES devices to stably operate within a wide electrochemical potential window of, in some cases, up to 6 V, providing a higher energy density.[6] The use of ILs in EES devices is currently limited for two reasons: first ILs are more expensive than organic solvent electrolytes and IL based EES devices do not yet yield high enough energy or power density to compensate the additional cost; and second the electrochemical stability of the neat ILs do not always result in an IL based EES with wide electrochemical stability due to the presence of irreversible interfacial reactions at the electrodes, especially at high temperatures. ILs also have moderately high ion transport resistance compared to organic solvent electrolytes which lowers the high-rate performance of IL-based EES devices. To develop IL based EES devices, it is imperative

to have a comprehensive understanding of the interactions and reactions at the IL–electrode interface (Fig. 1.1c). Thus, this chapter focuses on the structure of the IL–electrode interface, the interfacial electrochemical reactions, and the effects of high temperature to reveal the impact of electrode and electrolyte coupling on the performance of LIBs and SCs.

1.2 Design of Thermally Stable and Efficient ILs

The physicochemical properties of ILs are determined by the chemical structure and electrostatic interactions of the cations and anions. There are three classes of ILs according to the composition of the cation: aprotic, protic or metal-containing (Fig. 1.2a-b).[7] Aprotic and protic ILs share similar properties, but protic cations have a labile proton. The cation of a metal-containing IL is a metal-ion-containing complex,[8] such as a Li-crown ether[9] or Li–glyme.[10] For the purposes of this discussion, only aprotic and protic ILs will be addressed. To design an EES device which is safe at elevated temperatures, an IL which features high thermal stability and good ionic conductivity is required.

1.2.1 Design for High Thermal Stability

To design an IL with high thermal stability the cation of the IL must be carefully chosen as the cations of ILs generally control the thermal stability. The thermal stability of the different cation components are typically, pyrrolidinium> imidazolium> pyridinium> non-cyclic tetraalkyl ammonium cations. For example, 1-butyl-1-methyl-

pyrrolidinium bis(trifluoromethanesulfonyl)imide (PYR_{14}-TFSI), one of the most commonly used nitrogen-based IL electrolytes, is thermally stable up to 350–380 °C. Generally, pyrrolidinium ILs display a greater thermal stability than their piperidinium and morpholinium analogues.[11] Phosphonium based ILs are less studied but still demonstrate a good thermal stability, for instance trihexyl-decyl-phosphonium TFSI exhibits a decomposition temperature of 355 °C.[12] Sulfonium ILs on the other hand are less thermally stable than their corresponding nitrogen-based ILs. Moreover, the types of substituents on the heteroatom, the chain length of substituents and the hydrophobicity of the anion all influence the thermal stability of ILs.

While the decomposition temperature of the IL is determined by the cation, the decomposition temperature of the lithium salt, which provides the Li ions in the electrolyte, is influenced by the anions. Commercial devices primarily use $LiPF_6$ because of its high solubility in organic solvents and ionic conductivity. However, at temperatures above 55 °C PF_6^- degrades. Other lithium salts display a higher thermal decomposition temperature, such as lithium bis(trifluoromethanesulfonyl)imide (LiTFSI, 384 °C), lithium bisoxalatoborate (LiBOB, ~300 °C), lithium (fluorosulfonyl)-(trifluoromethanesulfonyl)imide (LiFTI, ~300 °C) and lithium bis(fluorosulfonyl)imide (LiFSI, 70 °C), but these salts do not as well as $LiPF_6$ in LIBs or SCs.[13] To replace the thermally unstable $LiPF_6$, new salts must outperform $LiPF_6$, and have the following capabilities: form a stable SEI, have a high lithium transport and solubility in ILs and nonaqueous solvents, as well as be chemically, thermally and electrochemically stable.

1.2.2 Design for High Ionic Conductivity

ILs typically display a high viscosity and low conductivity compared to organic solvent electrolytes, particularly at ambient temperatures. The high viscosity is due to the strong electrostatic interactions present between the cations and anions. Both the viscosity and conductivity of the ILs are strongly affected by the temperature, as the temperature increases the viscosity and conductivity increase and decrease, respectively, following the Arrhenius equation.[14-15] Moreover, increasing the length of the alkyl chains or decreasing the charge on the ions decreases the viscosity of ILs, by reducing activation energy necessary for the ions to flow past one another.[16]

A common method to decrease the viscosity at ambient temperatures is to reduce the strength of the ionic interaction between the cation and anion and increase the mobility of the ions and impart fluidity by mixing an IL with an organic solvent, such as EC or ACN.[17] Among these solvents, IL mixtures with ACN achieve the most efficient ion transport and highest conductivities (tens of $mS\,cm^{-1}$). However, the high volatility, flammability and toxicity due to the low flash point of ACN (~5 °C) raises health and environmental concerns and renders ACN impractical for high-temperature applications.[18] Another limitation to the solvent-IL mixtures is the decreasing electrochemical stability and thermal stability that arises from the solvation of the charged species.[19]

A promising alternative approach to reduce the viscosity and melting temperature of an IL is to mix two ILs with different cations together. It is established that the cations have a large role in prevent anion ordering.[20-22] For example, addition of 10 mol%

BenzMIM-TFSI to EMIM-TFSI (where $BenzMIM^+$ is 1-benzyl-3-methylimidazolium and $EMIM^+$ is 1-ethyl-3-methylimidazolium) leads to a lower viscosity and an ionic conductivity that is ~22% higher than neat EMIM-TFSI at 50 °C.[23] Binary mixtures of ILs have also been investigated in order to shift the crystallization to lower temperatures,[24-25] for example, a eutectic mixture forms when 1-butyl-4-methylpyridinium tetrafluoroborate ($BMP\text{-}BF_4$) and 1-butyl-3-methylimidazolium tetrafluoroborate ($BMIM\text{-}BF_4$) are mixed.[26] The dimensional mismatch between the cations inhibits the anion arrangement and, thus, lowers the melting temperature of the eutectic mixture.

1.3 Interfacial Ion Arrangement

To develop an electrolyte, an understanding of the electrolyte properties alone is not enough; when the IL electrolyte is in an EES device, it interacts with the electrodes creating interfacial effects due to the steric constraints on the electrode surface, and chemical, electrochemical and electrical field interactions. The molecular level structure of the electrode-IL interface and the impacts of the interfacial effects are described.

1.3.1 Theoretical Understanding of the EDL

Helmholtz in the nineteenth century described the electric double layer (EDL) as the formation of two layers of opposite charge that accumulate at the electrode-electrolyte interface when a potential is applied across the electrodes. The structure of the EDL varies as it extends away from the electrodes surface and the structure of an EDL

determines the energy that is stored in an EDL capacitor (also known as a non-faradaic supercapacitor). For a redox process, the driving forces are the voltage difference between the electrodes and the positions where the electrochemical reactions occur. The potential distribution in the EDL determines the electrochemical kinetics of a battery and as the applied potential is varied the ion arrangement at the electrode-IL interface changes (Fig. 1.3).

There are many models of the EDL which build from Helmholtz's description. For example, the Stern-modified Gouy–Chapman model describes a general EDL of a salt in solvent electrolyte on a charged surface; this EDL consists of two layers, a Stern layer with compact adsorbed ions and a diffuse layer with a continuous distribution of the electrolyte's cations and anions (Fig. 1.3a). Due to the strong ionic interactions present in an IL, the structure of the EDL is different than an organic solvent electrolyte. Due to these strong interactions the Stern–Gouy–Chapman model is limited, as such in 2007, Kornyshev proposed a model to describe the interfacial capacitance of a metal–IL system by solving the Poisson–Fermi equation. The Poisson–Fermi equation treats the electrolyte using a mean-field lattice-gas model, and derived an analytical expression for the differential capacitances of local concentrations of different ions.[27] The model predicted that when the ionic concentration changes from low to high a crowding effect arises at the electrodes surface; as there is no space left to pack more counterions on the surface of the electrode, the thickness of the double layer increases with increasing voltage. Independently, Bazant and colleagues derived the same analytical solution utilizing a different mathematical approach.[28] Classical density functional theory (DFT) is able to

identify the same effect as the ionic concentration is increased using a coarse-grained molecular model of ILs.[29] Classical DFT also predicted alternating cation–anion layered structures of up to 10 layers on a strongly charged surface.[30] To further explain the changing EDL in high ionic concentration mediums, Bazant, Storey and Kornyshev developed a simple Landau–Ginzburg-type continuum theory of the EDL for an electrode–IL system.[31] The model predicts that at small electrode polarization, a charged surface will be over-screened by a monolayer of counterions (Fig. 1.3b), and the excess charge will be neutralized by abundant co-ions in the second layer.

1.3.2 Experimental Observation of the EDL

Mezger et al, using a sapphire (0001) were able to experimentally observe the over-screening of ILs. The over-screening of ILs manifests as oscillating layers of ions normal to a charged interface.[32] And with integrated X-ray reflectivity and classical MD simulations on BMIM-TFSI near charged and uncharged graphene surfaces, Fenter and co-workers observed alternating cation-rich and anion-rich layers extending several layers out from the graphene surface, consistent with earlier work.[33] Another method to detect the ion arraignment on the surface and garner understanding of the layered structure of the EDL is Atomic Force Microscopy (AFM). For instance, with amplitude-modulated AFM the ordered lateral packing behavior of EMIM-TFSI on a highly ordered pyrolytic graphite electrode was observed (Fig. 1.3c).[34] The structure of ion layers beyond the first layer can also be probed by AFM.[35] It was found that a layered structure of ions extends for around four to seven layers, with a more stable layered structure under

negative polarization (cations adsorbed at the interface) compared with positive polarization (anions adsorbed at the interface). The structure changes slightly depending on the exact compositions of the IL.

The molecular-level arrangement of ILs at a surface under an applied potential can be changed by varying the composition of the ions and the alkyl chain lengths. For example, $EMIM^+$ with a short tail (ethyl group) forms a stronger interfacial structure than $BMIM^+$ (butyl group) as the imidazolium ring of $EMIM^+$ is oriented more parallel to the Au(111) surface. By contrast, the packing of $HMIM^+$ (1-hexyl-3-methylimidazolium) is more orderly than that of $BMIM^+$, as its longer tail increases solvophobic interactions.[36] In addition, the alternating cation-rich and anion-rich layers formed with pyrrolidinium-based ILs transform into a cationic bilayer structure with interdigitated alkyl chains once the length of the alkyl chain on the cation increases from C_8 to C_{10}.[37] Notably, the neutral alkyl chains on the cations can increase the capacitance at small and intermediate voltages, because they function as latent voids that can be replaced by charged groups to increase the local concentration of charges.[38]

The order packing structure of the EDL on the electrode surface does not extend throughout the entire surface, instead there are domains of ordered IL structure. For example, PYR_{14}-TFSI forms an ordered lateral structure with stripe-shaped domains of a few hundreds of nanometers in length on uncharged highly ordered pyrolytic graphite.[39] The orientation of the stripes is induced by the hexagonal graphite substrates, as indicated by the 120° angle between domains of different orientation. Although the ions adsorbed outside of the domains do not form an ordered lateral structure, the layered structure of

the IL normal to the surface is almost the same as that in the domains. The ordered lateral structure in the domains disappears when a large potential is applied ($V < -0.6$ V or $V > 0.4$ V vs open circuit potential (OCP)).

1.3.3 Effects of Changing Potential

The structure of an EDL in an IL changes with the applied potential (Fig. 1.3). A neutral state represents the state at which there is no specific adsorption of cations or anions on the electrode surface, and the potential of this state might not be zero. For example, an Au(100) surface in BMIM-BF_4 has a potential of approximately –0.65 V (vs Pt) in its neutral state.[40]

X-ray reflectivity was used to investigate the dynamic response of the layered structure of MNIM-TFSI (where $MNIM^+$ is 1-methyl-3-nonylimidazolium) on pristine epitaxial graphene surfaces during potential cycling as a function of temperature.[41] The IL exhibits different well-defined alternating cation–anion layered structures at positive and negative surface potentials (vs OCP). Both structures are present during cycling through the OCP, forming a hysteretic intermediate mixture with a characteristic lifetime on the order of seconds. The temperature dependence of the restructuring (25–60 °C) indicates an energy barrier of ~0.15 eV between the distinct cation-adsorbed (at the negatively charged surface) and anion-adsorbed (at the positively charged surface) structures. This finding is consistent with AFM observations, which indicate that even at OCP, the interfacial IL is organized into alternating cation-rich and anion-rich layers at a local level near the electrode surface.[42] Results from a neutron reflectometry study of

PYR_{14}-TFSI on a gold electrode support this observation, revealing an excess of cations at the interface in the uncharged state.[43] Increasing the positive charge of the electrode decreases the concentration of the cations at the interface. By contrast, a slight increase in the negative polarization increases the cation excess, with the cations forming a loosely adsorbed layer, which is the initial stage in the formation of the over-screening structure.

The loosely adsorbed layer formed during the initial stage of cation adsorption transforms into an ordered structure with increasing negative polarization and, thus, an increasing population of cations. This behavior was observed using amplitude-modified AFM for EMIM-TFSI on a highly ordered pyrolytic graphite surface as the potential was changed from –0.1 V to –0.3 V (versus the uncharged state) (Fig. 1.3c).[34] Upon further increasing the negative polarization, cations reorient from close-to-parallel to vertically aligned with a slight incline to the electrode surface (Fig. 1.3d).[44]

As the potential is further increased, the over-screening structure transitions into a 'crowding' structure, in which counterion adsorption dominates the first two monolayers from the electrode surface, while the co-ions move to the third layer to balance the excess charge (Fig. 1.3e).[31] The crowding structure was observed by operando X-ray scattering on a silicon electrode with THTDP-TFSI (where $THTDP^+$ is trihexyl-tetradecylphosphonium) as the electrolyte[45] and by neutron reflectometry on a niobium electrode with THTDP-PFPB (where $PFPB^-$ is tetrakis(pentafluorophenyl)borate).[46]

1.4 EDL with Porous Carbon Electrodes

In the EDLs observed above, ideal flat and metallic surfaces were utilized, however,

the most common electrode in supercapacitors is composed of porous carbon. Porous carbon is neither flat nor metallic, and it is heterogeneous with reactive edge sites,[47] defects[42] and surface functional groups[48-49]. Due to the presence of pores in a carbon electrode, there is a weakening of the screening from the ionic interactions between the ions and the wall as the electric fields of the ions absorbed on the walls penetrates to the pores, this weakened electrostatic interactions increases the distance between the adsorbed ions and the carbon electrode. Plus, as the porous carbon electrode is heterogenous, there is added complexity to the structure of the electrodes and steric limitations due to the variability in pore size which breaks the structure of the EDL.

Moreover, carbon electrodes interact with the ions of the IL whereas the metallic surfaces could not. For instance, in a carbon electrode the graphenic components of the material display π–π interactions with imidazolium rings. The ion arrangement and capacitance are also changed due to confinement present in the pores of the electrode. For example, surface hydroxyl groups attract anions closer to the pore walls, even at a negatively charged surface (with a surface charge density of –4.0 $\mu C\ cm^{-2}$)[48] and restrain the anion orientation and mobility.[50-51]

Increasing the surface area of the electrode through the formation of nanopores can increase the capacitance of the EES device. It was found that with pores smaller than 1 nm, the normalized capacitance (capacitance per surface area) is enhanced.[52-53] For a neat IL, the dramatic increase in the normalized capacitance is explained by a mathematical model that assumes close packing of the ions in pores.[54] Pore volume directly correlates to the normalized capacitance, and pore volume utilization is maximized when the pore

size matches the ion size. To design a realistic supercapacitor electrode material to approach the theoretical capacitance limit in a specific IL, the pore size distribution should be narrow, ideally monodispersed, with an average size selected carefully based on the ion size and operating voltage.[55]

The effect of temperature on the EDL also influences the charge-storage capability of IL-based EES devices. Disruption of the interfacial EDL structure at higher temperatures, as observed by in situ scanning tunneling microscopy and in situ AFM, lowers the capacitance.[56] Moreover, as elevated temperature weakens the ion–electrode interactions, the distance between the electrode surface and the adsorbed ions increases, which may decrease the capacitance.[32] The Debye length, a characteristic length that describes how the surface charge is screened by the electrolyte, is also temperature dependent and influences the EDL.[31]

1.5 Effect of Interfacial Reactions on ESW

An IL-based supercapacitor stores charge through counterion adsorption on the charged electrode and the formation of an EDL (Fig. 1.1c, left). For a conventional IL-based LIB, the IL functions as a ‘solvent’ to dissolve the Li salt, and only Li ions intercalate and de-intercalate at the cathode and anode and contribute to the capacity (Fig. 1.1c, right). Although ILs have good electrochemical stability compared with other electrolytes, IL-based EES devices still have a limited ESW owing to undesired electrochemical reactions at the electrode (Fig. 1.4a). Compared with a supercapacitor (in which the ESW is mainly limited by interfacial electrolyte decomposition), more diverse

and complex irreversible interfacial reactions occur in a LIB, including the co-intercalation of organic ions, electrolyte decomposition, SEI formation and the formation of 'dead' Li. Undesired electrochemical reactions at the interface can also trigger self-discharge mechanisms, shorten the cycling life and raise safety concerns due to the loss of active electrode materials, structural damage, gas release and electrolyte consumption. To increase the energy density of IL-based EES devices and ensure their safe operation, it is crucial to understand the possible interfacial reactions and the effect of temperature on these reactions.

1.5.1 Irreversible Intercalation of Organic Cations

To simplify the electrolyte in an IL-based LIB, a Li salt with the same anion as the IL can be used. The Li ions in the electrolyte are likely solvated by anions and form $[Li(anion)_x]^{(x-1)-}$ complexes (such as $[Li(TFSI)_2]^-$ in the case of a binary mixture containing LiTFSI).[57] Complexation increases the hydrodynamic radius of Li^+, and the electrolyte viscosity increases with an increase in Li salt concentration, resulting in decreased electrolyte ionic conductivity. Before Li^+ intercalation in an IL-based LIB, decomplexation (or desolvation) of the $[Li(anion)_x]^{(x-1)-}$ complex occurs at the electrode–electrolyte interface and liberates the anions. The interaction between Li^+ and the anions substantially affects the interfacial charge-transfer process during ion intercalation.[58] For example, the charge-transfer resistance at the electrode–electrolyte interface in a LIB comprising a Li metal anode and $LiCoO_2$ cathode with various Li salts dissolved in an *N*,*N*-diethyl-*N*-methyl-*N*-(2-methoxyethyl) ammonium-based IL, strongly depends on the

anion; among various anions, the system with the FSI^- anion exhibits the lowest charge-transfer resistance (Fig. 1.4b).[59]

The presence of organic cations causes competitive intercalation with Li^+. For instance, in an electrolyte comprising LiTFSI and EMIM-TFSI, $EMIM^+$ inserts into a layered graphite electrode at a potential of ~1 V (vs Li/Li^+) during an initial cathodic scan.[60] The intercalation of the organic cations is usually irreversible and destroys the layered structure of the anode, compromising performance. To prevent the intercalation of organic cations, the intrinsic intercalation properties of the electrode materials and the electrolytes should be considered. For example, combining $EMIM^+$ with the FSI^- anion, suppresses the intercalation of the organic cations, allowing reversible Li^+ intercalation at 0–0.2 V (vs Li/Li^+) on graphite.[60] One possible explanation for this behavior is that the decomposition of FSI^- during the initial charging cycle leads to the formation of a passivating SEI that prohibits the intercalation of $EMIM^+$.[61] Moreover, intercalation of organic cations is hindered if the electrode material allows Li^+ to intercalate at a relatively positive potential compared with the decomposition potential of $EMIM^+$. For example, a titanium oxide bronze (TiO_2-B) electrode operates stably in a voltage window of 1.2–2.5 V with a LiTFSI–EMIM-TFSI electrolyte, because the lithiation–delithiation potential (~1.5 V vs Li/Li^+) lies within the ESW of EMIM-TFSI.[62] Similarly, lithiated titanium oxide, with a redox potential of 1.5 V (vs Li/Li^+), is a suitable anode for a full-cell device with an IL-based electrolyte in combination with a high-potential cathodic material, such as $LiCoO_2$.[63]

1.6 Effects of High Temperature

Increasing the temperature not only accelerates the kinetics of reactions that occur at room temperature, but also initiates chemical or electrochemical side reactions. Cyclic voltammetry was used to investigate the room-temperature and high-temperature electrochemical stability of different ILs (including EMIM-TFSI and PIP-TFSI (where PIP^+ is 1-methyl-1-propylpiperidinium)) and a carbonate-based electrolyte with LiTFSI on a TiO_2-B electrode (Fig. 1.4c,d).[62] Comparing the cyclic voltammograms obtained at 25 °C and 120 °C, the lithiation process evolves into three separate pairs of redox reactions, indicating that the rates of deintercalation and intercalation are increased at higher temperatures. The onset reduction potential of $EMIM^+$ is 0.6 and 1 V (vs Li/Li^+) at 25 °C and 120 °C, respectively, suggesting that reduction is promoted at higher temperatures. Although anodic decomposition is suppressed when pyrrolidinium-based and piperidinium-based ILs are used, the decomposition-free voltage still shifts from 0.5 to 1.0 V at the elevated temperature, indicating shrinkage of the ESW. The compatibility of the IL with different electrode surfaces is crucial to the electrochemical stability at elevated temperature. Some cation and anion combinations have lower onset temperatures for thermal runaway than that of conventional EC:DEC electrolytes on specific charged electrode surfaces; for example, the runaway temperatures for EMIM-FSI and EC are 70 °C and 140 °C, respectively, on $Li_7Ti_5O_{12}$, and 225 °C and 325 °C, respectively, on $Li_{0.45}CoO_2$.[64]

Due to the decreased ESW at elevated temperatures, operating a device within the same voltage window as at room temperature lowers the Coulombic efficiency of Li^+

intercalation and deintercalation because of the formation of a thick SEI film that blocks Li^+ intercalation and increases the impedance.[62, 65] For example, for a graphite electrode in an organic solvent, the thickness of the SEI increases with ascending temperature, resulting in a 50% increase in cell impedance at 70 °C.[65] A thin SEI layer formed on a Si anode at 60 °C when using an IL electrolyte free of organic solvent (0.5 M LiFSI in PYR_{13}-FSI, where PYR_{13}^+ is 1-methyl-1-propyl-pyrrolidinium). Compared with the thick film formed in a carbonate-based electrolyte (1.0 M $LiPF_6$ in fluoroethylene carbonate: DMC), the IL-derived thin film enables longer, more stable device operation at 60 °C.[66] In another example, PIP-TFSI–LiTFSI affords a SEI layer on a Si anode that is thicker than that of an organic electrolyte (1.0 M $LiPF_6$ in EC:DEC).[67] Adding PC into the PIP-TFSI–LiTFSI mixture increases the contribution of the $TFSI^-$ decomposition product to the composition of the SEI and decreases the thickness of the SEI layer. The SEI layers formed by the reduction of the IL-based electrolytes (with or without PC) are stable up to 100 °C, and the LIB operates at 100 °C with the same cycling stability as at room temperature. Moreover, IL-derived films formed on a graphite electrode at 90 °C, using LiTFSI in PYR_{13}-TFSI, PIP-TFSI or BMIM-TFSI, are thicker and more thermally resilient than the corresponding films formed at 25 °C.[68] Although the thicker films show increased charge-transfer resistance, the capacity of the electrodes covered by the thicker films, surprisingly, increases at a low rate (<0.1 C), likely due to improved wetting of the electrode by the electrolyte and higher Li^+ transference numbers in the films. Additionally, increasing the concentration of a Li salt (LiFSI) in trimethylisobutylphosphonium bis(fluorosulfonyl)imide enhanced the mechanical

stability of the resultant SEI, which remained intact on the Si electrode after 60 cycles at 80 °C.[69]

Thermal breakdown of the SEI layer, which leads to the build-up of internal resistance and continuous consumption of electrolyte and electrode materials, also limits electrochemical stability at elevated temperatures. For electrodes, such as Si, that undergo large volume expansion and/or shrinkage during the charge and discharge processes, decomposition of the SEI is more profound at elevated temperatures when the rate of Li^+ intercalation and deintercalation is faster.[70] To construct a SEI that is thermally stable at high temperature, the electrolyte, Li salt and electrode must be considered. Ongoing research should focus on understanding the mechanism of SEI formation and its dependence on anode–electrolyte–cathode combinations to develop a strategy to design SEI layers with improved thermal stability and cycling performance.

1.7 Summary

The inherent conductivity, thermal and electrochemical stability of IL electrolytes significantly improve the safety and operational temperatures of EES devices. However, the full capabilities of ILs cannot be accessed until the ESW, interfacial interactions, and rate capabilities are maximized to improve IL-based EES device performance. The charging mechanisms for each unique IL formulation in conjunction with the electrode materials and applied potential must be analyzed and defined as units. As the electrodes surface chemistry and pore structure effect the structure of the EDL and the compositions of the IL's cations and anions further alter the EDL structure, to develop an optimized

EES devices requires research efforts to combine molecular modeling, materials science, and chemistry together. In summary, understanding the chemical reactions and interfacial interactions that govern device performance will be the key to future success.

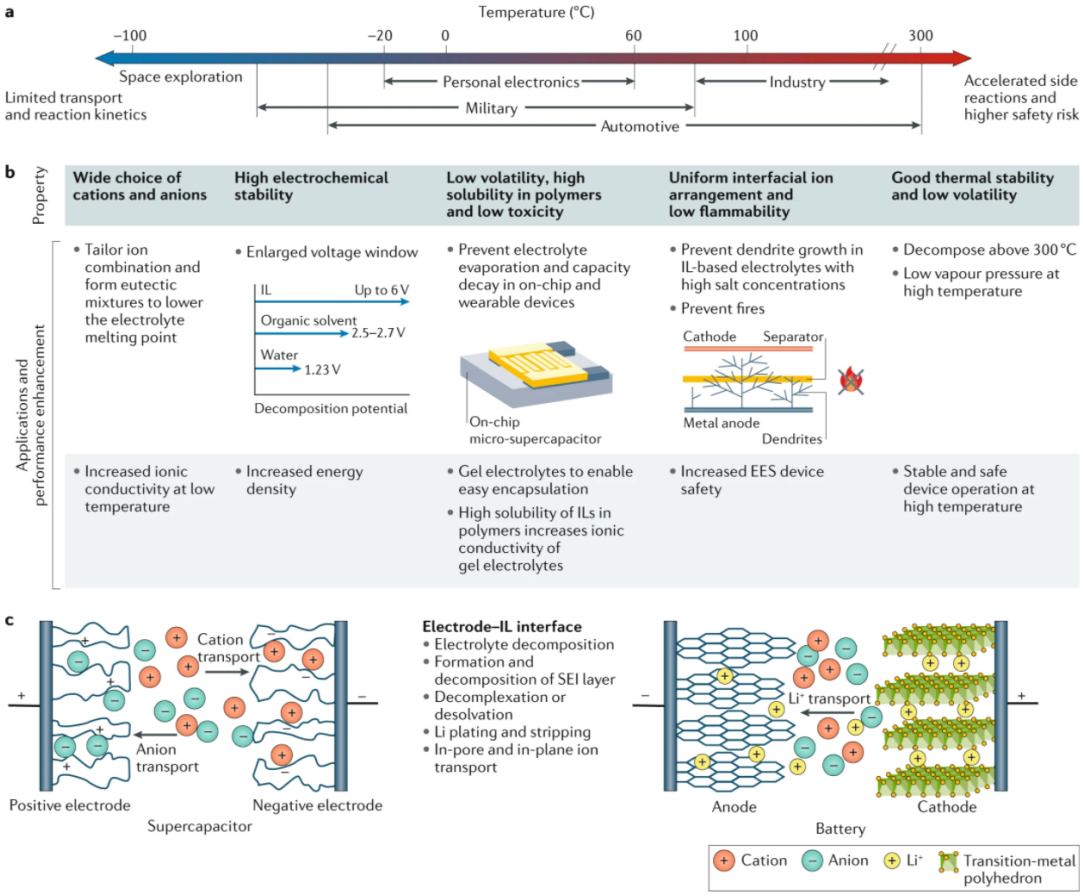

Fig. 1.1 **IL electrolytes for EES devices.** **a** Temperature windows for various applications of EES devices. **b** Advantages of using ILs as electrolytes in EES devices. Examples of devices that could benefit from IL electrolytes include on-chip and wearable devices (such as the knitted supercapacitor shown in the photograph) and LIBs. **c** Schematics showing the electrochemical processes that occur at the electrode–IL electrolyte interfaces within a supercapacitor and Li-ion battery. SEI, solid electrolyte interphase. Panel **b** (knitted supercapacitor) adapted from ref.[71].

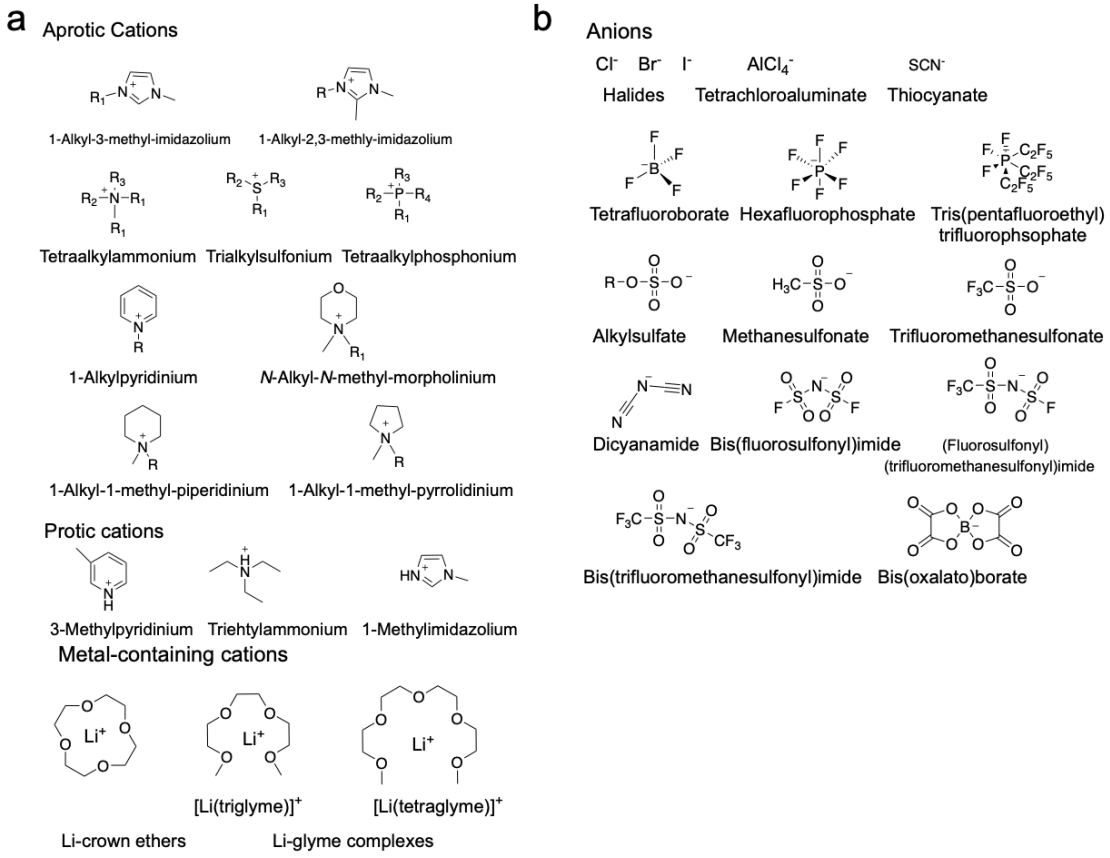

Fig. 1.2 **IL ions and properties of IL mixtures. a,b** Cations and anions commonly used for the formulation of ionic liquid (IL) electrolytes for energy-storage devices.

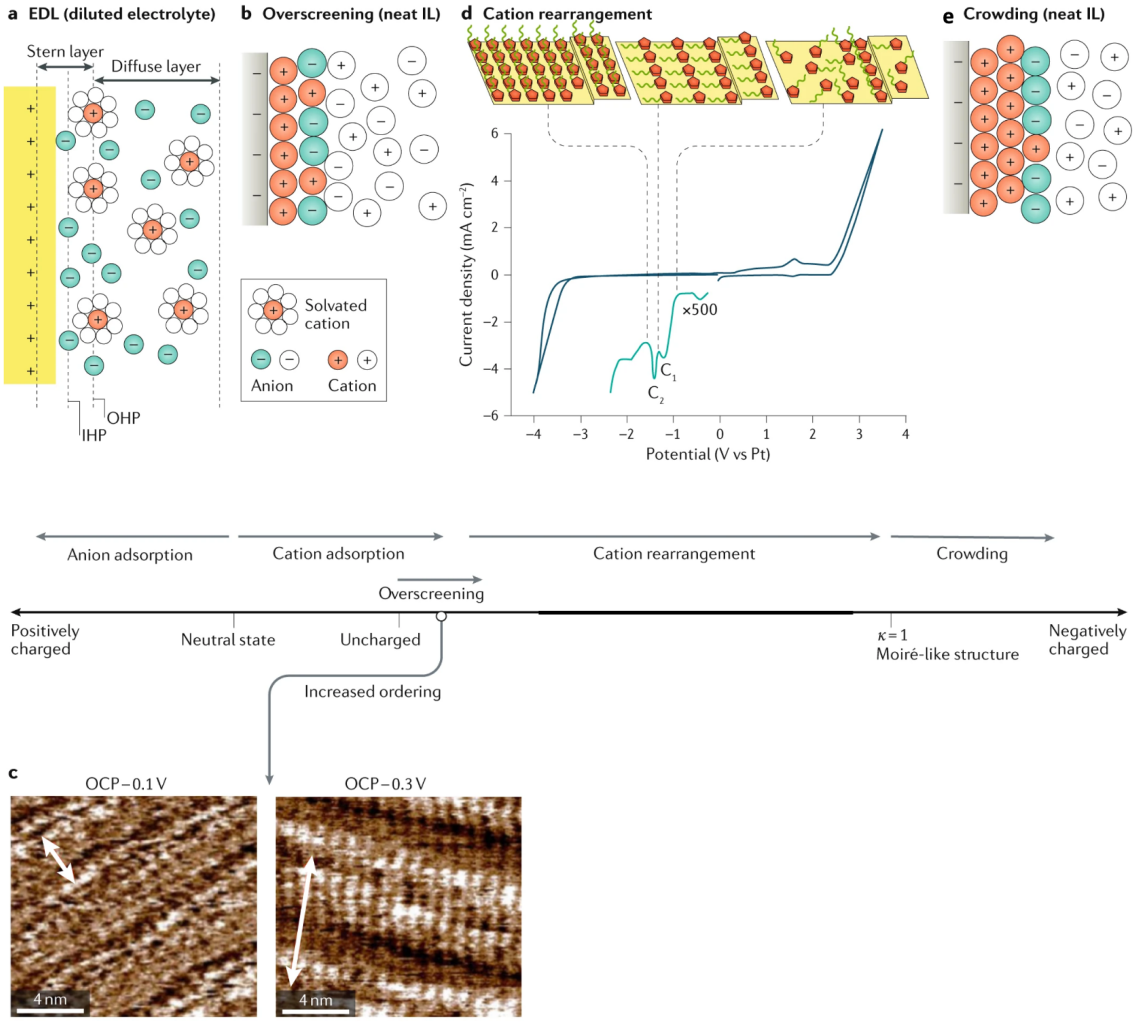

Fig. 1.3 **Structure of the IL–electrode interface.** An EDL forms at an electrode–electrolyte interface. For neat ILs, the structuring of ions at the interface is dependent on the applied potential and changes with increasing negative polarization **a** For an electrode surface in a diluted electrolyte, the EDL comprises a Stern layer and a diffuse layer (where IHP and OHP are the inner and outer Helmholtz planes, respectively). **b** For a neat IL, the surface charge is overscreened by a monolayer of counterions, and the co-ions in the second monolayer balance the excess charge. **c** Amplitude-modulated atomic

force microscopy images of 1-ethyl-3-methylimidazolium TFSI adsorbed on a highly oriented pyrolytic graphite substrate at –0.1 V and –0.3 V versus the OCP.[34] The red arrows indicate the repeat spacing in the image; as the potential decreases, the adsorbed layer becomes more ordered. **d** Cyclic voltammogram of an Au(111) electrode in 1-butyl-1-methylpyrrolidinium TFSI.[44] Starting from the OCP, two cathodic peaks (C_1 and C_2) are observed in the negative direction and correspond to rearrangement of the cations (as shown in the insets). **d** was observed in high-resolution scanning tunneling microscopy images of the PYR_{14}^+ adlayer on Au(111) at −1.4 V (5.4 nm × 7.5 nm) and −1.6 V (4 nm × 414nm).[44] Here, $a_2 = 0.51 \pm 0.05$ nm, $b_2 = 1.01 \pm 0.05$ nm, $a_3 = 0.50 \pm 0.05$ nm and $b_3 = 0.55 \pm 0.05$ nm. **e** Crowding structure for a neat IL. Counterion adsorption dominates the first two monolayers from the electrode surface, and the co-ions move to the third layer to balance the excess charge. κ, dimensionless surface charge compensation parameter. Panels **b** and **e** adapted from ref.[31], APS. Panel **c** adapted from ref.[34]. Panel **d** adapted from ref.[44].

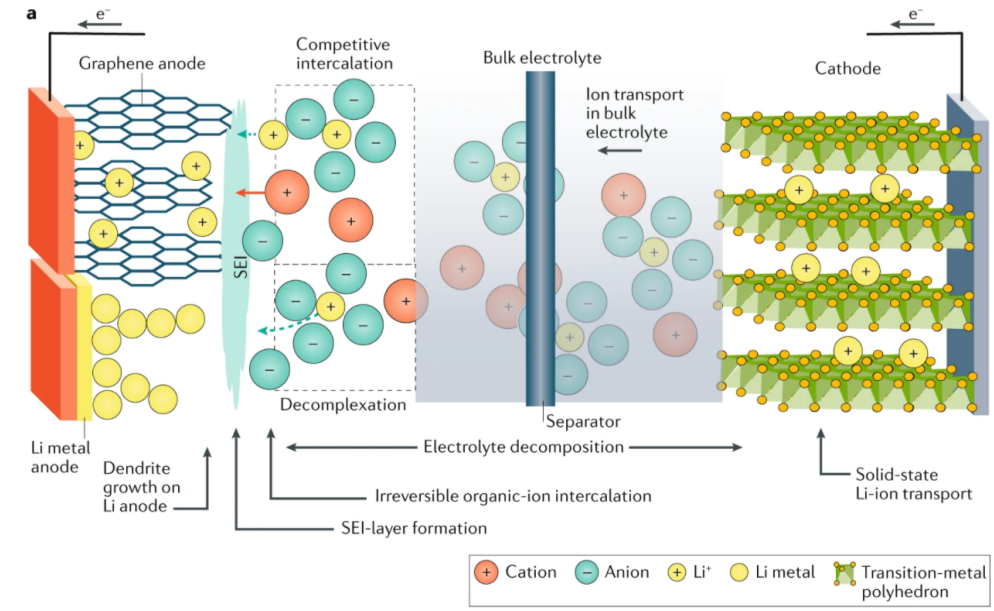
a
e⁻
Graphene anode
Competitive intercalation
Bulk electrolyte
Ion transport in bulk electrolyte
Cathode
SEI
Decomplexation
Separator
Li metal anode
Dendrite growth on Li anode
Electrolyte decomposition
Irreversible organic-ion intercalation
SEI-layer formation
Solid-state Li-ion transport
Cation
Anion
Li⁺
Li metal
Transition-metal polyhedron

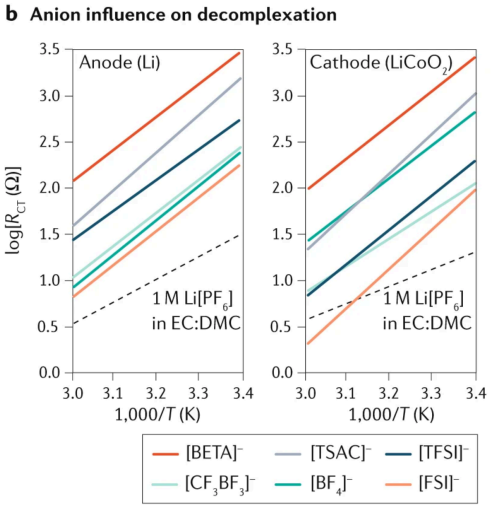
b Anion influence on decomplexation
Anode (Li)
Cathode (LiCoO2)
log[RCT (Ω)]
1,000/T (K)
1 M Li[PF6] in EC:DMC
[BETA]⁻
[TSAC]⁻
[TFSI]⁻
[CF3BF3]⁻
[BF4]⁻
[FSI]⁻

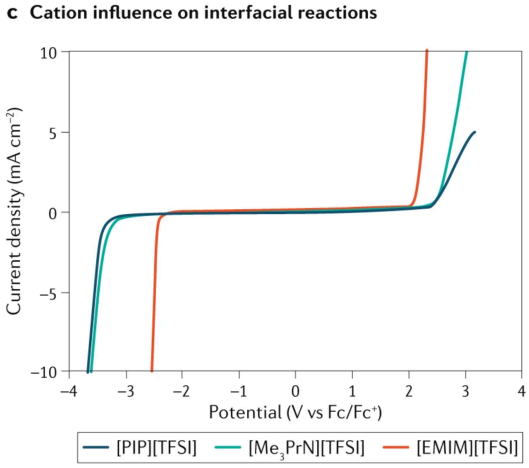
c Cation influence on interfacial reactions
Current density (mA cm⁻²)
Potential (V vs Fc/Fc⁺)
[PIP][TFSI]
[Me3PrN][TFSI]
[EMIM][TFSI]

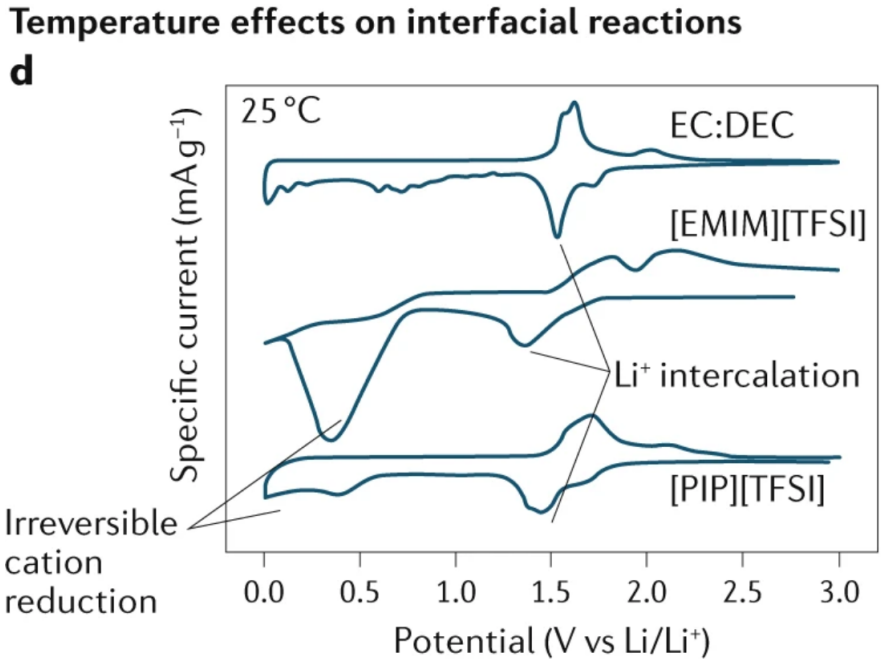

Fig. 1.4 **Interfacial reactions.** **a** Schematic showing the possible undesirable electrochemical reactions that occur at electrode–ionic liquid (IL) interfaces. **b** Arrhenius plot of the apparent charge-transfer resistance (R_{CT}) of a $LiCoO_2$ cathode and Li anode in ILs with the *N*,*N*-diethyl-*N*-methyl-*N*-(2-methoxyethyl)ammonium cation and various anions (where $BETA^-$ is bis(perfluoroethylsulfonyl)amide, $TSAC^-$ is 2,2,2-trifluoro-*N*-(trifluoromethylsulfonyl)acetamide). For comparison, the R_{CT} of 1 M $LiPF_6$ in EC:DMC is also shown. The cell voltage is kept at 4.2 V (ref.[59]). **c** Linear sweep voltammograms of $TFSI^-$-based ILs with different cations ($EMIM^+$ is 1-ethyl-3-methylimidazolium, Me_3PrN^+ is trimethylpropylammonium) measured at a scan rate of 50 mV s^{-1} at 25 °C. The working and counter electrodes are glassy carbon and Pt, respectively[71]. **d** Cyclic voltammogram for a titanium oxide bronze electrode in three different electrolytes

(where DEC is diethylcarbonate) with a scan rate of 0.1 mV s^{-1} at 25 °C (ref.[62]). Panel **b** adapted from ref.[59]. Panel **c** adapted from ref.[72]. Panels **d** adapted from ref.[62].

Chapter 2: Piperidinium Ionic Liquids as Electrolyte Solvents for Sustained High Temperature Supercapacitor Operation

Adapted from: Piperidinium ionic liquids as electrolyte solvents for sustained high temperature supercapacitor operation. *Chemical Communications*, 2018, 54, 5590-5593.

2.1 Introduction to Supercapacitors

Electrical energy storage (EES) devices, operating at elevated temperatures from 25 to 100 °C, are in increasing demand as applications in consumer goods, oil and mining, and automotive industries expand to meet new market opportunities.[3, 73-78] Currently, the number and variety of such commercially available EES devices are limited. For example, the lithium-thionyl chloride ($LiSOCl_2$) battery is one of the most robust systems available, but $LiSOCl_2$ batteries exhibit high internal resistance and $SOCl_2$ is toxic, corrosive, and hazardous. There has been more success with supercapacitors (e.g., Evans and FastCap), albeit these devices exhibit reduced cyclability at elevated temperatures.[79-80] This is a materials-centric and multifaceted problem with significant research efforts directed at synthesizing new electrode, electrolyte, and spacer materials. This challenge is compounded by the desire to have both small portable devices as well as devices that provide high capacity and/or rapid power response. While a number of breakthroughs are reported describing new high energy/power density electrode materials,[75, 77, 81-85] thermally stable separators,[86,87] and electrolytes,[88-91] electrolytes remain a limiting factor precluding wide-spread practical use in the above-mentioned applications and represent an opportunity for research. Our interest is in thermally stable, non-flammable, non-

volatile electrolytes for use in EES devices at elevated operating temperatures. Specifically, we report the: 1) synthesis of a series of non-flammable, thermally stable alkyl ether containing piperidinium ionic liquid electrolytes with lithium bis(trifluoromethanesulfonyl)imide (LiTFSI); 2) density functional theory calculations of the cation-anion binding energies completed by our collaborators Alexander Hino and Prof David Coker; 3) temperature and LiTFSI concentration dependence on ion conductivity and viscosity; and, 4) sustained performance of a lithium ion supercapacitor (LIC) at 100 ^{o}C.

2.2 Physiochemical Properties of Piperidinium Ionic Liquid Electrolytes

2.2.1 Rationale for Ionic Liquid Selection

Our selection of ionic liquids (ILs) to address this recognized problem in electrolyte deficiencies is supported by a number of reports describing imidazolium and phosphonium based ionic liquids and their corresponding low vapor pressure and non-flammability.[92,93] Significant research efforts are also underway to identify alternative thermally stable electrolytes, such as ionic liquid-carbonate-based solvent electrolyte mixtures,[67] ethoxy propylene carbonate electrolytes,[94] and solid polymer electrolytes (SPEs),[95] including degradable and environmentally friendly systems.[96] The key attributes responsible for SPE performance are compositions containing a large fraction of oxygen atoms to promote lithium salt dissociation (e.g., poly(ethylene oxide)), possessing low glass transition temperatures to increase segment mobility and ion transport, and exhibiting high thermal decomposition temperatures to ensure non-

flammability (≥150 ºC).

Piperidinium ionic liquids possess a number of favorable properties including non-flammability, a large electrochemical stability window (-3.8 to 2.5 V vs Pt), and inherent conductivity for use as an electrolyte solvent in electrical energy storage devices.[97-98] The archetypical piperidinium IL is N-methyl-N-propyl-piperidinium, **1**, and **1** has been extensively investigated by several laboratories since its first synthesis.[72, 99-100] Inspired by the performance of SPEs, we introduced an alkyl ether chain into the structure of **1** and synthesized similar analogues containing one, **2**, or two ether atoms, **3** (Fig. 2.1). With this structural change, we hypothesize that the benefits associated with SPEs will also be seen in these ILs, with a concurrent reduction in viscosity and increase in conductivity compared to **1**.[101-102]

2.2.2 Conductivity and Viscosity of Ionic Liquid Electrolyte

Prior to performing the supercapacitor experiments, the thermal stability, viscosity, and conductivity of **1**, **2**, and **3** were measured. Before each test, the samples were dried at 80 ºC while under vacuum for at least 6 hours. Thermal Gravimetric Analysis (TGA) on samples heated from 20 to 500 ºC at a rate of 10 ºC min^{-1} revealed decomposition temperatures of 386, 288, and 356 ºC for **1**, **2**, and **3**, respectively. The substitution of an oxygen atom for a methylene in the composition reduces the decomposition temperature, as such, compounds **2** and **3** are less stable than **1**, with **2** being the least stable. Though all are stable at 100 ºC, differential scanning calorimetry (DSC) analysis shows no T_m or T_c for **2** or **3**, indicating the compositions are a liquid over a wide temperature range, this

is unlike **1** which has a T_m and T_c at 19 and -23 ºC, respectively.

Next, the viscosity and conductivity of the neat ILs, **1**, **2**, and **3** as well as electrolyte compositions of **1**, **2**, and **3** with 0.5 and 1.0 M LiTFSI were measured as a function of temperature from ≈ 25 to 100 ºC. The conductivity is directly correlated to the temperature but inversely correlated to the added LiTFSI concentration; the opposite trend is observed for viscosity (Fig. 2.2). As the temperature increased the viscosity values for **1**, **2**, and **3**, and the electrolyte mixtures decrease. The ILs containing ether groups within the alkyl chain display a greater decrease in viscosity compared to **1**. For instance, at 25 ºC **1**, **2**, and **3** with 1.0 M LiTFSI salt possess viscosities of 0.42, 0.22, and 0.39 Pa.s, respectively. At lower temperatures IL electrolyte **2** exhibits the lowest viscosity value. At higher temperatures, the difference between the three IL electrolytes diminishes and all three IL electrolytes display nearly the same viscosity of approximately 0.03 Pa.s. The conductivity of ILs **1**, **2**, and **3** increase with increasing temperature, and it is clear that the incorporation of the ether group increases the conductivity of the ILs as both **2** and **3** possess conductivities slightly higher than **1**. At 25 ºC, ILs **1**, **2**, and **3** possess conductivities of 1.40, 2.29, and 1.99 mS/cm, respectively. Upon addition of LiTFSI to the ILs, the conductivity values of all three electrolytes decrease. IL **2** with 1.0 M LiTFSI possesses a conductivity value of 0.56 mS/cm at 25 ºC, while **1** and **3** with 1.0 M LiTFSI salt both have a value of ≈ 0.25 mS/cm. At 105 ºC, the conductivity difference between electrolytes **2** and **1** is more pronounced with the values being 9.2 and 7.5 mS/cm, respectively. The conductivity value for electrolyte **3** with 1.0 M LiTFSI is 6.2 mS/cm at 105 ºC, which is lower than **1**. For comparison, the

conductivity and viscosity values of propylene carbonate (PC) with 1.0 M LiTFSI, a conventional electrolyte, at 25 and 80 ºC are 4.8 mS/cm, 0.006 Pa.s, and 10.8 mS/cm, 0.003 Pa.s, respectively (See Fig. 2.3).[103] The conductivity values measured at elevated temperatures for these electrolytes are similar to literature values.[67, 100, 104-105]

2.3 Binding Energies of Piperidinium Ionic Liquids and Lithium Salts

Binding energy calculations were completed by and in collaboration with Alexander Hino and Prof. David Coker. Calculations using density functional theory (DFT; Gaussian 16; B3LYP-D3BJ/6-311G(d,p) using B3LYP-D3BJ/6-31G(d) optimized geometries) were next performed to gain further insight into observed viscosity and conductivity trends with the piperidinium ILs.[106] The inclusion of empirical dispersion and basis set superposition error corrections are important for calculations relevant to ILs.[107-108] The cation-anion binding energies for **1**, **2**, and **3** are similar in magnitude and approximately two times lower than that calculated for LiF (Table 2.1). The weak electrostatic interaction energies are consistent with **1**, **2**, and **3** being liquids at 25 ºC as well as the reduction in viscosity with increasing temperature; as sufficient energy is added to the system to overcome the interaction energies, the cation-anion pairs dissociate and the viscosity of the system reduces. Similarly, the conductivities of **1**, **2**, and **3** increase at elevated temperatures as the ions move more freely. However, a direct correlation between the small differences in binding energy values of **1**, **2**, and **3** and viscosity/conductivity data was not identified. This observation may be the result of the piperidinium IL's molecular weight or size being a greater contributor to the outcome

(e.g., **3** has a larger mass and viscosity compared to **2**) or a limitation of the DFT method.[109] An addition of LiTFSI to **1**, **2**, and **3** increases the viscosity values as there is more material per volume. The conductivity values also decreased with added LiTFSI in a concentration dependent manner. This result is consistent with the increased viscosity with added LiTFSI. Additionally, given that the binding energy of LiTFSI is on par with **1**, **2**, or **3**, a portion of LiTFSI and the electrolyte move as neutral pairs within the electrolyte. For comparison, the calculated binding energies are lower in a higher dielectric constant medium (e.g., PC), suggesting the ions are separated. These neutral pairs reduce the rate of ions flowing through the electrolyte, affording a decrease in conductivity as the concentration of LiTFSI is increased. Again, raising the temperature provides energy to overcome these electrostatic interactions, and the conductivity increases as more ions move as single species and not pairs. This explanation does not completely describe the conductivity-temperature dependence relationship as the conductivity values for **1**, **2**, or **3** do not converge at a single high temperature value. Additional calculations are ongoing to understand the finer details of cation-anion pairing and its dependence on specific piperidinium IL compositions in the presence of added Li salt.

2.4 Piperidinium Ionic Liquid Electrolytes Performance in a Supercapacitor

Given the thermal stability, lack of thermal transitions, lower viscosity, and higher conductivity of IL electrolyte **2** with 1.0 M TFSI compared to **1** and **3**, we selected electrolyte **2** and evaluated its performance in a supercapacitor at 25 ^{o}C and 100 ^{o}C

compared to PC with 1.0 M LiTFSI. The supercapacitors were fabricated using a method previously described.[94] The Celgard separators were soaked in 100 uL of the IL electrolyte at 60 ºC for 15 minutes to ensure that the viscous electrolyte fully penetrated the separators. The cells were assembled and the capacitance values measured using a multichannel Princeton Applied Research VersaStat MC Battery tester. The cells were equilibrated at room temperature or 100 ºC for 30 minutes, and tested within an electrochemical window of 0 to 2.5 V at current densities equal to 1, 2, 5 and 10 A/g. Charge-discharge cycling was performed to calculate the energy density, power density, and discharge capacitance to analyze the cycle life.

The first five charge-discharge cycles of the supercapacitor with electrolyte **2** and PC at 100 ºC show a similar dynamic range (Fig. 2.4– left; see Fig. 2.5 for data at 25 ºC). The Ragone plot for the PC and electrolyte **2** at 25 ºC and 100 ºC (Fig. 2.4-right) reveals that the supercapacitor containing electrolyte **2** exhibits a lower energy density (at 1 A/g) of 3.73 Wh/kg compared to 6.61 Wh/kg for PC at 25 C. At 100 ºC, the energy density for the supercapacitor containing electrolyte **2** increases to 12.91 Wh/kg and is greater than 9.65 Wh/kg for the supercapacitor containing PC. Increasing the temperature offers a 3.5 times improvement in energy density at a current density of 1 A/g. At 100 ºC, the supercapacitor containing electrolyte **2** also performs well at higher current densities (10 A/g) affording an energy density of 7.81 Wh/kg.

At 25 ºC, the initial capacitance values after five cycles for the supercapacitors with the PC and **2** electrolytes are 36.7 and 16.1 F/g, respectively (Figure 2.6-left). After 2000 cycles at 25 ºC, the capacitance values for both of the capacitors remain constant with

minimal loss over time, with the PC based supercapacitor providing greater capacitance. Raising the temperature significantly changes the capacitance of the supercapacitors. At 100 °C, these values correspondingly decrease to 36.1, and increase to 36.5 F/g for PC and **2**, respectively (Figure 2.6-right). Increasing the temperature affords a 2.2 times enhancement in performance for **2,** attributed to the decrease in electrolyte viscosity and increase in electrolyte conductivity, while a slight performance decrease occurs with the PC based supercapacitor. In contrast to the data collected at 25 °C, at 100 °C the capacitance values for the PC based supercapacitor decrease by 28% from 36.1 to 26.0 F/g after 2000 cycles with subsequent device failure at approximately 3200 cycles. This result is consistent with previous reports on PC based electrolytes operating at 60 °C or 70 °C where capacitor degradation occurs at higher temperatures.[110-111] The supercapacitor with electrolyte **2** cycles for more than 10000 cycles at 100 °C with a 30% decrease in capacitance.

2.5 Summary and Future Work

In summary, we described the synthesis and physicochemical characteristics of piperidinium ionic liquids possessing an alkyl ether chain as electrolytes when combined with LiTFSI for lithium ion supercapacitors. Replacing the alkyl chain with an alkyl ether within the piperidinium ionic liquid composition lowers the decomposition temperature, although all of the compounds are stable to >250 °C, and eliminates phase transitions (T_m or T_c), yielding a material which is liquid over a wide temperature range. The conductivity of the piperidinium ionic liquids are inversely correlated to added LiTFSI

concentration but directly correlated to temperature; viscosity displays the opposite relationship. The differences in electrolyte viscosity are most pronounced at lower temperatures, while at higher temperatures, all the electrolytes possess low values similar to each other. The conductivity of the electrolytes increase with increasing temperatures and electrolyte **2** exhibits the largest value of 9.2 mS/cm. DFT calculations reveal weak cation-anion binding energies between the piperidinium ionic liquid and TFSI, relative to LiF. A carbon electrode base lithium ion supercapacitor containing electrolyte **2** operates for 10000+ charge-discharge cycles and provides 28 F/g of capacitance at 100 ^{o}C, while an analogous device with a PC electrolyte fails after 3200 cycles. These findings support the continued development and performance evaluation of ionic liquid electrolytes for electrical energy storage devices operating at elevated temperatures.

2.6 General Procedures and Materials

2.6.1 Synthesis of Ionic Liquids

Compound **1, N-methyl-N-propyl-piperidinium Bis(trifluoro-methyl-sulfonyl)-imide,** was purchased from Iolitec Inc. with 99% purity. All other reagents were purchased from Sigma, Aldrich, or Acros and used without further purification. Purity is indicated on the labels. ^{1}H (500 MHz) and ^{13}C (126 MHz) NMR spectra were recorded on Varian INOVA spectrometers. Electrospray mass spectra were obtained on an Agilent 1100 LC/MSD Trap with ESI and APCI sources (LC/MS).

Synthesis of N-methyl-methoxy-methyl-piperidinium Bis(trifluoro-methane-sulfonyl)-imide (2): Bromomethyl methyl ether (Aldrich, technical grade, 90%) (0.2

mol) was added dropwise to a 1.0 M solution of N-methyl-piperidine (Aldrich, 99%) (0.2 mol) and Ethyl Acetate. The reaction was stirred at 50 ^{o}C for 12 hours. The solid halide product was recrystallized 3 times with Dichloromethane (DCM) and Ethyl Acetate. N-methyl-N-methoxymethyl-piperidinium bromide was obtained as a white solid product in 35% yield. The halide anion was then exchanged for a TFSI anion by dissolving N-methyl-N-methoxymethyl-piperidinium bromide in 20 mL of DCM and simultaneously dissolving an equimolar amount of LiTFSI salt in 20 mL of deionized water. The two mixtures were combined and stirred at room temperature overnight. The water phase of the mixture was then washed three times with 10 mL of DCM. 1 N $AgNO_3$ was used to confirm the complete elimination of the Bromide anion. The organic layer was dried on $MgSO_4$ and the solvent was removed under vacuum. N-methyl-N-methoxymethyl-piperidinium TFSI was isolated as a yellow liquid in 27% yield. ^{1}H-NMR (CD_3OD): δ1.60-1.74 (m, 2 H, CH_2-**CH_2**-CH_2), 1.84 (m, 4H, **CH_2**CH_2-**CH_2**), 3.19 (s, 3H, N-CH_3), 3.30-3.37 (m, 4H, CH_2-N-CH_2), 3.62 (s, 3H, O-CH_3), 5.03 (s, 2H, N-CH_2-O) ^{13}C-NMR: δ20.81 (2C, CH_2), 22.46 (1C, CH_2), 45.92 (1C, N-CH_3), 49.5 (1C, O-CH_3), 58.96 (2C, CH_2), 61.48 (1C, N-CH_2-O), 117.68, 120.23, 122.78, 125.33 (CF_3); LC/MS: Pos. 144.2 m/z, Neg. 279.1 m/z.

Synthesis of N-methyl-N-methoxy-ethoxyethyl-piperidinium Bis(trifluoro-methane-sulfonyl)-imide (3): 9.00 mmol of N-methylpiperidine was cooled to 0 ^{o}C in a dark vessel and flushed with Argon. 1-bromo-methoxyethoxy ethane (9.00 mmol) was added over 30 minutes and the mixture was warmed to room temperature and stirred for

12 hours. The solid halide product was heated to 50 ºC overnight while under vacuum to remove leftover reactants and N-methyl-N-methoxyethoxyethyl-piperidinium bromide (Acros Organics, 90% stabilized with sodium carbonate) was isolated as a brown solid. The halide anion was then exchanged for TFSI using the procedure described above. An orange liquid N-methyl-methoxyethoxyethyl-piperidinium TFSI was obtained. To remove the color impurities an activated charcoal column was run with sand, silica, and activated charcoal. N-methyl-N-methoxyethoxyethyl-piperidinium TFSI was isolated as a yellow liquid. ^{1}H-NMR(CD_3OD): δ1.69 (m, 2H, CH_2-**CH_2**-CH_2), 1.90 (m, 4H, **CH_2**-CH_2-**CH_2**), 3.16 (s, 3H, N-CH_3), 3.40 (s, 3H, O-CH_3), 3.46 (m, 2H, O-CH_2), 3.50 (m, 2H, CH_2-O), 3.55 (m, 2, CH_2-O), 3.60 (m, 4H, CH_2-N-CH_2), 3.9 (m, 2H, CH_2-N); ^{13}C-NMR ($CDCl_3$): δ19.72 (2C,CH_2), 20.44 (1C, CH_2), 49.27 (1C, N-CH_3), 59.9 (1C, O-CH_3), 62.4 (2C, CH_2), 64.11 (1C, CH_2-O), 70.25 (1C, N-CH_2-CH_2-O), 71.38 (1C, N-CH_2), 115.91, 118.47, 121.03, 123.58 (CF_3); LC/MS: Pos. 202.2 m/z. Neg. 279.1 m/z.

2.6.2 Procedure for General Characterization of Ionic Liquids

Before each of the following tests the samples were dried at 80 ºC while under vacuum for at least 6 hours. Thermal Gravimetric Analysis (TGA) experiments were completed with TGA Q50 and samples were heated from 20 to 500 ºC at a rate of 10 ºC min^{-1}. Thermal decomposition point was defined as the temperature where 6% weight loss of the original sample weight was recorded.

Thermal transitions were measured using a TA instruments Q100 Differential Scanning Calorimeter from -70 ^{o}C to 250 ^{o}C at a heating rate of 20 ^{o}C/min and cooling of 5 ^{o}C min^{-1} for three iterations. All samples weighed between 10 to 20 mg.

Viscosity was measured on TA Instruments AR 2000 Rheometer. Generally, a 25 mm aluminum plate geometry was used with the gap set to 1000 um. Prior to testing, a preshear at shear rate of 100 Hz for 10 s followed by a five min equilibrium was performed to eliminate physical memory of the sample. An oscillatory strain sweep was completed between .1 % and 12 % strain at 1 Hz to find the Linear Viscoelastic Region (LVR). Next, a frequency sweep from 0.1 to 12.5 Hz was completed at a strain % within the LVR. The dynamic viscosity was recorded at a specific frequency and strain %. Next, an oscillatory temperature sweep was conducted from 10 to 95 ^{o}C with increments of 10 ^{o}C and 1 min equilibrium at each temperature. Strain and frequency were set to 10% and 1 Hz, respectively.

Conductivity measurements were performed with a Conductivity Meter (K912, Consort, +/- 0.5% fs of range for conductivity and +/- 0.3 ^{o}C) equipped with a 4-electrode cell to prevent polarization error and fouling of the electrode. 4- electrode probe was calibrated with .01, 0.1 and 1 M KCl Standard Solutions. Testing was completed inside an Argon Glovebox (H_2O <1 ppm, O_2 <0.6 ppm) and a heating block was used to control the temperature; samples were equilibrated for 30 min at each temperature. Samples were dried at 80 ^{o}C while under vacuum overnight before testing.

2.6.3 General Procedures for Supercapacitor Fabrication

The supercapacitors were fabricated using a method previously described by our laboratory.[94] Activated Carbon (AC) working electrodes were fabricated using a standard method: 75 wt% AC, 15 wt% acetylene black (AB), and 10 wt% poly(vinylidene fluoride) binder in N-methyl-pyrrolidinone solvent were ground together in a mortar. AC and AB were dried at 80 and 120 C in a vacuum oven, respectively. The generated mixture was then coated on stainless steel sheets (1.58 cm diameter). All electrodes produced had approximately 1 to 2 mg of active material after drying under vacuum at 80 ^{o}C overnight. Coin cells were assembled using CR2032 coin cells (MTI Co.) and were composed of a spring, two identical electrodes (by weight) and two Celgard 480 membrane separators. During assembly, the separators were soaked in the ionic liquid electrolyte at 60 ^{o}C for 15 minutes. Once thoroughly soaked, the bottom of a coin cell was fitted with a spring, one electrode, and the separators were placed on top, followed by the second electrode and the cap. The cell was then crimped shut and left to rest at room temperature for 12 hours prior to testing.

2.6.4 General Procedures for Electrochemical Measurements

All electrochemical measurements were performed on VersaStat Battery Tester. A cyclic voltammogram was run on the coin cells to determine the electrochemical window for charge discharge cycling experiments. Multiple scans at different scan rates ranging from 100 mV/s to 20 mV/s were run on coin cells containing PC, electrolytes 1 and 2. A non-faradaic region (no oxidation and reduction peaks) between 0-2.5 V was observed

for all the three electrolytes. This voltage range was chosen as the potential window for all charge discharge cycling experiments.

For the charge discharge cycling, a current density of 1 A/g was chosen for all experiments and the cells were cycled between 0-2.5 V. The discharge capacitance was calculated from the following equation:

$$C_s=2I_{const}/(m*(dV/dt))$$

Where I is the constant current applied in A, in our experiments, dV/dt is the slope of discharge curve, and m is the mass of each electrode in g.

Charge discharge cycle experiments were carried out at different current densities (1, 2, 5 and 10 A/g) both at 100 degrees and room temperature for propylene carbonate and electrolyte 2. Energy density (Wh/kg) and power density (W/kg) were calculated using the following equations:

$$E=\frac{1}{8}\ C_S\Delta V^2$$

$$P=\frac{E}{\Delta t}$$

Where ΔV is the window potential (V) and Δt is the discharge time.

2.6.5 DFT Computational Calculations

The computation calculations were completed by my collaborates Alexander Hino and Prof. David Coker.

The binding energies (BE) were determined as follows:

$$BE=E^{CP}(CA)- E_{min}(C)- E_{min}(A)+ \Delta ZPVE$$

Where $E^{CP}(CA)$ is the counter-poise corrected energy of the cation-anion pair, $E_{min}(C)$ and $E_{min}(A)$ are the minimum energies of the cation and anion respectively, and $\Delta ZPVE$ is the change in zero-point vibrational energy between the separated ions and the ion pair. The counter-poise corrected energy is used to avoid basis-set superposition error (BSSE). All structures were optimized at the B3LYP/6-31G(d) level of theory and the resulting geometries were used to calculate energies at the B3LYP/6-311G(d,p) level of theory. This level of theory has been found to give reliable results when compared to previous studies. Using the [C_1mpyr][Cl], configuration 1 optimized geometry from literature we calculated a BE of -94.55 kcal/mol as compared to the reported value of -95.22 kcal mol^{-1} which was found at the MP2/aug-cc-pVTZ level of theory.[108] All calculations were performed with Gaussian 16. Calculations used a polarizable continuum model (PCM) with ε=15.2 to simulate the environmental effects.

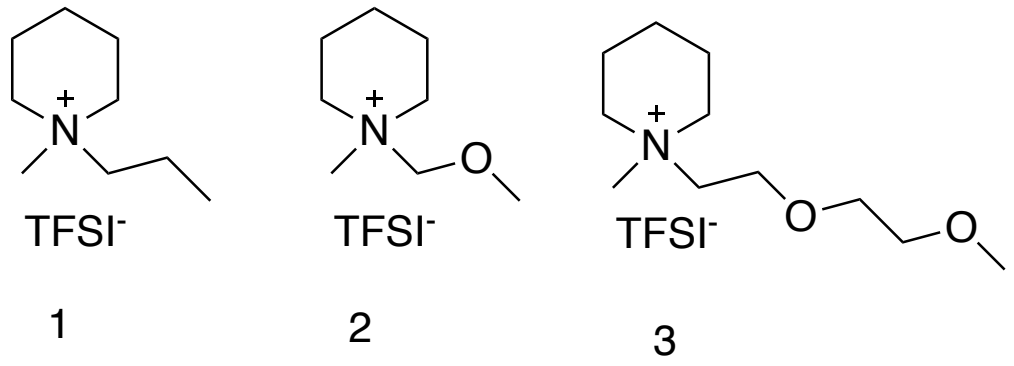

Fig. 2.1 Chemical structures of the ionic liquids investigated. N-methyl-N-propyl-piperidinium TFSI (**1**), N-methyl-N-methoxymethyl-piperidinium TFSI (**2**), and N-methyl-N-methoxyethoxyethyl-piperidinium TFSI (**3**).

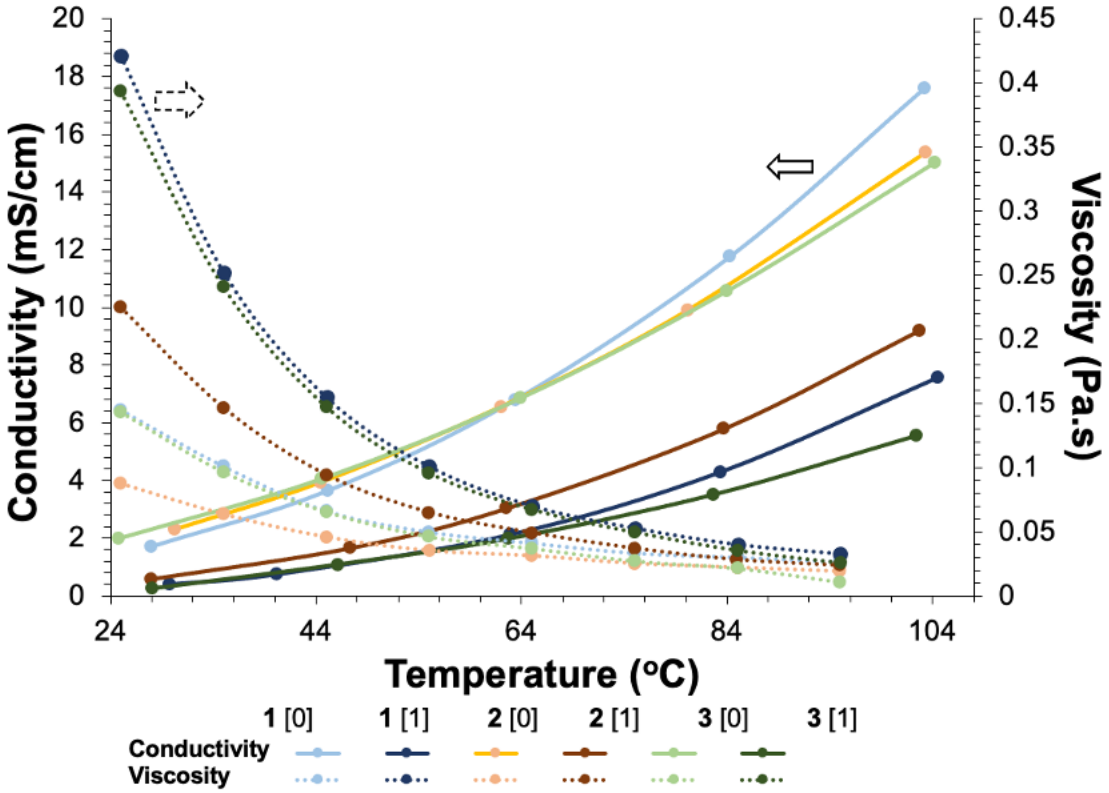

Fig. 2.2 Conductivity and viscosity data for **1**, **2**, and **3** with 0.0 M and 1.0 M LiTFSI salt concentration as a function of temperature. The conductivity and viscosity data are represented by solid and dotted lines, respectively, with the color of the line corresponding to the ionic liquid and the darker shades reflecting increased LiTFSI salt concentration (N>3). Individual graphs for the conductivity and viscosity as well as for the 0.5M LiTFSI compositions are found in the ESI.

Table 2.1 Calculated binding energies for the ion pairs

Ionic Liquids	Binding Energy (kcal mol^{-1})[1]
N-methyl-N-propyl-piperidinium TFSI, 1	-11.44
N-methyl-N-methoxymethyl-piperidinium TFSI, 2	-11.50
N-methyl-N-methoxyethoxyethyl-piperidinium TFSI, 3	-9.87
LiTFSI	-10.22, -11.02, -14.11
LiF	-2.34

[a]Energy calculations were performed in Gaussian 16 with a polarizable continuum model (PCM) with a dielectric constant ε = 15.2. Three configurations were found for LiTFSI and the resulting range of binding energies is reported. The binding energy for LiTFSI in a PCM with a dielectric constant ε = 78.4, more similar to PC, was calculated to be -6.73, -6.02, -7.14.

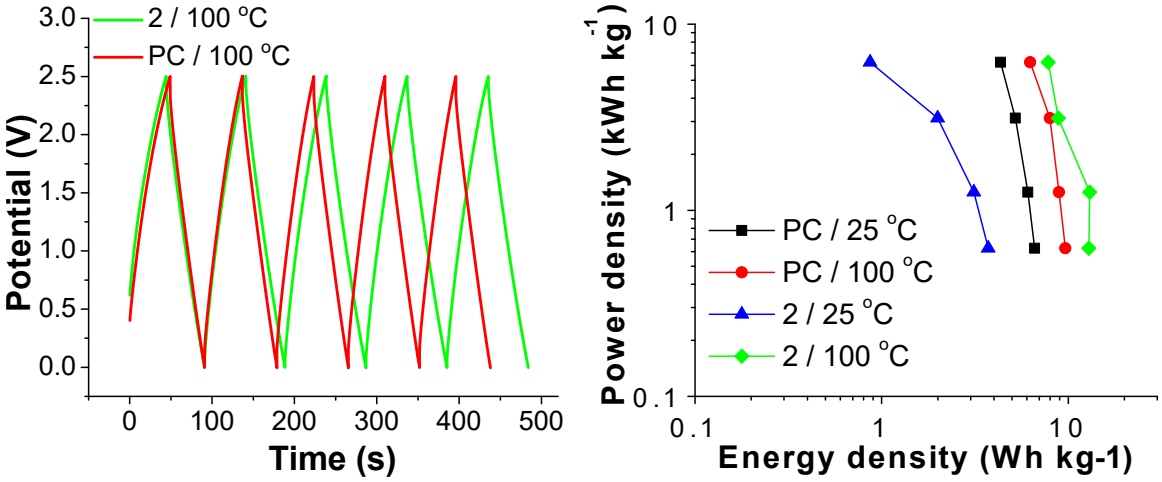

Fig. 2.3 (left) First five charge and discharge cycles of a supercapacitor with electrolyte **2** with 1.0 M LiTFSI at 100 °C. (right) Ragone plot for supercapacitors containing electrolyte **2** or PC (1, 2, 5 and 10 A/g) at 25 and 100 °C.

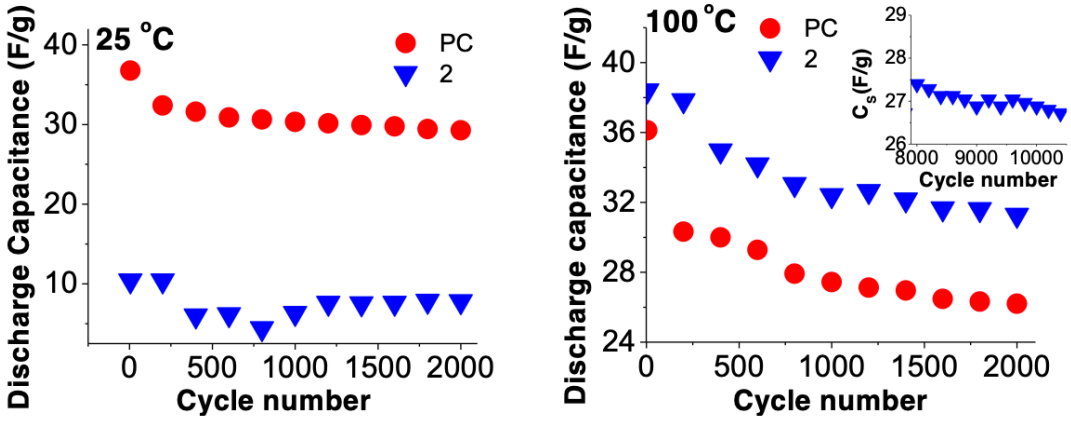

Fig. 2.4 (left) Capacitance values as a function of cycle number for supercapacitors with electrolytes PC and 2 with 1.0 M LiTFSI at 25 °C. (right) Capacitance values as a function of cycle number for supercapacitors with electrolytes PC and 2 with 1.0 M LiTFSI at 100 °C from 0 to 2000 cycles and continued operation (insert) to 10000+ cycles.

Chapter 3: Electrochemical Stability of Binary Mixtures of Ionic Liquids Paired with Various Lithium Salts: Uncommon and Common Ion Pairings

3.1 Introduction

3.1.1 Challenges for High Temperature Electrical Energy Storage Devices

The demand for electrical energy storage devices (EES) that function at both ambient and elevated temperatures is significant as global communities' desire to replace fossil fuels expands.[82, 112-113] Unfortunately, current EES devices rely on flammable and volatile carbonate-based electrolytes presenting a major limitation to producing thermally stable EES devices.[3, 73, 114] Ionic liquids (ILs) are nonflammable, nonvolatile, electrochemically stable molten salts of substantial interest as candidate electrolytes for use in thermally stable EES devices. ILs are limited however due to their relatively high viscosity and low conductivity at ambient temperature.[13, 115-116] The design of an IL electrolyte that satisfies all of the conditions to replace carbonate-based solvents is an unmet challenge.

3.1.2 Components of an Ideal Ionic Liquid Electrolyte

The manipulation of ILs is readily accomplished by changing the specific cation and anion species utilized, which drastically alters the physicochemical properties of the resultant IL. This ability to fine tune the IL by varying the cations and anions is an opportunity to adjust and balance the positive and negative physiochemical properties of the IL.[21, 117-123] We have taken advantage of the tunability of ILs and generated nine ILs with unique cation/anion pairs to characterize the effects of cation/anion pairings on the

physiochemical properties. We also developed a strategy to design new candidate IL electrolytes.

The specific cation and anion components utilized in our systems all show beneficial characteristics when utilized in an ILs or EES device. Phosphonium based ILs exhibit a wide thermal and electrochemical stability.[12, 93, 124-127] Imidazolium based ILs have low densities, resulting in low viscosities and high conductivities.[128-131] Moreover, the incorporation of an ether moiety into the side change of an IL is an established practice to decrease the viscosity and increase the conductivity. [132-134] As such compounds with and without an ether moiety were compared in this study.

The addition of lithium salts to the carbonate-based solvent is required to create an electrolyte, and previous reports document that the addition of lithium salts to IL electrolytes improves EES devices performance.[135] Lithium hexafluorophosphate ($LiPF_6$) is relatively inert and stable and is a common salt used in commercial electrolytes.[19, 136] Lithium bis(trifluoromethanesulfonyl)imide (TFSI) and $LiPF_6$ salts both contain fluoride atoms which are necessary for the formation of a stable solid electrode interface (SEI) on the surface of the electrode.[137-139] The dicyanamide anion (DCA^-) has a low molecular weight and the negative charge is highly delocalized which facilitates the generation of highly conductive ionic liquids.[117, 137, 140-143] Figure 3.1 displays the physical structure of the nine ILs evaluated.

Lastly, the generation of an IL electrolyte through the addition of a lithium salt introduces two new cations and anions to the IL, producing an IL mixture electrolyte; this can lead to drastic changes in the physiochemical properties of the resultant mixture.[144-

[147] As such, we measured the electrochemical stability of both the neat ILs and the IL mixture electrolytes versus Li/Li^+ and we catalogued the unique interactions present upon the addition of the salts. Table 3.1 displays the IL electrolyte mixtures that were evaluated.

3.2. Characterization of Neat Ionic Liquids

3.2.1 Thermal Behavior of Neat Ionic Liquids

Of the nine ILs synthesized, only three are solids; P111-TFSI, P111-PF_6, and P1o1-PF_6. The solid state of phosphonium based ILs originates from the symmetric nature of the phosphonium based ILs compared to the asymmetric 1-allyl-3-butyl-imidazolium (AC_4Im) cation. Asymmetry in the cation of the IL hinders packing of the cations and anions into an ordered crystalline structure resulting in low density and liquid compounds. Moreover, comparing P111-TFSI to P1o1-TFSI, P111-TFSI is a solid compound at room temperature and does not melt until 75 ^oC, while P1o1-TFSI is a liquid at room temperature with a melting point (T_m) of 19 ^oC (Table 3.2). The single chemical difference between P1o1-TFSI and P111-TFSI is the replacement of a methylene group in one side arm of the cationic structure with an ether moiety. This exchange exemplifies how a small alteration in the cationic structure significantly impacts the packing properties of the IL and the resulting physiochemical properties.

We measured the thermal stability, thermal phase shifts (T_m and T_c), conductivity and viscosity of each IL, except for the three solid compounds where no viscosity or conductivity measurements were performed. Comparing all of the compounds, the $TFSI^-$

based ILs display the highest thermal stability, followed by PF_6^- and then DCA^-, though all ILs are stable well above 100 ºC. DSC analysis of the compounds show no T_m or T_c for the AC_4Im based ILs in the range of -70 to 150 ºC. P111-DCA displays the lowest T_m compared to all the phosphonium based ILs with a melting point of 4.35 ºC.

3.2.2 Conductivity and Viscosity of the Neat Ionic Liquids

The viscosity and conductivity of the ILs display a linear relationship with temperature; as the temperature rises the conductivity of the IL increases and the viscosity decreases (Table 3.2). Examining the viscosity at 25 ºC, P1o1-DCA displays the lowest viscosity 0.043 Pa.s, with P111-DCA displaying a similar viscosity of 0.046 Pa.s. The overall range of viscosity values for the ILs is small, from 0.060 Pa.s for P1o1-TFSI to 0.043 Pa.s for P1o1-DCA. It is difficult to determine if these differences substantially impact the ILs performance in an EES device, but compared to traditional carbonate-based solvent electrolytes, these ILs are twenty times more viscous.[148]

To easily compare the conductivities of the ILs we evaluated the conductivity at 30 ºC (due to facilities issues in our laboratory ambient temperatures in the glovebox vary widely day to day from 19 ºC to 27 ºC, as such the samples were heated to 30 ºC). The conductivity of each IL closely follows the viscosity of the ILs. For example, the lowest viscosity IL P1o1-DCA has the highest conductivity of 8.83 mS/cm, while the highest viscosity IL P1o1-TFSI displays the lowest conductivity of 1.87 mS/cm. The other ILs displayed conductivities between those two values.

3.2.3 Electrochemical Stability of Neat Ionic Liquids

To understand the electrochemical stability of the IL salt mixtures, we first established the electrochemical stability window of the neat ILs in a three-electrode system utilizing Li/Li/Pt from -1 to 5 V at 25 ºC and 60 ºC. In this experiment, only the ILs which are liquids at room temperature were tested (Fig. 3.2-3.3). Different electrochemical behaviors are observed for the ILs at 25 ºC and 60 ºC. At 25 ºC, AC_4Im-TFSI, followed by AC_4Im-PF_6 displays the largest current response and smallest electrochemical stability window (3.2a). However, AC_4Im-DCA displays a nearly flat curve with current leakage of less than 10 µA from -1 to 5 V (Fig. 3.2b). It is theorized that the interaction between the DCA anion and the AC_4Im cation is stronger than the TFSI and PF_6 interactions, thus stabilizing the AC_4Im-DCA IL.

This trend is repeated with the phosphonium based ILs. P111-DCA only measures, at the highest, 28 µA current leakage from 4.5 V to 5 V. On the other hand, P1o1-TFSI and P1o1-DCA are unstable with oxidation reactions at 1 and 2 V for P1o1-TFSI and 3 V for P1o1-DCA (Fig. 3.2b). As the anodic stability of the IL is impacted by the anions of the system, and the cathodic stability is controlled by the cations of the system, the oxidation observed when scanning from -1 to 5 V for P1o1-TFSI is attributed to the oxidation of the TFSI anion. It is important to note that while two oxidation reactions are observed for P1o1-TFSI the current response remains below 10 µA, indicating the reactions are small in scale perhaps due to trace amounts of moisture. Plus, the scan for P1o1-TFSI was completed at 100 ºC instead of at 60 ºC, as such, the lower current response compared to P1o1-DCA is further evidence that P1o1-TFSI is more stable than P1o1-DCA. For P1o1-

DCA, the DCA anion oxidizes at 3 V, and when scanning with a cathodic current, a large current response is measured from 0 to -1 V, indicating the reduction of the P1o1 cation. Currents generated during the oxidation of P1o1-DCA are nearly seven time larger at 5 V than P1o1-TFSI, indicating greater instability of P1o1-DCA. The fact that the P1o1-DCA is not electrochemically stable similar to P111-DCA is unexpected; there is some indication that the introduction of an ether moiety will affect the electrochemical stability, but those effects have been minor and not to the magnitude observed in our experiments.[93, 149-150] However, given the only chemical difference between P111-DCA and P1o1-DCA is the incorporation of the ether moiety, it is theorized that the increased polarity from the ether group destabilizes the IL.

At 60 ºC, we measured an increased current for all ILs tested. In particular, P1o1-TFSI displays a dramatic current response with values near 150 μA at 4.5 V (Fig. 3.3b). This indicates instability of both the cation and anion at these potentials at elevated temperatures. P1o1-DCA shows a similar current response to the applied voltage as displayed at 25 ºC, however there is now a single oxidation peak centered at 2 V. This oxidation peak has been reported for DCA based ILs at higher temperatures, and it is hypothesized that at higher temperatures the DCA anion dimerizes.[137, 140] Interestingly, P111-DCA does not display this oxidation peak but does displays similar stability until 4 V at 25 ºC. The interaction between the cation of P111 and the DCA anion is stronger than the interaction between P1o1 and DCA. This interaction potentially stabilizes the DCA anion and hinders dimerization at elevated temperatures. AC_4Im-DCA showed

similar stability to P111-DCA. Lastly, the AC_4Im-PF_6 and AC_4Im-TFSI display greater instability at this elevated temperature (Fig. 3.3a).

3.3 Evaluation of Quaternary Mixtures

With the electrochemical behavior of the neat ILs established, we determined the electrochemical stability of binary mixtures of the ILs with LiTFSI, $LiPF_6$, and LiDCA in 1.0 M concentrations. ILs that are solid at room temperature were excluded from this experiment. The ILs tested in this section displayed a stable electrochemical curve while neat, as such only P111-DCA and AC_4Im-DCA were evaluated. Unfortunately, the lithium salts displayed different solubilities in the ILs. For example, $LiPF_6$ and LiTFSI are soluble to 0.3 M and 0.5 M, respectively, in P111-DCA.

3.3.1 Conductivity and Viscosity of Quaternary Mixtures

The addition of the salts significantly affects both the physical and electrochemical properties of the IL. Figure 3.4 a-b compares the conductivity and viscosity of the ILs with the salts relative to temperature. As is common for ILs, the addition of salt decreases the conductivity of the IL compared to neat and increases the viscosity. It is important to note that the P111-DCA with 0.3 M $LiPF_6$ displays similar conductivity to the neat P111-DCA due to the low concentration of salt. Comparing only the 1.0 M LiDCA composition, the conductivity of both ILs are greatly reduced. At 28 ^oC, P111-DCA and AC_4Im-DCA display conductivities of 1.37 mS/cm and 2.67 mS/cm, respectively—a loss of 4 mS/cm compared to their neat counterparts. Prior to the addition of salt, P111-DCA

displays a superior conductivity by 1 mS/cm more than AC_4Im-DCA; now AC_4Im-DCA is more conductive. The increased conductivity of 1.0 M LiDCA in AC_4Im-DCA compared to 1.0 M LiDCA in P111-DCA is because of the slightly polar nature of AC_4Im-DCA due to the olefin functional group, which increases the solubility of LiDCA, allowing for freer Li^+ and DCA^- in the solution, increasing the number of charge carriers in solution. Moreover, the viscosities of these ILs at 25 ^oC are both 0.12 Pa.s, a 3X increase compared to their neat viscosities which explains the dramatic decrease in conductivity.

3.3.2 Electrochemical Stability of Quaternary Mixtures

The addition of the salts greatly impacts the electrochemical stability of the ILs, particularly at 60 ^oC. At 25 ^oC, both P111-DCA and AC_4Im-DCA exhibit similar curves with increased currents measured above 3 V, indicating the presence of an oxidation reaction or electron transfer reaction for all salts (Fig. 3.5a). For both ILs, the LiTFSI mixtures exhibit the smallest current from -1 to 5 V, below 30 μA. The LiDCA and $LiPF_6$ mixtures behave similarly in P111-DCA and AC_4Im-DCA, displaying a wide electrochemical stability until about 3 V. Each then shows a slow increase of current to a maximum of 48 μA at 5 V for $LiPF_6$. LiDCA behaves similar to $LiPF_6$ in P111-DCA, but in AC_4Im-DCA, a higher current of 75 μA was measured at 5 V. The higher current measured with 1.0 M LiDCA in AC_4Im-DCA supports the idea that LiDCA separates into its component parts more fully in AC_4Im-DCA, leaving DCA^- free and more readily oxidized because it is not stabilized by Li^+ or the AC_4Im^+.

At 60 ºC, the trends described at 25 ºC no longer hold true. With AC_4Im-DCA, the most stable salt is now $LiPF_6$, with the highest current response of 41 µA at 5 V (Fig. 3.5b). Both LiDCA and LiTFSI display oxidation reactions at 1.5 V and 2 V, respectively. LiDCA in particular is unstable below 0 Vs. With P111-DCA, LiTFSI is not stable from -1 to 5 V, with a current response of over 500 µA. LiDCA displays three oxidation reactions at 0.5, 1.5 V, and 3.5 V, as well as instability below 0 Vs. $LiPF_6$ in P111-DCA displays a moderate current response at 5 V of 93 µA.

Upon comparing the 1.0 M LiDCA mixtures of P111-DCA and AC_4Im-DCA, since these formulations contain the same concentration of LiDCA, it is clear that the salt behaves differently in each IL. In AC_4Im-DCA and P111-DCA, redox reactions are observed but they are in a larger magnitude in AC_4Im-DCA, indicating a destabilized interaction of the salt in AC_4Im-DCA compared to P111-DCA. LiTFSI, though in a smaller concentration in P111-DCA than AC4Im-DCA, generates more current in P111-DCA and exhibits instability throughout the entire voltage range. The different electrochemical behavior of the salt in the IL mixtures at 25 ºC versus 60 ºC highlights how solubility and the composition of the salt in the IL affect the reactivity of the mixture. At 25 ºC, all three salts are moderately unreactive to the applied potential. As the temperature increases, and the viscosity of the IL decreases, the salts more fully dissociate into their component parts, freeing more cations and anions into the solution. As the free anions are not stabilized by AC_4Im^+ or Li^+, the anions are susceptible to oxidation reducing the electrochemical stability window of the mixtures.

3.4 Conclusion

Nine ILs were prepared and their electrochemical stabilities studied. All of the ILs and IL/salt mixtures are thermally stable above 200 ºC. The symmetric structure of the phosphonium cation results in half of the compounds being solids at room temperature, whereas all of the asymmetrical imidazolium compounds were liquids at ambient temperatures regardless of the paired anion. Moreover, both the PF_6 and TFSI anions pair weakly with both of the cations, resulting in small electrochemical stability windows at both 25 and 60 ºC. The DCA anion displays large stability with the P111 and AC_4Im cations, with electrochemical stability windows of over 5 V for both ILs. However, the DCA anion when paired with P1o1 cation is not stable, limiting the use of the ether moiety in the cations to reduce the viscosity of the ILs. Lastly, both AC_4Im-DCA and P111-DCA display varying electrochemical stability when mixed with three different lithium salts, with the $LiPF_6$ salt being most stable in both ILs. Additional work needs to be undertaken to fully understand the interactions between the lithium salts and ILs while in solution, but the results from this work are a promising step towards a clear understand of the interplay that ILs face as both neat liquids and as ionic liquid electrolytes.

3.5 Methods and Materials

All other reagents were purchased from Sigma Aldrich, or Acros and used without further purification. Lithium bis(trifluoromethanesulfonyl)imide (LiTFSI), 99 % (Sigma-Aldrich) and lithium hexafluorophosphate ($LiPF_6$), 99 +% (Strem) were purchased at the highest purity and stored in a glovebox with moisture levels below 5 ppm. ^1H (500 MHz),

^{13}C (126 MHz), and ^{31}P (500 MHz) NMR spectra were recorded on Varian INOVA spectrometers. Electrospray mass spectra were obtained on an Agilent 1100 LC/MS Trap with ESI and APCI sources (LC/MS). Sodium and lithium detection were completed on an Agilent 4210 MP-AES using standards purchased from Agilent.

3.5.1 Synthesis of Nine Ionic Liquids and Various Salts

Lithium dicyanamide (LiDCA) was synthesized following previously published methods.[151] Samples had purities between 98 to 99.9 % of the lithium ion.

Synthesis of silver dicyanamide (AgDCA) was synthesized by dissolving 10 mol NaDCA and 10 mol $AgNO_3$ in minimal amounts of water in the dark. Once dissolved, the $AgNO_3$ solution was added dropwise to the NaDCA solution and left to stir in the dark for 15 minutes at room temperature. The solution was then filtered and the solid was washed three times with fresh DI water. The product was dried under vacuum at 80 ^oC overnight. AgDCA was obtained in yields of 80%.

P1o1-TFSI, P1o1-DCA and P1o1-PF_6 were synthesized from the base material P1o1-Br (triethyl-methoxymethyl-phosphonium bromide). A pre-dried Schlenk flask was charged with 30 mL (30 mmol) of a 1.0 M triethyl-phosphine in Tetrahydrofuran (THF) solution and capped with a rubber stopper in a glovebox. Nitrogen was flowed through the Schlenk flask as the cap was replaced with a condenser sealed at the end with a nitrogen balloon. Then, 3.28 mL (33 mmol) of 1-bromo-methyl-methoxyl was added along with 10 mL of dry THF and refluxed at 78 ^oC for 12 hours. The product was dried at 80 ^oC for 12 hours while under vacuum to yield P1o1-Br as a white solid with a yield

of 99 %. ^{1}H-NMR (CD_3OD): δ1.21-28 (m, 3H, P-CH_2-**CH_3**), 2.17-25 (m, 6H, P-**CH_2**-CH_3), 3.48 (s, 3H, P-CH_2-O-**CH_3**), 4.41-21 (d, 2H, P-**CH_2**-O-CH_3). ^{13}C-NMR: δ5.59 (3C, P-CH_2-**CH_3**), 10.41 (3C, P-**CH_2**-CH_3), 61.11 (1C, P-CH_2-O-**CH_3**), 78.61 (1C, P-**CH_2**-O-CH_3); LC/MS: Pos. 163.1 m/z, Neg. -- m/z.

Anion exchange procedures:

Br^- to $TFSI^-$: Equimolar amounts of P1o1-Br and LiTFSI were dissolved in 50 ml of Dichloromethane (DCM) or 50 mL deionized (DI) water respectively. The two phases were mixed and stirred at room temperature for 12 hours to yield P1o1-TFSI. Next, the product was washed three times with fresh DI water. To ensure the removal of the halide, three drops of 1 N silver nitrate ($AgNO_3$) were added to an aliquot of the DCM phrase; a solid precipitate indicated the presence of halide anions and the extraction steps were repeated. The product was dried under vacuum for 12 hours at 80 °C to give P1o1-TFSI (triethyl-methoxymethyl-phosphonium bis(trifluoromethanesulfonyl)imide) in a 90 % yield. ^{1}H-NMR (CD_3OD): δ1.21-28 (m, 3H, P-CH_2-**CH_3**), 2.17-25 (m, 6H, P-**CH_2**-CH_3), 3.48 (s, 3H, P-CH_2-O-**CH_3**), 4.41-21 (d, 2H, P-**CH_2**-O-CH_3). ^{13}C-NMR: δ5.59 (3C, P-CH_2-**CH_3**), 10.41 (3C, P-**CH_2**-CH_3), 61.11 (1C, P-CH_2-O-**CH_3**), 78.61 (1C, P-**CH_2**-O-CH_3), 117.68, 120.23, 122.78, 125.33 (CF_3); LC/MS: Pos. 163.1 m/z, Neg. 279.1 m/z.

Br^- to DCA^-: Equimolar amounts of P1o1-Br and AgDCA were added to excess methanol creating a suspension. The suspension was covered with foil and left to stir for 24 hours at 30 °C. The solid silver halide was filtered off and washed with methanol. The solvent was removed from the filtrate using roto vap and a yellow liquid product was

obtained. The product was dried under vacuum at 80 ^{o}C for 12 hours. 50 mL of DCM and 50 mL of Nanopure water were added to the liquid product and the two phases extracted. The DCM phases were washed three times with Nanopure water. The three waters phases were combined and washed with 50 mL of DCM. The water was removed and the product was again dried under vacuum for 12 hours at 80 ^{o}C. Lastly, the product was purified on silica using acetone as the mobile phase to obtain a light yellow liquid, P1o1-DCA (triethyl-methoxymethyl-phosphonium dicyanamide) in yield of 94%. ^{1}H-NMR (CD_3OD): δ1.21-28 (m, 3H, P-CH_2-**CH_3**), 2.17-25 (m, 6H, P-**CH_2**-CH_3), 3.48 (s, 3H, P-CH_2-O-**CH_3**), 4.41-21 (d, 2H, P-**CH_2**-O-CH_3). ^{13}C-NMR: δ5.59 (3C, P-CH_2-**CH_3**), 10.41 (3C, P-**CH_2**-CH_3), 61.11 (1C, P-CH_2-O-**CH_3**), 78.61 (1C, P-**CH_2**-O-CH_3), 19.39 (1C, P-**CH_2**-CH_3), 119.89 ($N(CN)_2$); LC/MS: Pos. 163.1 m/z, Neg. --m/z.

Br^- to PF_6^-: P1o1-Br was placed in a Schlenk flask and dissolved in dry acetonitrile in a glovebox. Once dissolved an equal molar amount of silver hexafluorophosphate ($AgPF_6$) was added creating a suspension. The suspension was stirred for fifteen minutes then immediately filtered through 0.02 um thick PTFE syringe filters. The filtrate was taken out of the glovebox and dried on roto-vap. To remove any remaining silver, the solid product was resuspended in acetone. Activated charcoal was added and allowed to stir for fifteen minutes. The product was filtered through a celite pad to remove the charcoal. P1o1-PF_6 (triethyl-methoxymethyl-phosphonium hexafluorophosphate) was dried on high vacuum for 12 hours at 80 ^{o}C to obtain the product in 87 % yield. ^{1}H-NMR (CD_3OD): δ1.21-28 (m, 3H, P-CH_2-**CH_3**), 2.17-25 (m, 6H, P-**CH_2**-CH_3), 3.48 (s, 3H, P-

CH_2-O-**CH_3**), 4.41-21 (d, 2H, P-**CH_2**-O-CH_3). ^{13}C-NMR: δ5.59 (3C, P-CH_2-**CH_3**), 10.41 (3C, P-**CH_2**-CH_3), 61.11 (1C, P-CH_2-O-**CH_3**), 78.61 (1C, P-**CH_2**-O-CH_3), 19.39 (1C, P-**CH_2**-CH_3). ^{31}P-NMR: δ145 (P111-**P**F_6), 38 (**P**1o1-PF_6); LC/MS: Pos. 163.1 m/z, Neg. 143.9 m/z.

P111-TFSI, P111-DCA, and P111-PF_6 were synthesized from the base material P111-I (triethyl-propyl-phosphonium Iodide). P111-I was synthesized using the same procedure as P111-Br except 1-Iodopropane was used instead of 1-bromo-methoxymethyl. P111-I was a solid white powder with a yield of 99 %. ^{1}H-NMR ($CDCl_3$): δ1.04-1.07 (t, 3H, P-CH_2-CH_2-**CH_3**), 1.17-24 (m, 9H, P-CH_2-**CH_3**), 1.50-1.59 (m, 2H, P-CH_2-**CH_2**-CH_3), 2.07-2.12 (m, 2H, P-**CH_2**-CH_2-CH_3), 2.13-2.21 (m, 6H, P-**CH_2**-CH_3). ^{13}C-NMR: δ5.61 (1C, P-CH_2-CH_2-**CH_3**), 11.56 (1C, P-CH_2-**CH_3**), 15.34 (1C, P-CH_2-**CH_2**-CH_3), 15.47 (1C, P-**CH_2**-CH_2-CH_2), 19.39 (1C, P-**CH_2**-CH_3); LC/MS: Pos. 161.1 m/z, Neg. 127.1 m/z.

Anion exchange procedures:

I^- to $TFSI^-$: The same procedure as described above for P1o1-TFSI was completed to obtain P111-TFSI (triethyl-propyl-phosphonium bis(trifluoro-methane-sulfonyl)imide) as a white solid with a yield of 83 %. ^{1}H-NMR ($CDCl_3$): δ1.04-1.07 (t, 3 H, P-CH_2-CH_2-**CH_3**), 1.17-24 (m, 9H, P-CH_2-**CH_3**), 1.50-1.59 (m, 2H, P-CH_2-**CH_2**-CH_3), 2.07-2.12 (m, 2H, P-**CH_2**-CH_2-CH_3), 2.13-2.21 (m, 6H, P-**CH_2**-CH_3). ^{13}C-NMR: δ5.61 (1C, P-CH_2-CH_2-**CH_3**), 11.56 (1C, P-CH_2-**CH_3**), 15.34 (1C, P-CH_2-**CH_2**-CH_3), 15.47 (1C, P-**CH_2**-

CH_2-CH_2), 19.39 (1C, P-**CH_2**-CH_3), 117.68, 120.23, 122.78, 125.33 (CF_3); LC/MS: Pos. 161.1 m/z, Neg. 279.1 m/z.

I^- to DCA^-: The same procedure as described above for P1o1-DCA was completed to obtain P111-DCA (triethyl-propyl-phosphonium dicyanamide) as a white solid with a yield of 63 %. ^{1}H-NMR ($CDCl_3$): δ1.04-1.07 (t, 3 H, P-CH_2-CH_2-**CH_3**), 1.17-24 (m, 9H, P-CH_2-**CH_3**), 1.50-1.59 (m, 2H, P-CH_2-**CH_2**-CH_3), 2.07-2.12 (m, 2H, P-**CH_2**-CH_2-CH_3), 2.13-2.21 (m, 6H, P-**CH_2**-CH_3). ^{13}C-NMR: δ5.61 (1C, P-CH_2-CH_2-**CH_3**), 11.56 (1C, P-CH_2-**CH_3**), 15.34 (1C, P-CH_2-**CH_2**-CH_3), 15.47 (1C, P-**CH_2**-CH_2-CH_2), 19.39 (1C, P-**CH_2**-CH_3), 119.89 ($N(CN)_2$); LC/MS: Pos. 161.1 m/z, Neg. -- m/z.

I^- to PF_6^-: The same procedures as described above for P1o1-PF_6 were completed except to remove leftover silver after the anion exchange the crude material was dissolved in hot isopropanol and filtered through a 0.02 um PTFE filter. The filtrate was slowly cooled to obtain P111-PF_6 (triethyl-propyl-phosphonium hexafluorophosphate) as white crystals which were collected by vacuum filtration in a yield of 27 %.[152] ^{1}H-NMR (CD_3CN): δ1.04-1.07 (t, 3 H, P-CH_2-CH_2-**CH_3**), 1.17-24 (m, 9H, P-CH_2-**CH_3**), 1.50-1.59 (m, 2H, P-CH_2-**CH_2**-CH_3), 2.07-2.12 (m, 2H, P-**CH_2**-CH_2-CH_3), 2.13-2.21 (m, 6H, P-**CH_2**-CH_3). ^{13}C-NMR: δ5.61 (1C, P-CH_2-CH_2-**CH_3**), 11.56 (1C, P-CH_2-**CH_3**), 15.34 (1C, P-CH_2-**CH_2**-CH_3), 15.47 (1C, P-**CH_2**-CH_2-CH_2), 19.39 (1C, P-**CH_2**-CH_3). ^{31}P-NMR: -145 (P111-**P**F_6), 38 (**P**111-PF_6); LC/MS: Pos. 161.1 m/z, Neg. 144.1 m/z.

AC_4Im-TFSI, AC_4Im-DCA, and AC_4Im-PF_6 were synthesized from the base material AC_4Im-Cl (1-allyl-3-butyl-imidazolium Chloride). A pre-dried Schlenk flask

was charged with 1-chlorobutane and equal molar amount of 1-allyl-imidazole and 1.0 M dry acetonitrile were added. The reaction was left to reflux at 80 ^{o}C for 72 hours while under nitrogen. The acetonitrile was removed via roto-vap. A silica column was used to purify the product with an acetone/methanol mobile phase: the concentration of methanol was slowly increased to 100% to obtain the desired product. Silica was then removed from the viscous liquid by completely drying under vacuum for 12 hours at 80 ^{o}C. Once dry, acetonitrile was added dissolving the liquid, and the silica was removed using filter paper. The product was then dried on high vacuum at 80 ^{o}C and a yellow viscous liquid was obtained in a yield of 65%. ^{1}H-NMR (CD_3OD): δ1.0 (t, 3 H,CH_2-CH_2-CH_2-**CH_3**), 1.40 (m, 2H, CH_2-CH_2-**CH_2**-CH_3), 1.89 (m, 2H, CH_2-**CH_2**-CH_2-CH_3), 4.24 (t, 2H, CH_2-CH_2-CH_2-**CH_3**), 4.86 (d, 2H, CH_2-CH=**CH_2**), 5.47 (d, 2H, **CH_2**-CH=CH_2), 6.09 (m, 1H, CH_2-**CH**=CH_2), 7.61 (s, 1H, N-C**H**=CH-N^+), 7.67 (s, 1H, N-C**H**=CH-N^+). ^{13}C-NMR: δ13.73 (1H,CH_2-CH_2-CH_2-**CH_3**), 20.46 (1C, CH_2-CH_2-**CH_2**-CH_3), 33.04 (1C, CH_2-**CH_2**-CH_2-CH_3), 50.73 (1C, **CH_2**-CH_2-CH_2-CH_3), 52.73 (1C, **CH_2**-CH=CH_2), 121.94 (2C, N-C**H**=CH-N^+), 123.75 (1C, CH_2-CH=**CH_2**), 131.94 (1C, CH_2-**CH**=CH_2); LC/MS: Pos. 165.1 m/z, Neg. -- m/z.

Anion exchange procedures:

Cl^- to $TFSI^-$: The same procedure as described above for P1o1-TFSI was completed to obtain AC_4Im-TFSI (1-allyl-3-butyl-imidazolium bis(trifluoromethanesulfonyl)imide) as a yellow liquid. ^{1}H-NMR (CD_3OD): δ1.0 (t, 3 H,CH_2-CH_2-CH_2-**CH_3**), 1.40 (m, 2H, CH_2-CH_2-**CH_2**-CH_3), 1.89 (m, 2H, CH_2-**CH_2**-CH_2-CH_3), 4.24 (t, 2H, CH_2-CH_2-CH_2-

CH_3), 4.86 (d, 2H, CH_2-CH=**CH_2**), 5.47 (d, 2H, **CH_2**-CH=CH_2), 6.09 (m, 1H, CH_2-**CH**=CH_2), 7.61 (s, 1H, N-C**H**=CH-N^+), 7.67 (s, 1H, N-C**H**=CH-N^+). ^{13}C-NMR: δ13.73 (1H,CH_2-CH_2-CH_2-**CH_3**), 20.46 (1C, CH_2-CH_2-**CH_2**-CH_3), 33.04 (1C, CH_2-**CH_2**-CH_2-CH_3), 50.73 (1C, **CH_2**-CH_2-CH_2-CH_3), 52.73 (1C, **CH_2**-CH=CH_2), 121.94 (2C, N-C**H**=CH-N^+), 123.75 (1C, CH_2-CH=**CH_2**), 131.94 (1C, CH_2-**CH**=CH_2), 117.68, 120.23, 122.78, 125.33 (CF_3); LC/MS: Pos. 165.1 m/z, Neg. 279.1 m/z.

Cl^- to DCA^-: The same procedure as described above for P1o1-DCA was completed to obtain AC_4Im-DCA (1-allyl-3-butyl-imidazolium dicyanamide) as a yellow liquid in a yield of 53 %. ^{1}H-NMR (CD_3OD): δ1.0 (t, 3 H,CH_2-CH_2-CH_2-**CH_3**), 1.40 (m, 2H, CH_2-CH_2-**CH_2**-CH_3), 1.89 (m, 2H, CH_2-**CH_2**-CH_2-CH_3), 4.24 (t, 2H, CH_2-CH_2-CH_2-**CH_3**), 4.86 (d, 2H, CH_2-CH=**CH_2**), 5.47 (d, 2H, **CH_2**-CH=CH_2), 6.09 (m, 1H, CH_2-**CH**=CH_2), 7.61 (s, 1H, N-C**H**=CH-N^+), 7.67 (s, 1H, N-C**H**=CH-N^+). ^{13}C-NMR: δ13.73 (1H,CH_2-CH_2-CH_2-**CH_3**), 20.46 (1C, CH_2-CH_2-**CH_2**-CH_3), 33.04 (1C, CH_2-**CH_2**-CH_2-CH_3), 50.73 (1C, **CH_2**-CH_2-CH_2-CH_3), 52.73 (1C, **CH_2**-CH=CH_2), 121.94 (2C, N-C**H**=CH-N^+), 123.75 (1C, CH_2-CH=**CH_2**), 131.94 (1C, CH_2-**CH**=CH_2), 120.48 (2C, $N(CN)_2$); LC/MS: Pos. 165.1 m/z, Neg. -- m/z.

Cl^- to PF_6^-: The same procedure as described above for P1o1-PF_6 were completed to obtain AC_4Im-PF_6 (1-allyl-3-butyl-imidazolium hexafluorophosphate) in yield of 43 %. ^{1}H-NMR (CD_3CN): δ1.0 (t, 3 H,CH_2-CH_2-CH_2-**CH_3**), 1.40 (m, 2H, CH_2-CH_2-**CH_2**-CH_3), 1.89 (m, 2H, CH_2-**CH_2**-CH_2-CH_3), 4.24 (t, 2H, CH_2-CH_2-CH_2-**CH_3**), 4.86 (d, 2H, CH_2-CH=**CH_2**), 5.47 (d, 2H, **CH_2**-CH=CH_2), 6.09 (m, 1H, CH_2-**CH**=CH_2), 7.61 (s, 1H, N-

C**H**=CH-N^+), 7.67 (s, 1H, N-C**H**=CH-N^+). ^{13}C-NMR: δ13.73 (1H,CH_2-CH_2-CH_2-**CH_3**), 20.46 (1C, CH_2-CH_2-**CH_2**-CH_3), 33.04 (1C, CH_2-**CH_2**-CH_2-CH_3), 50.73 (1C, **CH_2**-CH_2-CH_2-CH_3), 52.73 (1C, **CH_2**-CH=CH_2), 121.94 (2C, N-C**H**=CH-N^+), 123.75 (1C, CH_2-CH=**CH_2**), 131.94 (1C, CH_2-**C**H=CH_2), 120.48 (2C, $N(CN)_2$), ^{31}P-NMR: -145 (AC_4Im-**P**F_6); LC/MS: Pos. 165.1 m/z, Neg. 143.9 m/z.

3.5.2 Characterization of Ionic Liquid Electrolytes

Before each of the following tests, the samples were dried at 80 ºC while under vacuum for at least 6 hours. Thermal Gravimetric Analysis (TGA) experiments were completed with TGA Q50, and samples were heated from 20 to 500 ºC at a rate of 10 ºC min^{-1}. Thermal decomposition point was defined as the temperature where 10 % weight loss of the original sample weight was recorded.

Thermal transitions were measured using TA instruments Q100 Differential Scanning Calorimeter from -70 ºC to 250 C at a heating rate of 20 ºC min^{-1} and cooling of 5 ºC min^{-1} for three iterations. All samples weighed between 10 to 20 mg. Viscosity was measured on TA Instruments DHR-2 Rheometer. A 25 mm aluminum plate geometry was used with the gap set to 1000 um. Prior to testing, a pre-shear at a rate of 100 Hz for 10 s followed by a five min equilibrium was performed to eliminate physical memory of the sample. An oscillatory strain sweep was completed between .1 % and 12 % strain at 1 Hz to find the Linear Viscoelastic Region (LVR). Next, a frequency sweep from 0.1 to

12.5 Hz was completed at a strain % within the LVR. The dynamic viscosity was recorded at a specific frequency and strain %.

An oscillatory temperature sweep was conducted from 10 to 95 ^{o}C with increments of 10 ^{o}C and 1 min equilibrium at each temperature with strain and frequency set to 10% and 1 Hz, respectively. Samples were dried at 80 ^{o}C overnight while under a vacuum prior to testing.

Conductivity measurements were performed with a Conductivity Meter (K912, Consort, +/- 0.5% fs of range for conductivity and +/- 0.3 ^{o}C) equipped with a 4-electrode cell to prevent polarization error and fouling of the electrode. The 4- electrode probe was calibrated with .01, 0.1 and 1 M KCl Standard Solutions. Testing was completed inside an Argon Glovebox (H_2O <1 ppm, O_2 <0.6 ppm) and a heating block was used to control the temperature. Samples were equilibrated for 30 min at each temperature. Samples were dried at 80 ^{o}C while under vacuum overnight before testing.

The electrochemical stability window was measured using a 3-electrode Split Test Cell (MTI Co.) by cyclic voltammetry at a scan rate of 5 mVs^{-1} and a potential window of -1 to 5.0 V at room temperature and 60 °C. The cell was assembled in an argon-filled glove box using a Li/Li/Pt configuration

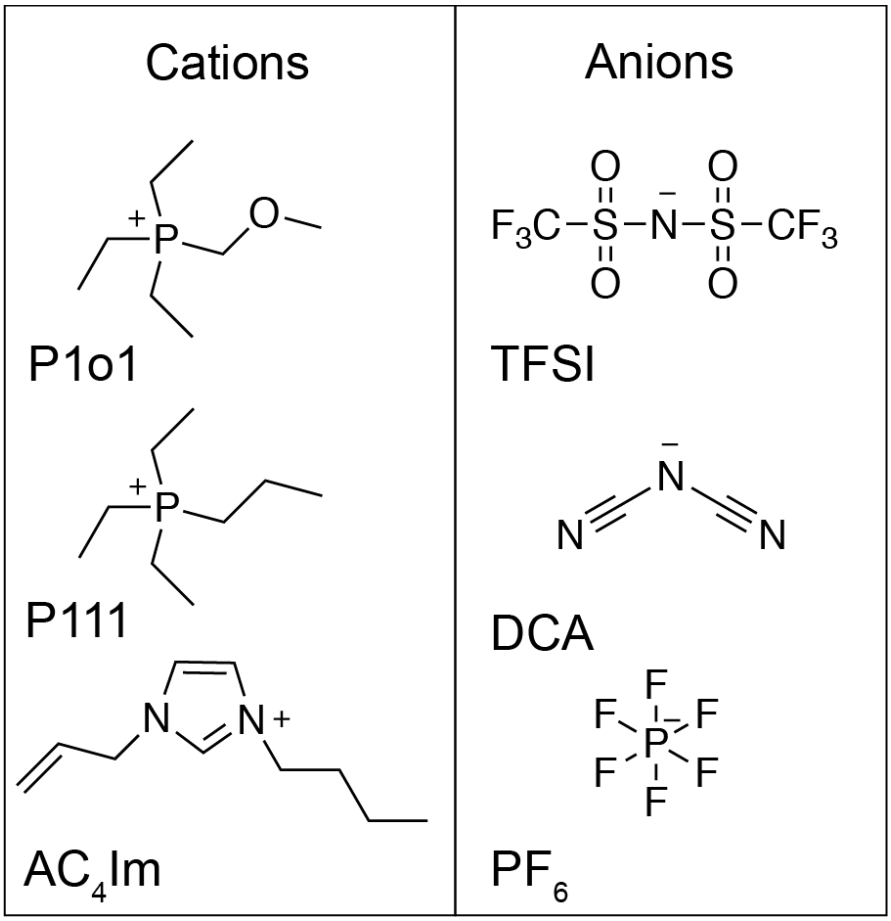

Fig. 3.1 Structures of the cation and anion components evaluated. Triethyl-methoxymethyl-phosphonium (P1o1), Triethyl-propyl-phosphonium (P111), 1-allyl-3-butyl-imidazolium (AC_4Im), and bis(trifluoromethanesulfonyl)imide (TFSI), dicyanamide (DCA), and hexafluorophosphate (PF_6).

Table 3.1 RTILs and Lithium Salt Mixtures.

Mixture No.	**1**	**2**	**3**	**4**	**5**	**6**	**7**	**8**
IL	P1o1-TFSI	P1o1-TFSI	P1o1-TFSI	P1o1-TFSI	P1o1-DCA	P1o1-DCA	P1o1-DCA	P1o1-DCA
Salt	No Salt	$LiPF_6$	LiDCA	LiTFSI	No salt	$LiPF_6$	LiDCA	LiTFSI
Mixture No.	**13**	**14**	**15**	**16**	**17**	**18**	**19**	**20**
IL	AC4Im-DCA	AC_4Im-DCA	AC_4Im-DCA	AC_4Im-DCA	P111-PF6	P111-PF_6	P111-PF_6	P111-PF_6
Salt	No Salt	$LiPF_6$	LiDCA	LiTFSI	No salt	$LiPF_6$	LiDCA	LiTFSI
Mixture No.	**25**	**26**	**27**	**28**	**29**	**30**	**31**	**32**
IL	AC4Im-PF6	AC_4Im-PF_6	AC_4Im-PF_6	AC_4Im-PF_6	AC4Im-TFSI	AC_4Im-TFSI	AC_4Im-TFSI	AC_4Im-TFSI
Salt	No salt	$LiPF_6$	LiDCA	LiTFSI	No salt	$LiPF_6$	LiDCA	LiTFSI

12	**11**	**10**	**9**
P111-DCA	P111-DCA	P111-DCA	P111-DCA
LiTFSI	LiDCA	$LiPF_6$	No Salt
24	**23**	**22**	**21**
P1o1-PF_6	P1o1-PF_6	P1o1-PF_6	P1o1-PF6
LiTFSI	LiDCA	$LiPF_6$	No salt
36	**35**	**34**	**33**
P111-TFSI	P111-TFSI	P111-TFSI	P111-TFSI
LiTFSI	LiPF6	LiDCA	No salt

Table 3.2 Thermal and Physiochemical Properties of the Neat ILs.

ILs	T_d (°C)	T_m (°C)	T_c (°C)	mS/cm	Pa.s	EW (V) 25 °C	EW (V) 60 °C
P1o1-TFSI	361.64	19.10	-23.15	1.87	0.037	0 to 2	0
P1o1-DCA	269.68	--	--	8.83	0.043	0	0
P1o1-PF_6	282.58	184.09	175.30	---	---	---	---
P111-TFSI	412	75.80	59.94	---	---	---	---
P111-DCA	358.75	4.35	-32.09	7.13	0.046	-1 to 5	-1 to 4
P111-PF_6	332.08	138.40	130.66	---	---	---	---
AC_4Im-TFSI	374.54	--	--	3.23	0.050	1.2 to 2.2	1.5 to 2
AC_4Im-DCA	229.82	--	--	6.81	0.054	-1 to 5	-1 to 4
AC_4Im-PF_6	257.88	--	--	0.727	0.349	0 to 5	0

Conductivity is noted at approximately 30 °C. Electrochemical stability window is V vs Li/Li^+. (--) indicates no value measured (---) no experiment was completed.

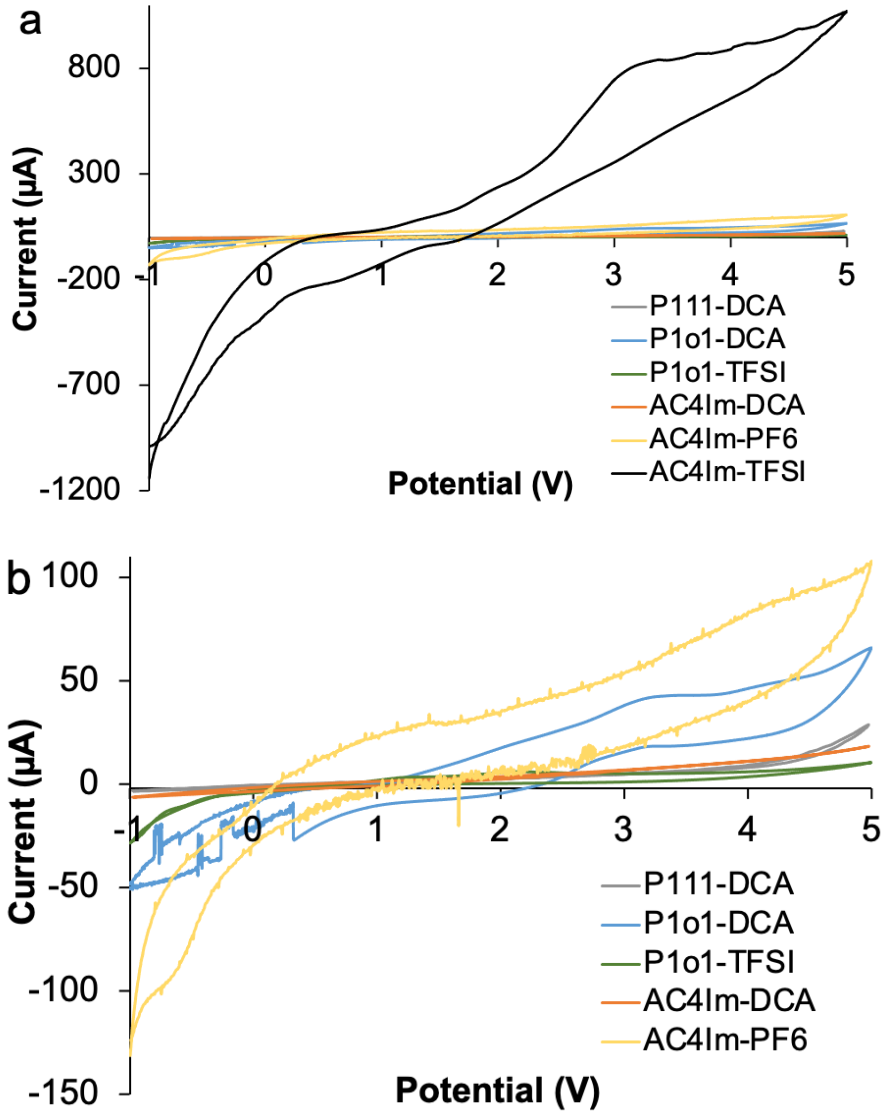

Fig. 3.2 (a) Cyclic voltammograms for all six RTILs with no salt added, the fifth cycle is shown, at 25 °C. (b) AC_4Im-TFSI has been removed to better view the cyclic voltammograms of the other five RTILs with no salt added at 25 °C.

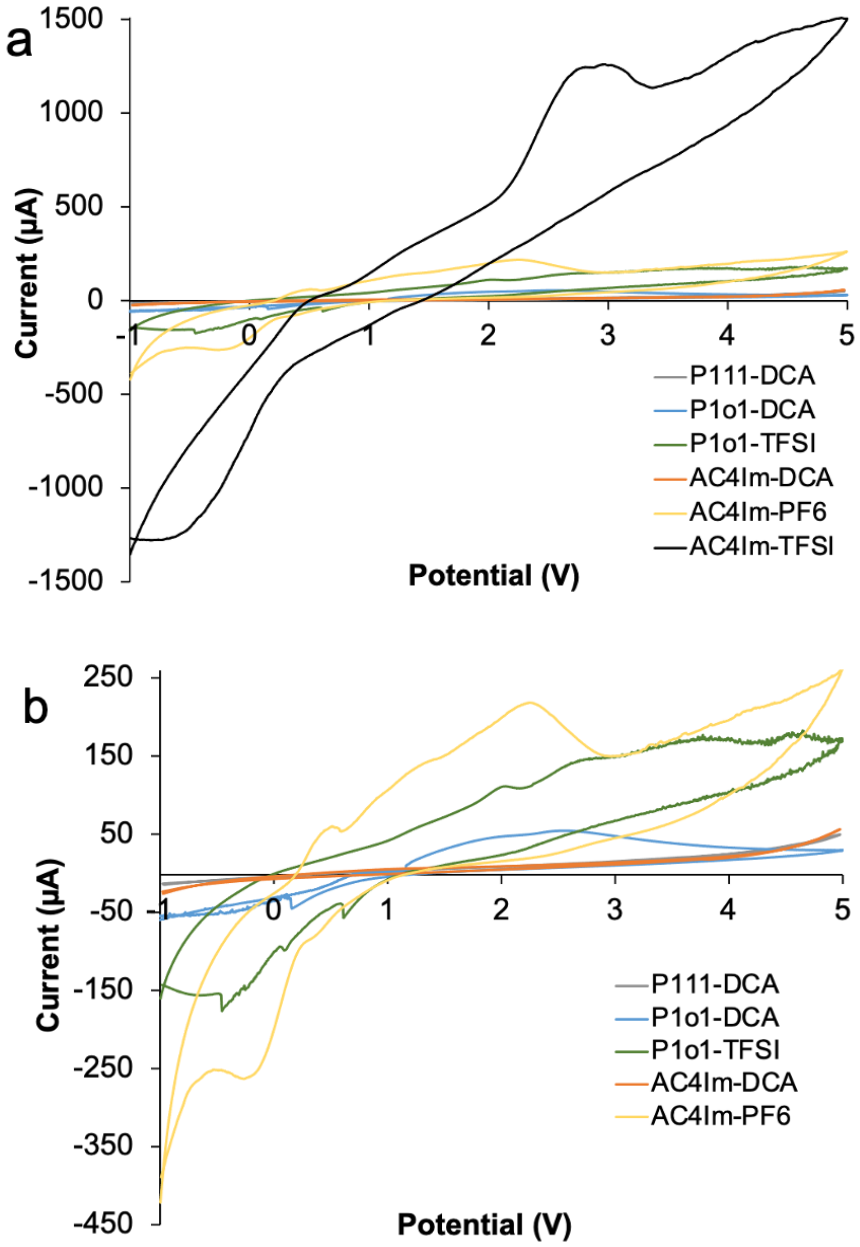

Fig. 3.3 (a) Cyclic voltammograms for all six RTILs with no salt added, the fifth cycle is shown, at 60 °C. (b) AC_4Im-TFSI has been removed to better view the cyclic voltammograms of the other five RTILs with no salt added at 60 °C.

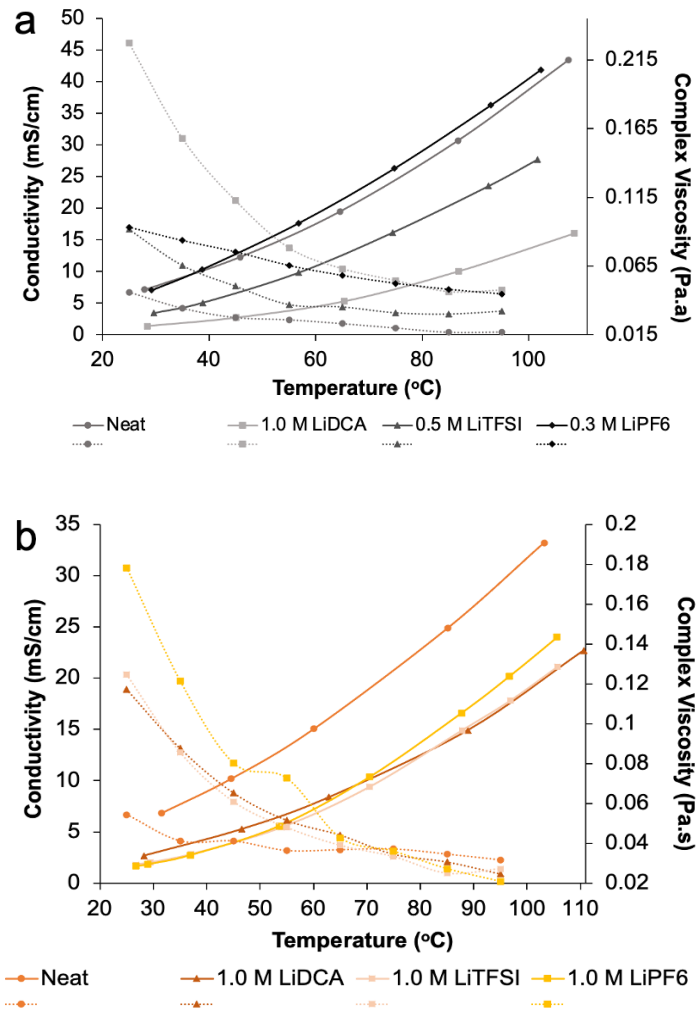

Fig. 3.4 (a) Conductivity and viscosity of P111-DCA neat and with varying concentrations of lithium salts. (b) Conductivity and viscosity of AC_4Im-DCA neat and with varying concentrations of lithium salts. The dotted lines correspond to the measured viscosity while the solid lines represent the conductivity of the RTILs.

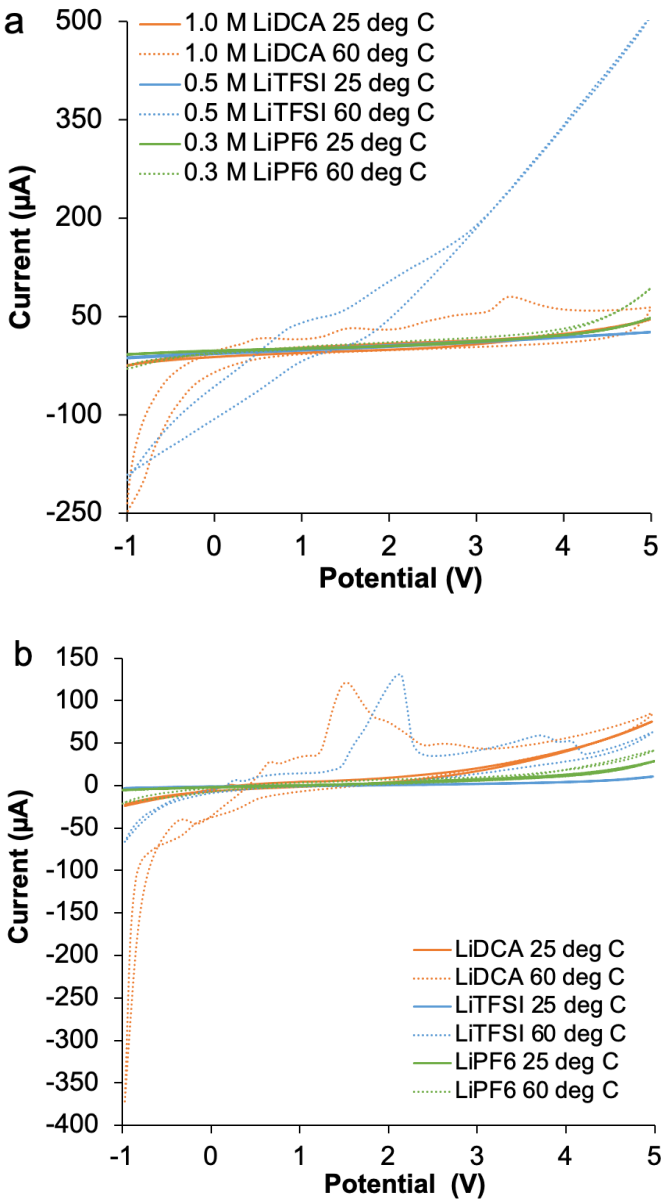

Fig. 3.5 (a) Cyclic voltammograms of P111-DCA with varying concentrations of lithium salts at 25 and 60 °C. (b) Cyclic voltammograms of AC_4Im-DCA with 1.0 M of various lithium salts at 25 and 60 °C.

Chapter 4 Manipulation and Control of Physiochemical Properties of Room Temperature Ionic Liquids for Use as Electrolytes at High Temperature

4.1 Introduction to Lithium Ion Batteries

4.1.1 Role and Limitation of Carbonate-Based Electrolytes in Lithium Ion Batteries

Lithium ion batteries (LIBs) have the highest demonstrated energy density (J/m^3) capabilities among electrical energy storage (EES) devices, and thus, LIBs dominate the portable electronics field.[3, 77, 153-154] Unfortunately, LIBs are only operational at ambient temperatures between 0 to 40 ^oC, limiting their use in high temperature environments like electric vehicles and oil and mining.[77] The main limitation hindering high temperature operation of LIBs is the flammable and volatile carbonate-based solvent electrolytes used in the devices.[19, 155-157]

The electrolytes main function is to shuttle lithium ions between the cathode and anode during charging/discharging. The electrolyte is composed of a mixture of linear and cyclic carbonate-based solvents with an electrochemically stable inorganic lithium salt (lithium hexafluorophosphate, $LiPF_6$).[158-159] While carbonate-based solvents are unsafe at high temperatures, their ability to transport Li ions within the battery cell are, as of now, unprecedented by any other solvent at ambient temperatures. Moreover, during the initial charge and discharge cycle, cyclic carbonate electrolytes decompose on the anode surface forming a passivation layer called the solid electrolyte interface (SEI). The SEI hinders further decomposition of the electrolyte and prevents co-intercalation of the

electrolyte solvent into the anode with the Li ions, extending the lifetime of the battery.[19, 160-162]

4.1.2 Characteristics of Ionic Liquids

Ionic liquids (ILs) are salt-like materials held together via electrostatic interactions, composed of a cationic organic compound (e.g., phosphonium, piperidinium) and an inorganic or organic anion (e.g., $TFSI^-$). These compounds are generally nonvolatile, nonflammable, and thermally and electrochemically stable. Due to these advantageous properties, ILs represent an ideal candidate to replace carbonate based electrolytes in LIBs.[83, 113-114, 130, 163] While ILs display wide electrochemical stability due to the strong electrostatic interactions between cations and anions at ambient temperatures, ILs suffer from comparatively low conductivities and high viscosities.[24, 164-165]

Previous experimentation with linear and cyclic carbonates demonstrates the positive impacts the incorporation of an electronegative moiety into the carbonate structure has on the observed physiochemical properties, such as conductivity, viscosity, and electrochemical stability.[166] For example, incorporation of a fluorine element into cyclic and linear carbonate-based solvents has dramatically increased the oxidation potential and decreased the melting point.[112, 167-169] Carbonate-based solvents with sulfone functional groups have a wider oxidation potential up to 5 V versus Li^+/Li.[170-173] Lastly, it is documented that lithium ions have a strong affinity for oxygen atoms. As such, most carbonate-based solvents already include at least one ether moiety, and further incorporation of more ether moieties displayed enhanced ion transport efficiancy.[166, 174]

We hypothesize that the incorporation of electronegative elements into the cationic structure of an IL will have beneficial effects on the viscosity and conductivity and will improve performance at ambient temperatures, resulting in an IL with the necessary physiochemical properties to serve as an electrolyte in a LIB with operating temperature between 25 ^{o}C to 100 ^{o}C.

4.2 Physiochemical Properties of Ionic Liquids with an Electronegative Moiety

4.2.1 Design Parameters of Ionic Liquid Electrolytes

Candidate IL electrolytes must possess specific physical and chemical properties to replace current electrolyte systems. Specifically, IL electrolytes must: 1) be thermally stable upwards of 300 ^{o}C; 2) display a wide liquid range of -10 ^{o}C – 200 ^{o}C; 3) be electrochemically stable between 0 – 5 volts; 4) have a conductivity of 3-10 mS/cm at 25 ^{o}C; 5) display a low viscosity, comparable to linear carbonate electrolytes; and 6) display SEI formation capabilities. We selected a tetraalkylphosphonium cationic structure as the base compound because of its low viscosity and established electrochemical stability.[12, 117, 124-126, 175-176] We synthesized phosphonium based ILs paired with an ether, fluoride, or sulfonyl moiety and measured the resulting ILs' thermal stability, conductivity and viscosity.

4.2.2 Thermal Behavior Fluoro-, Sulfonyl-, and Ether Based Ionic Liquids

Three series of ILs were generated featuring either an ether, a fluoride, or a sulfonyl moiety. Each series also included either an increasing number of moieties incorporated

into the cationic structure or an increase in the alkyl chain length extending from the cationic center (Fig. 4.1). During the synthesis of the IL, the cationic center was first paired with a halide anion (Cl^- or Br^-) before an anion exchange reaction was completed to replace the halide with a TFSI anion. The exchange was completed for two reasons; firstly the fluoride present in the TFSI anion is beneficial in the formation of a stable SEI during battery cycling.[19, 139, 177] Secondly, the much larger molecular size of the TFSI anion, which features a highly delocalized negative charge, typically generates ILs with lower melting points.

For each IL, the thermal behavior and stability was assessed via thermal gravimetric analysis (TGA) and differential scanning calorimetry (DSC) to identify the thermal degradation (T_d) and melting point (T_m) (Table 4.2). For a majority of the compounds, the $TFSI^-$ version of the IL displays a higher T_d, lower melting points and wider liquid range than their halide variant. The improved thermal stability of the $TFSI^-$ version of the ILs is due to the larger molecular size of the anion as well as the stronger bonds present in the TFSI anion itself. For example, comparing the melting points of P2F-I and P6F-TFSI, P2F-I has a sharp melting point at 51.56 ^oC while P6F-TFSI melts at 19.79 ^oC, near ambient temperatures. Moreover, it was observed that as the alkyl chain length extending from the phosphonium cationic center increases, the resultant IL has a lower melting point and subsequently a larger liquidus range; this is particularly true for the fluoride series.

In the fluoride series, changes in the cationic or anionic structure significantly affect the thermal properties of the IL, but in the sulfonyl series, the connection between

structure and thermal properties was not readily correlated. The sulfonyl based ILs are not liquids or solids, but glassy compounds that flow upon the addition of heat. After heating, the ILs slowly cool and solidify into a glassy solid again. DSC analysis for all of the sulfonyl compounds did not identify a crystallization (T_c) or melting (T_m) temperature, however a glass transition state (T_g) was identified. Moreover, while increasing the alkyl change length did not affect the liquid range as strongly in this series as in the fluoride series, the longer chains did hinder the packing properties of the compounds and decreased the T_g, resulting in a slower solidification and organization process for P6S-TFSI compared to P2S-TFSI. As such, P6S-TFSI takes significantly more time to solidify after heating than P2S-TFSI, and P2S-TFSI is a solid while P6S-TFSI is a tacky compound at ambient temperatures. As none of the sulfonyl ILs are liquids at room temperature, no further characterization work was completed.

For the ether series, instead of increasing the alkyl chain lengths extending from the phosphonium center, the number of methoxy groups present in one of the chains was increased from one to two. Previously, Tsunashima and Sugiya as well as our lab extensively studied the IL P1o1-TFSI and its improved conductivity and viscosity compared to other ILs lacking an ether moiety.[12, 88, 93, 133, 178] Researchers in our lab utilized P1o1-TFSI with 1.0 M LiTFSI in a Lithium Titanate (LTO) half-cell configuration at 24 ^oC and 90 ^oC; at 24 ^oC, the P1o1-TFSI equipped half-cell does not display a stable discharge capacity compared to a standard carbonate solvent, but at 90 ^oC, the half-cell has an increased discharge capacitance, (~175 mAh/g vs 160 mAh/g) compared to a standard carbonate solvent.[133] The ultimate goal with utilizing a RTIL

electrolyte is to develop a system that works as well as or better than current systems. P1o1-TFSI as an electrolyte works nearly as well as a carbonate solvent, but further work needs to be completed to improve its performance as an electrolyte at ambient temperatures.

To further improve the performance of the P1o1-TFSI, the viscosity of P1o1-TFSI needs to be decreased. From the fluoride and sulfonyl series, it was demonstrated that increasing the alkyl chain lengths extending from the cationic center decreases the melting point of the resultant IL, decreasing the viscosity of the system. Unfortunately, increasing the side chains extending from P1o1-TFSI would decrease the packing ability of the RTIL, as P1o1-TFSI is already a liquid with a low melting point. Instead, the number of ether moieties were increased and the length of only a single side chain was increased to accommodate the extra ether groups.

P2o1 features two ether groups in a single carbon chain but maintains the same structure as P1o1. For this series, again, both the halide and $TFSI^-$ variants of the ILs were synthesized. Comparing the four phosphonium compounds, P1o1-Br, P1o1-TFSI, P2o1-Br and P2o1-TFSI, all are liquids at ambient temperature except for P1o1-Br, which is a white solid. Increasing the chain length of P1o1-Br to P2o1-Br has an appreciable effect on the melting point as P2o1-Br melts 60 ^oC lower than P1o1-Br. But P2o1-Br is less thermally stable than both P1o1-TFSI and P2o1-TFSI with a T_d of 265 ^oC, while P1o1-TFSI and P2o1-TFSI are stable above 300 ^oC. P2o1-TFSI displays no T_m or T_c and remains a liquid at ambient temperatures, unlike P1o1-TFSI which is a solid below 20 ^oC. All the ether ILs generated do not solidify upon standing, unlike the sulfonyl based ILs.

4.2.3 Conductivity and Viscosity of Room Temperature Ionic Liquids

The conductivity and viscosity of the ILs which are liquids at ambient temperatures, herein called room temperature ionic liquids (RTILs), were measured. The conductivity and viscosity of the RTILs were measured as a function of temperature. As is common for RTILs, as the temperature increases, the conductivity increases and viscosity decreases. While P2o1-TFSI displays a larger liquid range than P1o1-TFSI, it is less conductive and more viscous than P1o1-TSFI. The replacement of two methylene groups with the ethers did not reduce the size of the molecular structure enough to counterbalance the longer alkyl chain length of P2o2-TFSI, increasing the viscosity of the RTIL. At room temperature, P1o1-TFSI has a conductivity of 3.1 mS/cm while P2o1-TFSI only has a conductivity of 2.3 mS/cm (Fig. 4.2a). P2o1-Br is less conductive than both P2o1-TFSI and P1o1-TFSI, while P6F-TFSI is less conductive than P2o1-Br.

The viscosity of the compounds follows the trend established while measuring conductivity. P1o1-TFSI and P2o1-TFSI have very similar viscosities, while P2o1-Br and P6F-TFSI are appreciably more viscous (Fig. 4.2b). Though P1o1-TFSI and P2o1-TFSI are approximately 10 times less viscous than P2o1-Br, they are still 100 times more viscous than a traditional carbonate based solvent.

As P2o1-TFSI and P1o1-TFSI display the best conductivity of the synthesized compounds, the electrochemical stability of the RTILs were assessed using a 3-electrode split cell systems Li/Li/Pt at 25 ^{o}C and at an elevated temperature, 60 or 100 ^{o}C) (Fig. 4.3). At both 25 ^{o}C and an elevated temperature, the RTILs are not stable from -1 to 5 V.

Plus while P2o1-TFSI electrochemical stability was measured at 60 ºC but P1o1-TFSi was measured at 100 ºC, P2o1-TFSI displays a significantly larger current response than P1o1-TFSI (Fig. 4.3b). This instability means the RTILs would only work as an electrolyte in a small operational window potential, limiting the power output of the EES device. There is some evidence that the instability of the RTILs is correlated to the incorporation of the ether groups, though in other experiments it was not to the extend observed here.[93, 179]

4.3 Summary and Future Work

Three series of ILs were generated, each featuring a unique electronegative moiety in one of the side chains of the phosphonium based cation. The thermal behavior and stability of each IL was measured and three trends were observed. First, the size of the anion and ability of the molecule to delocalize the negative charge has a large impact on the melting points of the ILs. The halide version of nearly all the ILs are solids with high melting points; after exchanging to the TFSI anion the melting point lowers enough to produce RTILs at ambient temperatures. Second, increasing the length of the alkyl chains extending from the cationic center had a similar effect as exchanging the anion; the longer the alkyl chains the less “packable” the ILs were, reducing the melting point and increasing the liquid range of the IL. Lastly, the ether moiety when incorporated had the greatest effect on the thermal properties and liquid range of the IL, increasing the conductivity by 2 mS/cm. Utilizing the three series of ILs we have identified simple chemical alterations that result in measurable changes in the physiochemical properties of

an IL; representing a facile method to design and synthesize RTILs with exact properties and behaviors.

4.4. Experimental Methods

All other reagents were purchased from Sigma Aldrich, or Acros and used without further purification. Lithium bis(trifluoromethanesulfonyl)imide (LiTFSI), 99 % (Sigma-Aldrich) was purchased at the highest purity and stored in a glovebox with moisture levels below 5 ppm. ^{1}H (500 MHz), ^{13}C (126 MHz) and ^{31}P (500 MHz) NMR spectra were recorded on Varian INOVA spectrometers. Electrospray mass spectra were obtained on an Agilent 1100 LC/MS Trap with ESI and APCI sources (LC/MS). Infrared data was collected on a Nicolet FT-IR with ATR.

4.4.1 Synthesis of the Ionic Liquids

Synthesis of the Ether Ionic Liquids:

Synthesis of P1o1-TFSI (triethyl-methoxymethyl-phosphonium bis(trifluoro-methanesulfonyl)imide: A pre-dried Schlenk flask was charged with 30 mL (30 mmol) of a 1.0 M triethyl-phosphine in Tetrahydrofuran (THF) solution and capped with a rubber stopper in a glovebox. Nitrogen was flowed through the Schlenk flask as the cap was replaced with a condenser sealed at the end with a nitrogen balloon. Then 3.28 mL (33 mmol) of 1-bromo-methyl-methoxyl was added along with 10 mL of dry THF and refluxed at 78 ^{o}C for 12 hours. A P1o1-Br, a solid, was obtained and dried at 80 ^{o}C for 12 hours. Equimolar amounts of P1o1-Br and LiTFSI were dissolved in 50 ml of

Dichloromethane (DCM) and 50 mL deionized (DI) water, respectively. The two phases were mixed and stirred at room temperature for 12 hours to yield P1o1-TFSI. Next, the product was washed three times with fresh DI water. To ensure the removal of the halide, three drops of 1 N silver nitrate ($AgNO_3$) were added to an aliquot of the DCM phrase; a solid precipitate indicated the presence of halide anions and the extraction steps were repeated. The product was dried under vacuum for 12 hours at 80 ^oC to give P1o1-TFSI in a 90 % yield. ^{1}H-NMR (CD_3OD): δ1.21-28 (m, 3H, P-CH_2-**CH_3**), 2.17-25 (m, 6H, P-**CH_2**-CH_3), 3.48 (s, 3H, P-CH_2-O-**CH_3**), 4.41-21 (d, 2H, P-**CH_2**-O-CH_3). ^{13}C-NMR: δ5.59 (3C, P-CH_2-**CH_3**), 10.41 (3C, P-**CH_2**-CH_3), 61.11 (1C, P-CH_2-O-**CH_3**), 78.61 (1C, P-**CH_2**-O-CH_3), 117.68, 120.23, 122.78, 125.33 (CF_3); LC/MS: Pos. 163.1 m/z, Neg. 279.1 m/z.

Synthesis of P2o1-TFSI (triethyl-methoxyethoxyethyl-phosphonium bis(trifluoro-methane-sulfonyl)imide: A pre-dried Schlenk flask was charged with 30 mL (24 mmol) of a 1.0 M triethyl-phosphine in Tetrahydrofuran (THF) solution and capped with a rubber stopper in a glovebox. Nitrogen was flowed through the Schlenk flask as the cap was replaced with a condenser, sealed at the end with a nitrogen balloon. Then 3.23 mL (24 mmol) of 1-bromo-methoxy-ethoxy-methyl was added along with 10 mL of dry THF and refluxed at 78 ^oC for 12 hours. A P2o1-Br, a viscous liquid, was obtained and dried at 80 ^oC for 12 hours. Equimolar amounts of P2o1-Br and LiTFSI were dissolved in 50 ml of Dichloromethane (DCM) and 50 mL deionized (DI) water, respectively. The two phases were mixed and stirred at room temperature for 12 hours to yield P1o1-TFSI.

Next, the product was washed three times with fresh DI water. To ensure the removal of the halide, three drops of 1 N silver nitrate ($AgNO_3$) were added to an aliquot of the DCM phrase; a solid precipitate indicated the presence of halide anions and the extraction steps were repeated. P2o1-TFSI was purified with a silica column and the product was dried under vacuum for 12 hours at 80 ^oC to give P2o1-TFSI with a yield of 59.9 %. ^{1}H-NMR ($(CD_3)OD$): δ1.3 (m, 9H, P-CH_2-**CH_3**), 2.4 (m, 6H, P-**CH_2**-CH_3), 2.6 (m, 2H, P-CH_2-**CH_2**-O- CH_2-CH_2-O-CH_3), 3.4 (s, 3H, P-CH_2-CH_2-O-CH_2-CH_2-O-**CH_3**), 3.6 (d of q, 4H, P-CH_2-CH_2-O-**CH_2-CH_2**-O-CH_3), 3.9 (d of t, 2H, P-**CH_2**-CH_2-O- CH_2-CH_2-O-CH_3. ^{13}C-NMR: δ6.00 (1C, P-CH_2-**CH_3**), 13.11 (1C, P-**CH_2**-CH_3), 20.0 (1C, P-CH_2-**CH_2**-O-CH_2-CH_2-O-CH_3), 59.22 (1C, P-CH_2-CH_2-O-CH_2-**CH_2**-O-CH_3), 64.93 (1C, P-CH_2-CH_2-O-**CH_2**-CH_2-O-CH_3), 71.41 (1C, P-CH_2-CH_2-O- CH_2-CH_2-O-**CH_3**), 72.84 (1C, P-**CH_2**-CH_2-O- CH_2-CH_2-O-CH_3)117.68, 120.23, 122.78, 125.33 (CF_3); LC/MS: Pos. 221.2 m/z, Neg. 280.2 m/z.

Synthesis of P2F-TSFI (triethyl-3,3,3-trifluoro-propyl-phosphonium bis(trifluoro-methanesulfonyl)imide): 2.7 mmol 3-Iodo-1,1,1-trifluoropropane was added dropwise to 2 mmol of a 1.0 M triethyl-phosphine in THF solution in a Schlenk flask inside the glovebox. The Schlenk flask was removed from the glovebox and capped with a sealed condenser with a nitrogen balloon. 5 mL of dry THF was added to the solution which was stirred for 12 hours. A white solid product was then obtained and dried under vacuum at 80 ^oC prior to the anion exchange reaction. Anion exchange with LiTFSI was completed following the same procedure as P1o1-TFS. The solid white product was purified using a

silica column to obtain P2F-TFSI in 45 % yield. ^{1}H-NMR (CD_3OD): δ0.92-0.98 (m, 9H, P-CH_2-**CH_3**), 1.27-1.32 (m, 6H, P-CH_2-CH_3), 2.84-2.90 (d of m, 4H, P-**CH_2-CH_2**-CF_3). ^{13}C-NMR: δ6.00 (3C, P-CH_2-**CH_3**), 11.77 (4C, P-**CH_2**-CH_3), 70.20 (2C, P-**CH_2-CH_2**-CF_3), 71.31 (1C, P-CH_2-CH_2-**CF_3**) 117.68, 120.23, 122.78, 125.33 (CF_3); LC/MS: Pos. 215.1m/z, Neg. 279.1 m/z.

P4F-TFSI, tributyl-3,3,3-trifluoro-propyl-phosphonium bis(trifluoro-methane-sulfonyl)imide, and P6F-TFSI, trihexyl-3,3,3-trifluoro-propyl-phosphonium bis(trifluoro-methane-sulfonyl)imide, were synthesized following the same procedure as P2-TFSI except tributyl-phosphine and trihexyl-phosphine were used instead of triethyl-phosphine, respectively.

Synthesis of P4F-TFSI, 95 % yield: ^{1}H-NMR (CD_3OD): δ0.92-0.98 (m, 9H, P-CH_2-CH_2-CH_2-**CH_3**), 1.27-1.32 (m, 6H, P- CH_2-CH_2-**CH_2**-CH_3), 1.48-1.57(m, 6H, P-CH_2-**CH_2**-CH_2-CH_3), 2.69-2.74 (m, 6H, P-**CH_2**-CH_2-CH_2-CH_3), 2.84-2.90 (d of m, 4H, P-**CH_2-CH_2**-CF_3). ^{13}C-NMR: δ9.80 (3C, P-CH_2-CH_2-CH_2-**CH_3**), 15.77 (3C, P-CH_2-CH_2-**CH_2**-CH_3), 20.80 (3C, P-CH_2-**CH_2**-CH_2-CH_3), 62.72 (3C, P-**CH_2**-CH_2-CH_2-CH_3), 70.20 (2C, P-**CH_2-CH_2**-CF_3), 71.31 (1C, P-CH_2-CH_2-**CF_3**) 117.68, 120.23, 122.78, 125.33 (CF_3); LC/MS: Pos. 301.2 m/z, Neg. 279.1 m/z.

Synthesis of P6F-TFSI, 87 % yield: ^{1}H-NMR (CD_3OD): δ0.85-0.88 (m, 9H, P-CH_2-CH_2-CH_2-CH_2-**CH_3**), 1.27-1.32 (m, 12H, P-CH_2-CH_2-CH_2-**CH_2-CH_2**-CH_3), 1.48-1.57(m, 12H, P-CH_2-**CH_2-CH_2**-CH_2-CH_2-CH_3), 2.5-2.63 (m, 6H, P-**CH_2**-CH_2-CH_2-CH_2-CH_2-CH_3), 2.68-2.71 (d of m, 4H, P-**CH_2-CH_2**-CF_3). ^{13}C-NMR: δ6.00 (3C, P-CH_2-CH_2-

CH_2-CH_2-CH_2-**CH_3**), 12.77 (3C, P-CH_2-CH_2-CH_2-**CH_2-CH_2**-CH_3), 19.80 (3C, P-CH_2-CH_2-**CH_2**-CH_2-CH_2-CH_3), 58.72 (3C, P-CH_2-**CH_2**-CH_2-CH_2-CH_2-CH_3), 63.93 (3C, P-**CH_2**-CH_2-CH_2-CH_2-CH_2-CH_3), 70.20 (2C, P-**CH_2-CH_2**-CF_3), 71.31 (1C, P-CH_2-CH_2-**CF_3**) 117.68, 120.23, 122.78, 125.33 (CF_3); LC/MS: Pos. 383.3 m/z, Neg. 281.1 m/z.

Synthesis of Sulfonyl Ionic Liquids

Oxidation of 2-chloro-ethyl-methyl-sulfide to 2-chloro-ethyl-methyl-sulfone: Add 32.1 mmol (110.61 g/mol) of 2-chloro-ethyl-methyl-sulfide to 35.5 mL of methanol, simultaneously add 64.2 mmol (307.38 g/mol) potassium peroxomonosulfate to 18 mL of water, and combine the solutions and stir for 24 hours at room temperature. Next, concentrate the mixture on the roto-vap, a large quantity of white solid side products will be present. Add the mixture, not the white residue, to a separatory funnel and dissolve in dichloromethane (DCM). Extract the reaction with a solution of sodium carbonate and then wash with a brine solution. Dry the organic layer with magnesium sulfate and roto-vap the solvent to obtain the white solid, 2-chloro-ethyl-methyl-sulfone, in 25 % yield. ^{1}H-NMR ($(CD_3)_2$ CO) : δ1.50 (t, 3H, Cl-CH_2-CH_2-SO_2-CH_2-**CH_3**), 3.32 (q, 2H, Cl-CH_2-CH_2-SO_2-**CH_2**-CH_3), 3.70 (t, 2H, Cl-CH_2-**CH_2**-SO_2-CH_2-CH_3), 4.07 (t, 2H, Cl-**CH_2**-CH_2-SO_2-CH_2-CH_3). FT-IR: ν1118.96 and 1285.33 (SO_2).

Synthesis of P2S-TFSI, triethyl-ethyl-methyl-sulfonyl-phosphonium bis(trifluoro-methane-sulfonyl)imide: 8.1 mmol 2-chloro-ethyl-methyl-sulfone was dissolved in THF and added dropwise to 8 mmol of a 1.0 M triethyl-phosphine in THF solution in a

Schlenk flask inside the glovebox. The Schlenk flask was removed from the glovebox and capped with a sealed condenser with a nitrogen balloon. 5 mL of dry THF was added to the solution which was stirred for 12 hours. The white viscous liquid product was then obtained and dried under vacuum at 80 ^{o}C prior to the anion exchange reaction. Anion exchange with LiTFSI was completed following the same procedure as P1o1-TFSI. The solid viscous liquid/solid product was purified using a silica column to obtain P2S-TFSI in yield 71 %. ^{1}H-NMR ($(CD_3)_2$ CO): δ1.37 (m, 9H, P-CH_2-**CH_3**), 2.59 (m, 9H, P-**CH_2**-CH_3), 2.59 (m, 2H, P-CH_2-**CH_2**-SO_2-CH_3), 3.12 (s, 2H, P-CH_2-CH_2-SO_2-**CH_3**), 3.61 (m, 2H, P-**CH_2**-CH_2-SO_2-CH_3). ^{13}C-NMR: δ4.44 (1C, P-CH_2-**CH_3**), 11.53 (1C, P-**CH_2**-CH_3), 39.71 (1C, P-CH_2-**CH_2**-SO_2-CH_3), 45.72 (1C, P-CH_2-CH_2-SO_2-**CH_3**), 54.07 (1C, P-**CH_2**-CH_2-SO_2-CH_3), 117.68, 120.23, 122.78, 125.33 (CF_3); LC/MS: Pos. 225.1m/z, Neg. 279.1 m/z.

P4S-TFSI, tributyl-ethyl-methyl-sulfonyl-phosphonium bis(trifluoro-methane-sulfonyl)imide, and P6S-TFSI, trihexyl-ethyl-methyl-sulfonyl-phosphonium bis(trifluoro-methane-sulfonyl)imide, were synthesized following the same procedures as P2S-TFSI except tributyl-phosphine and trihexyl-phosphine were used instead of triethyl-phosphine, respectively.

Synthesis of P4S-TFSI, yield 63 %. ^{1}H-NMR ($(CD_3)_2$ CO): δ0.97 (m, 9H, P-CH_2-CH_2-CH_2-CH_2-**CH_3**), 1.50 (m, 6H, P-CH_2-CH_2-CH_2-**CH_2**-CH_3), 1.75 (m, 6H, P-CH_2-CH_2-**CH_2**-CH_2-CH_3), 2.53 (m, 6H, P-CH_2-CH_2-CH_2-CH_2-**CH_3**), 2.96 (m, 2H, P-CH_2-**CH_2**-SO_2-CH_3), 3.07 (s, 2H, P-CH_2-CH_2-SO_2-**CH_3**), 3.66 (m, 2H, P-**CH_2**-CH_2-SO_2-CH_3). ^{13}C-

NMR: δ12.35 (1C, P-CH_2-CH_2-CH_2-CH_2-**CH_3**), 17.52 (1C, P-CH_2-CH_2-CH_2-**CH_2**-CH_3), 18.07 (1C, P-CH_2-**CH_2**-CH_2-CH_2-CH_3), 22.69 (1C, P-**CH_2**-CH_2-CH_2-CH_2-CH3), 23.55 (1C, P-CH_2-**CH_2**-SO_2-CH_3), 45.72 (1C, P-CH_2-CH_2-SO_2-**CH_3**), 54.07 (1C, P-**CH_2**-CH_2-SO_2-CH_3), 117.68, 120.23, 122.78, 125.33 (CF_3); LC/MS: Pos. 309.2 m/z, Neg. 280.1m/z.

Synthesis of P6S-TFSI, 64 % yield. ^{1}H-NMR ($(CD_3)_2$ CO): δ0.86 (m, 9H, P-CH_2-CH_2-CH_2-CH_2-CH_2-CH_2-**CH_3**), 1.35 (m, 12H, P-CH_2-CH_2-CH_2-CH_2-**CH_2-CH_2**-CH_3), 1.50 (m, 6H, P-CH_2-CH_2-CH_2-**CH_2**-CH_2-CH_2-**CH_3**), 1.74 (m, 6H, P-CH_2-**CH_2**-CH_2-CH_2-CH_2-CH_2-CH_3), 2.53 (m, 6H, P-**CH_2**-CH_2-CH_2-CH_2-CH_2-CH_2-CH_3), 2.95 (m, 2H, P-CH_2-**CH_2**-SO_2-CH_3), 3.12 (s, 2H, P-CH_2-CH_2-SO_2-**CH_3**), 3.66 (m, 2H, P-**CH_2**-CH_2-SO_2-CH_3). ^{13}C-NMR: δ6.00 (3C, P-CH_2-CH_2-CH_2-CH_2-CH_2-**CH_3**), 12.77 (3C, P-CH_2-CH_2-CH_2-**CH_2-CH_2**-CH_3), 19.80 (3C, P-CH_2-CH_2-**CH_2**-CH_2-CH_2-CH_3), 58.72 (3C, P-CH_2-**CH_2-**CH_2-CH_2-CH_2-CH_3), 63.93 (3C, P-**CH_2**-CH_2-CH_2-CH_2-CH_2-CH_3), 23.55 (1C, P-CH_2-**CH_2**-SO_2-CH_3), 45.72 (1C, P-CH_2-CH_2-SO_2-**CH_3**), 54.07 (1C, P-**CH_2**-CH_2-SO_2-CH_3), 117.68, 120.23, 122.78, 125.33 (CF_3); LC/MS: Pos. 393.3 m/z, Neg. 280.1 m/z.

4.4.2 Thermal Analysis

Before each of the following tests, the samples were dried at 80 °C while under vacuum for at least 6 hours. Thermal Gravimetric Analysis (TGA) experiments were completed with TGA Q50 and samples were heated from 20 to 500 °C at a rate of 10 °C

min^{-1}. Thermal decomposition point was defined as the temperature where 10 % weight loss of the original sample weight was recorded.

Thermal transitions were measured using a TA instruments Q100 Differential Scanning Calorimeter from -70 ^oC to 250 C at a heating rate of 20 $^oC\ min^{-1}$ and cooling of 5 $^oC\ min^{-1}$ for three iterations. All samples weighed between 10 to 20 mg. Viscosity was measured on TA Instruments DHR-2 Rheometer. Generally, a 25 mm aluminum plate geometry was used with the gap set to 1000 um. Prior to testing, a pre-shear at a rate of 100 Hz for 10 s followed by a five min equilibrium was performed to eliminate physical memory of the sample. An oscillatory strain sweep was completed between 0.1 % and 12 % strain at 1 Hz to find the Linear Viscoelastic Region (LVR). Next, a frequency sweep from 0.1 to 12.5 Hz was completed at a strain % within the LVR. The dynamic viscosity was recorded at a specific frequency and strain %.

An oscillatory temperature sweep was conducted from 10 to 95 ^oC with increment of 10 ^oC and 1 min equilibrium at each temperature with strain and frequency set to 10% and 1 Hz, respectively. Samples were dried at 80 ^oC overnight while under a vacuum prior to testing.

Conductivity measurements were performed with a Conductivity Meter (K912, Consort, +/- 0.5% fs of range for conductivity and +/- 0.3 ^oC) equipped with a 4-electrode cell to prevent polarization error and fouling of the electrode. 4- electrode probe was calibrated with .01, 0.1 and 1 M KCl Standard Solutions. Testing was completed inside an Argon Glovebox (H_2O <1 ppm, O_2 <0.6 ppm) and a heating block was used to

control the temperature; samples were equilibrated for 30 min at each temperature. Samples were dried at 80 ºC while under vacuum overnight before testing.

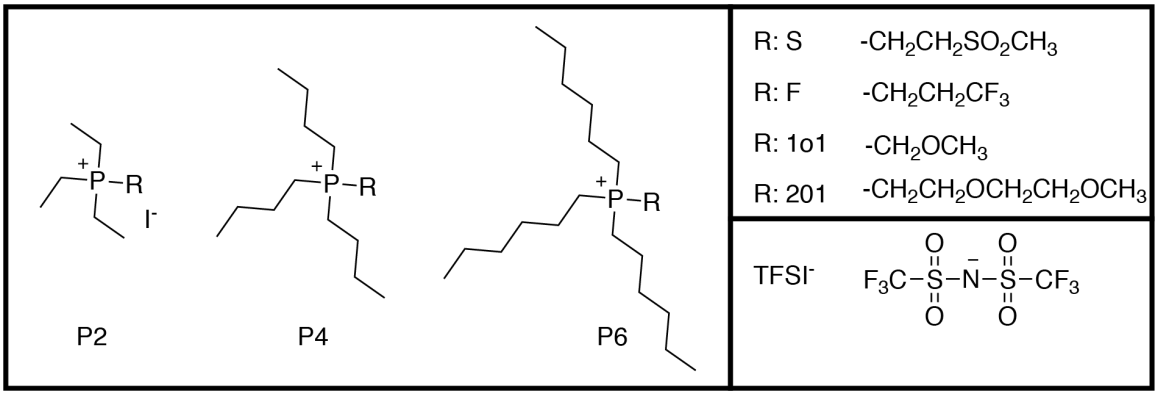

Fig. 4.1 The various cationic structures measured in this reported and manipulated with various R groups.

Table 4.1 Thermal Properties of Series of Electronegative Ionic Liquids.

Compound	T_g (°C)	T_m (°C)	T_d (°C)	Physical Description
P2F-I	---	N/A	N/A	Solid
P2F-TFSI	---	80.84	396	Solid
P4F-I	---	120.67	335	Solid
P4F-TFSI	---	102.68	359	Solid
P6F-I	---	51.56	297	Solid
P6F-TFSI	---	19.79	379	Liquid
P2S-Cl	2.57	---	248	Solid
P2S-TFSI	-40.02	---	365	Solid
P4S-Cl	-17.51	---	228.83	Solid
P4S-TFSI	-39.02	---	348.25	Solid
P6S-Cl	-24.22	---	227.41	Solid
P6S-TFSI	-49.63	---	354.99	Solid
P1o1-Br	---	86.79	239.20	Solid
P1o1-TFSI	---	19.10	362	Liquid
P2o1-Br	---	25.27	265	Liquid
P2o1-TFSI	---	N/A	385	Liquid
(---) indicates no value was measured				

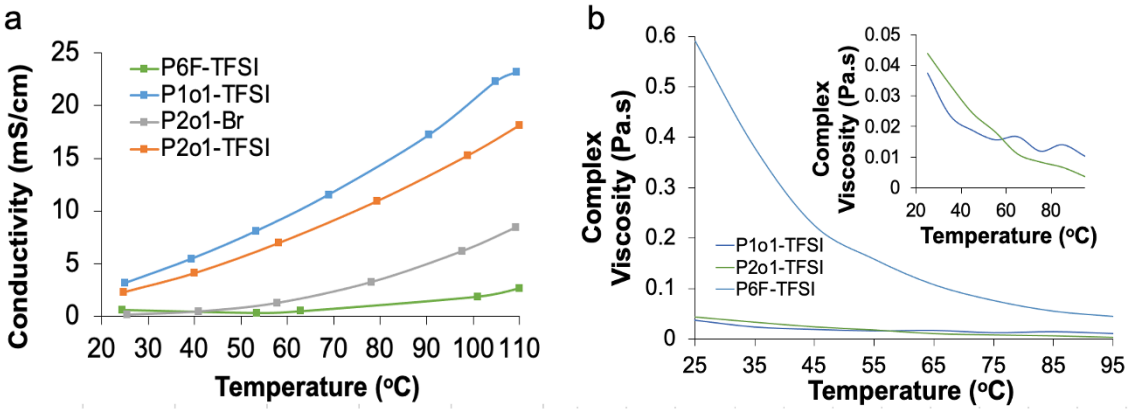

Fig. 4.2 (a) Conductivity of the RTILs synthesized in this study. (b) Viscosity of the RTILs with the TFSI anion. The inset shows a closer view of P1o1-TFSI and P2o1-TFSI.

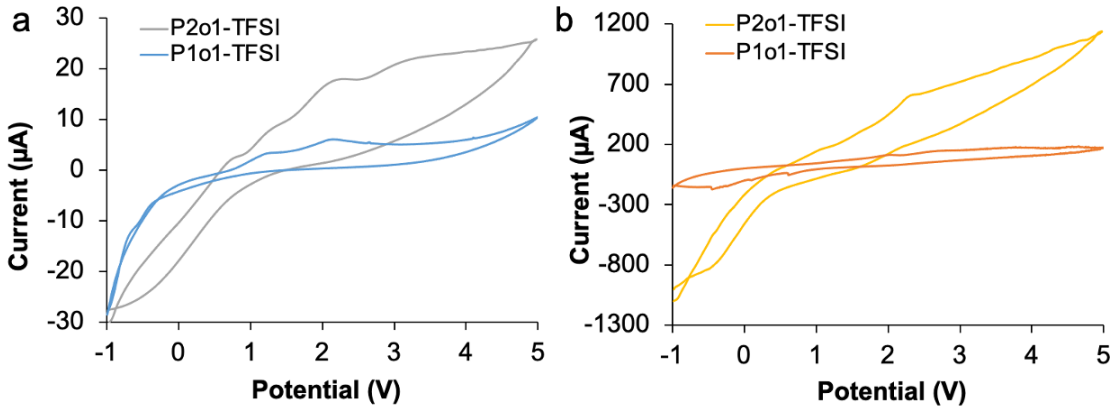

Fig. 4.3 (a) Cyclic voltammograms of P2o1-TFSI and P1o1-TFSI at 25 °C. (b) Cyclic voltammograms of P2o1-TFSI at 60 °C and P1o1-TFSI at 100 °C.

Chapter 5: Lithium Free Supercapacitors: Room Temperature Ionic Liquid Electrolytes for High Temperature Operation of Electrical Energy Storage Devices

5.1 Introduction

5.1.1 Humanitarian Concerns of Mining Lithium

Currently, the demand for electric energy storage (EES) devices that offer clean and renewable energy, such as lithium ion batteries and supercapacitors, necessitate the use of lithium salts in the electrolyte solution. The standard electrolyte solutions are a mixture of carbonate solvents and lithium salts; these solvents have good conductive properties, as well as low viscosity and facilitate the mobility of lithium ions during cycling of the EES device.[75, 82] While organic carbonate solvents mixed with various lithium salts affords EES devices with good energy and power density, there are two major limitations. First and foremost, the mining of lithium deposits which are generally found in South America produce numerous environmental and humanitarian concerns.[180-183] Secondly, EES devices are limited in operation to moderate temperatures between 0 and 50 ^{o}C due to volatile and flammable organic solvents utilized in these systems, limiting the operational temperature and raising severe safety concerns.[114, 164] The limited operational temperatures of the devices restricts their application in demanding fields such as electric vehicles.

To address both the humanitarian concerns of mining lithium and the limitations of the carbonate solvents, a new electrolyte motif must be designed that does not require the shuttling of lithium ions to generate energy. Room temperature ionic liquids (RTILs),

molten salts composed of a cationic and anionic components, represent ideal candidates to replace carbonate solvent mixture electrolytes; RTILs are inherently conductive as well as thermally and electrochemically stable. Plus, as RTILs are composed of two components the design of a RTIL with specific physiochemical is simply completed by exchanging the cationic and anionic components. The facile manipulation of the physicochemical properties of the RTIL, coupled with the inherent conductivity and thermal stability make RTILs an ideal candidate to replace standard organic carbonate/lithium salt electrolyte mixtures.

To generate a RTIL electrolyte which satisfies all the requirements required to replace standard electrolyte solvents at high temperatures and without the need for lithium salt, we have synthesized and characterized two RTILs based on the dicyanamide (DCA) anion; triethyl-propyl-phosphonium dicyanamide (P111-DCA) and 1-allyl-3-butyl-imidazolium dicyanamide (AC_4Im-DCA) (Fig. 5.1). The thermal stability, conductivity, viscosity, and electrochemical stability of the RTILs were measured as well as the performance of the RTIL electrolytes in activated carbon based supercapacitors at 60 ^oC.

5.2 Physiochemical Properties of P111-DCA and AC_4Im-DCA

Before performing supercapacitor experiments, the thermal stability, viscosity, conductivity and electrochemical stability of P111-DCA and AC_4Im-DCA were measured. Thermal gravimetric analysis (TGA) revealed decomposition temperatures of 358.75 and 229.82 ^oC for P111-DCA and AC_4Im-DCA, respectively. The phosphonium cation displays a hundred degree higher stability than the imidazolium cation, though

both RTILs are stable well above 100 ºC. The difference in thermal stability between the two RTILs is not explained by differences in molecular weight as both weigh approximately 231 g/mol. Differential scanning calorimetry (DSC) analysis shows no T_m or T_c for AC_4Im-DCA indicating the composition is a liquid over a wide temperature range, unlike P111-DCA which has a T_m and T_c at 4.35 and -32.09 ºC, respectively.

Next, the viscosity and conductivity of the RTILs were measured as a function of temperature from ≈ 25 to 100 ºC. The conductivity and viscosity are directly correlated to the temperature. As the temperature is increased, the viscosity values for P111-DCA and AC_4Im-DCA decrease (Fig. 5.2). For instance, at 25 ºC P111-DCA and AC_4Im-DCA possess viscosities of 0.046 and 0.054 Pa.s, respectively. At higher temperatures, the difference between the RTILs remain with P111-DCA and AC_4Im-DCA displaying viscosities of 0.020 and 0.031 Pa.s, respectively. The weak dipole moment in the allyl group present on the AC_4Im cation increases the intermolecular forces present in a solution of AC_4Im-DCA compared to P111-DCA, resulting in the slightly increased viscous nature of AC_4Im-DCA. The conductivity of AC_4Im-DCA and P111-DCA increase with increasing temperature as well: at 25 ºC, AC_4Im-DCA and P111-DCA exhibit conductivities of 6.81 and 7.13 mS/cm, respectively. At approximately 105 ºC, the conductivity difference between AC4Im-DCA and P111-DCA are more pronounced with the values of 33.3 and 43.4 mS/cm, respectively. For comparison, a conventional electrolyte, propylene carbonate (PC) with 1.0 M LiTFSI, displays a conductivity and viscosity values of 4.8 mS/cm, 0.006 Pa.s, and 10.8 mS/cm, and 0.003 Pa.s at 25 and 80 ºC, respectively.[103]

The electrochemical stability of P111-DCA and AC_4Im-DCA were evaluated using a 3-electrode split cell at 25 ºC and 60 ºC. At both temperatures, P111-DCA and AC_4Im-DCA display wide electrochemical stability windows (Fig. 5.3). At 25 and 60 ºC, both P111-DCA and AC_4Im-DCA display no redox reactions, and even at 5 V no more than 50 µA is measured at 60 ºC; indicating a wide electrochemical stability window for both RTILs. For a more detailed analysis of the electrochemical stability of both P111-DCA and AC_4Im-DCA, please see chapter 3.

5.3 Supercapacitors with RTIL electrolytes

5.3.1 Activated Carbon Supercapacitors

Given the wide electrochemical stability window and high conductivity of P111-DCA and AC_4Im-DCA, we designed activated carbon based supercapacitors which utilized P111-DCA and AC_4Im-DCA electrolytes with no added lithium salt. In these coin cells, the cations and anions of the RTIL will generate the electric double layer.[143, 184-185] In order to take advantage of the improved conductivity and viscosity of the RTILs at elevated temperatures, all experiments were completed at 60 ºC. The supercapacitors were equipped with activated carbon electrodes and either neat P111-DCA or AC_4Im-DCA.

The discharge capacitance for each coin cell was calculated using the following equations:

$$C_s = 2I_{constant}/[m(dV/dt)], \qquad \text{Equation 5.1}$$

where I is the constant current applied in A, dV/dt is the slope of discharge curve, and m

is the mass of each electrode in g. Rapid decaying of discharge capacitance for AC_4Im-DCA from cycle 1 to cycle 1000 is observed from 68 F/g to 0 F/g (Fig. 5.4). Within the first 100 cycles 84 % of the discharge capacitance is lost. The supercapacitors equipped with P111-DCA display stable but low discharge capacitance from cycle 1 to 2000. After 2000 cycles, 74 % of the discharge capacitance is lost, with cycles 1 and 2000 exhibiting a discharge capacitance of 5.1 F/g and 1.2 F/g, respectively. At 60 ^oC both P111-DCA and AC_4Im-DCA have relatively high conductivities and moderate viscosities of 19.51 mS/cm and 0.023 Pa.s and 15.05 mS/cm and 0.037 Pa.s, respectively. While the viscosity of each RTIL is relatively high compared to a standard carbonate solvent electrolyte, which will increase the internal resistance of the coin cell, given the high conductivities of both RTILs, the improved conductive properties should counterbalance the viscosity. Plus, AC_4Im-DCA is not significantly more viscous than P111-DCA, in fact, both are more viscous than a traditional carbonate solvent than they are different from each other. The substantial difference in decaying rates between the two RTIL supercapacitors is not explained by the viscosity difference between the two.

5.3.2 Effects of Anionic Component on Cyclability of Supercapacitors

Research into the novel DCA anion and the effects of anion choice has on the cyclability of a lithium ion battery and supercapacitor is necessary to identify why both coin cells display rapid loss of discharge capacitance. Previous studies have demonstrated that the solid electrolyte interface (SEI), which forms during cycling of the device on the electrodes surface, greatly effects the cyclability of the cell; to form a strong but

permeable SEI the inclusion of a fluoride containing anion or salt is integral.[138, 163, 169] Moreover, other studies that have utilized the DCA based anion observed a passivation of the electrode surface through degradation and dimerization of the DCA anion, especially at elevated temperature.[137, 139] To determine if the DCA anions instability and the lack of the fluoride present in P111-DCA and AC_4Im-DCA are the reasons for the rapid failure of the coin cells at 60 ºC, new activated carbon electrodes were fabricated that featured the inclusion of 30 wt% N-methyl-N-methoxymethyl piperidinium bis(trifluoromethanesulfonyl)imide (PP1o1-TFSI). Previously, a PP1o1-TFSI equipped activated carbon supercapacitor with 1.0 M LiTFSI salt cycled at 100 ºC for over 10,000 cycles with a discharge capacitance of 28 F/g.[115]

5.3.3 PP1o1-TFSI Incorporated Supercapacitors

PP1o1-TFSI was included in the activated carbon (AC) mixture when fabricating the electrode and not included into the RTIL bulk electrolyte for two reasons. First, to ensure PP1o1-TFSI was close to the electrode and would not have to compete with the bulk cation and anions to reach the electrode surface. Second, to maintain the electrochemical stability of P111-DCA and AC_4Im-DCA as PP1o1-TFSI is not electrochemically stable (Fig. 5.5).

The supercapacitors outfitted with the infused electrodes had different effects on the cyclability and discharge capacitance for P111-DCA and AC_4Im-DCA. For AC_4Im-DCA, no improvement is observed; the coin cell still displays a rapid loss of capacitance after a high initial capacitance within 100 cycles (Fig. 5.6). However, the incorporation of

PP1o1-TFSI into the electrode surface displays a large effect on the discharge capacitance and cyclability for the P111-DCA equipped supercapacitors, enabling cycling for over 10,000 cycles with a final discharge capacitance of 10.62 F/g. While the initial discharge capacitance for the P111-DCA equipped supercapacitor displays a significant improvement of initial capacitance from 5.1 to 31 F/g, after 10,000 cycles P111-DCA only retains 30 % of its initial discharge capacitance.

5.2.4 Cyclic Voltammetry of RTIL Equipped Supercapacitors

To elucidate the cause of the rapid failure of the AC_4Im-DCA and P111-DCA coin cells, cyclic voltammetry experiments were completed; CV curves of the supercapacitors at scan rates of 0.005 V/s, 0.05 V/s, and 0.5 V/s from 0 to 3 V are shown in Figure 5.7a-b. As there is no lithium salt present and both P111-DCA and AC_4Im-DCA are electrochemically stable from -1 to 5 V (Li/Li^+), it was theorized that no pseudocapacitance would be observed in the coin cells. However, at all scan speeds neither the AC_4Im-DCA nor P111-DCA exhibit ideal capacitive behavior, with the CV curves displaying deviation from a simple rectangular shape (5.7a-b). Moreover, after cycling at each scan rate for ten cycles and then rescanning the samples at 0.005 V/s for ten cycles, reduced currents are measured for both P111-DCA and AC_4Im-DCA; indicating a reduction of available species to react at the electrode surface and a decrease in the number of free cations and anions available to form an electric double layer (Fig. 5.8a-b). In particular, AC_4Im-DCA displays non-repeatability, with the rescan at 0.005 V/s measuring nearly 1000 μA less than during the first scan. The decrease in the current

after repeating CV scans for AC_4Im-DCA indicates degradation of the RTIL.

5.2.5 Electrical Impedance Spectroscopy Experiments of Supercapacitors

The deviation from ideal capacitive behavior that both P111-DCA and AC_4Im-DCA, display and the mass reduction in current measured for AC_4Im-DCA indicates the presence of redox reactions. The presence of redox reactions in the supercapacitors, however, does not indicate that the cells generate capacitance through the reactions. To determine if the supercapacitors solely store charge via the electric double layer or if pseudocapacitance is present as well, electrical impedance spectroscopy experiments (EIS) were completed at 60 ^oC with a constant potential of 0.8 V and Nyquist plots were obtained (Fig. 5.9a). The Nyquist plots are linear from low to high frequencies for both P111-DCA and AC_4Im-DCA. Zooming into the high frequency region for both RTILs a linear line is present; indicating a diffusion mediated process even at high frequency (Fig. 5.9b). The linearity of both Nyquist plots at low and high frequencies confirms the capacitive charge behavior of the RTILs electrolyte. Thus, the formation of an EDL is the main mechanism for energy generation for the supercapacitors containing both RTILs.

5.2.6 Electrochemical Stability of RTILs on Carbon Electrodes

As the EIS experiments show a lack of pseudocapacitance aiding in the capacitance of the supercapacitors, the decaying discharge capacitance observed when cycling the coin cells must be due to the degradation of the RTILs themselves. Utilizing a three electrode system (Li/Li/Pt) both RTILs electrolytes were found to be stable from -1 to 5 V,

however, on the carbon/carbon electrodes they are not stable to the same voltage. The variable electrochemical stability on different surfaces is an inherent limitation for RTILs, as designing an EES device means measuring the electrochemical stability of the RTIL on various systems and at various voltages and scan rates to uncover the most accurate representation of the potential window.[186-187] On the carbon electrodes, P111-DCA and AC_4Im-DCA display differing electrochemistry, from each other and from the Li/Li/Pt system.[188]

P111-DCA displays a more stable electrochemical performance in the AC supercapacitor than AC_4Im-DCA because the phosphonium cation is more resistant to reduction compared to the imidazolium cation. The phosphonium is more resistant to reduction due to the hydrocarbon chains on the phosphonium cation increasing the energy needed to reduce the phosphonium cation.[179, 189] While the alkyl chains present in imidazolium RTILs have little effect on the electrochemical stability.[141] Moreover, the proposed reduction mechanism for a phosphonium cation is more easily reversed than the imidazolium based cations, as the radical of imidazolium cations tend to immediately dimerize.[190] This reversibility of the phosphonium cation means that the P111-DCA RTIL will remain viable to form the electric double layer, while the AC_4Im-DCA RTIL will degrade and lose capacitance. Thus, the imidazolium cation is not as electrochemically stable as the phosphonium cation.[191] Lastly, the DCA anion has shown to be less electrochemically stable than fluorinated anions on the carbon electrode.[131, 179] The DCA anion has also shown to dimerization at elevated temperatures and voltages depending on the cation pair.[192] As such, the pairing of the less electrochemically stable

AC_4Im cation with the DCA anion results in a RTIL which is electrochemically unstable, while the P111 cation paired with the DCA anion results in a more stable RTIL which is able to cycle in a carbon supercapacitor.

5.3 Conclusion

Two RTILs were prepared and their physiochemical properties evaluated. Both AC_4Im-DCA and P111-DCA are thermally stable above 200 ^oC and electrochemically stable from -1 to 5 V at 25 and 60 ^oC. Through cycling of activated carbon supercapacitors with both RTIL electrolytes it was found that the DCA anion passivates the electrode surface, limiting the cyclability of the supercapacitors. The inclusion of a piperidinium TFSI based RTIL electrolyte (PP1o1-TFSI) in the electrode surface increased the cyclability of the P111-DCA electrolyte to over 10,000 cycles with a final discharge capacitance of 10 F/g. EIS experiments confirmed the main mechanism of charge for AC_4Im-DCA and P111-DCA electrolytes is through the formation of an electric double layer, however AC_4Im-DCA displays an electrochemical instability to the activated carbon electrodes. The variable electrochemical stability that P111-DCA, AC_4Im-DCA and PP1o1-TFSI in a Li/Li/Pt 3-electrode system versus an activated carbon coin cell is still not fully understood. To improve the cyclability of the salt free RTIL supercapacitors further investigations into the variable electrochemical stability of the RTIL on various electrode surfaces need to be completed to improve cyclability and discharge capacitance of the promising salt free RTIL electrolytes.

5.4 Experimental

5.4.1 Synthesis of RTILs

For detailed directions on the synthesis of P111-DCA and AC_4Im-DCA, please see 3.5.1.

5.4.2 Characterization of RTIL

For detailed instructions on the characterization of the thermal properties, conductivity, viscosity and electrochemical stability of P111-DCA and AC_4Im-DCA, please see chapter 3.5.2

.

5.4.3 Fabrication and Characterization of Supercapacitors

For detailed instructions on the fabrication of activated carbon electrodes, please see chapter 2.6.3.

For the fabrication of the PP1o1-TFSI infused electrodes the ratio of materials was changed to 30 wt% PP1o1-TFSI, 55 wt% activated carbon, 11 wt% acetylene black, and 7 wt% poly(vinylidene fluoride) binder in N-methyl-pyrrolidinone solvent were ground together in a mortar.

5.4.4 Charge-Discharge, Cyclic Voltammetry and EIS of Supercapacitor Coin Cells

Cyclic voltammetry (CV) and charge-discharge (CD) and electrochemical impedance spectroscopy (EIS) measurements were performed using a Princeton Applied Research VersaStat battery tester. CV and CD tests were conducted over a voltage range of 0 to 3.0

V at scan rate of 0.005 V/s, 0.05 V/s, 0.5 V/s, and 0.005 V/s (again), for ten cycles each and at a current densities of 1 A/g at 60 °C. EIS measurements were conducted over a frequency range of 10 kHz to 10 mHz under a bias potential of 0.8 V using a 5 mV rms sinusoidal modulation. All calculations were based on the total weight of active materials.

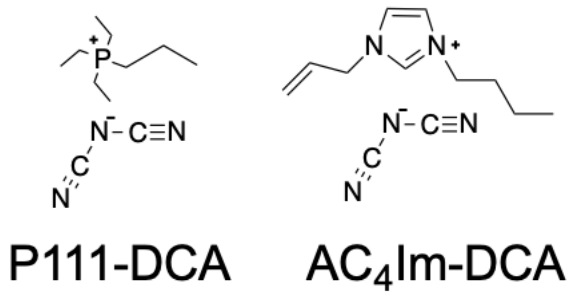

Fig. 5.1 Structure of P111-DCA (triethyl-propyl-phosphonium dicyanamide) and AC_4Im-DCA (1-allyl-3-butyl-imidazolium dicyanamide).

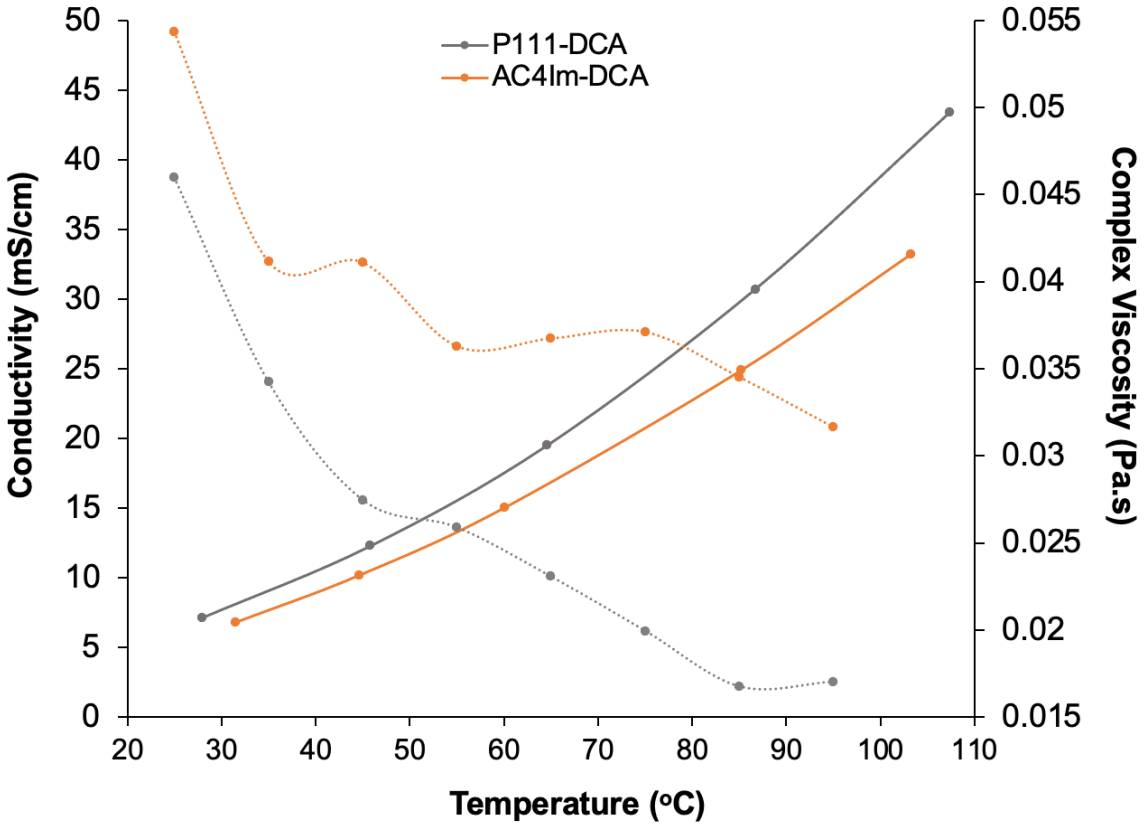

Fig. 5.2 Conductivity and Viscosity data of the neat RTILs P111-DCA and AC4Im-DCA. Dotted lines represent viscosity data.

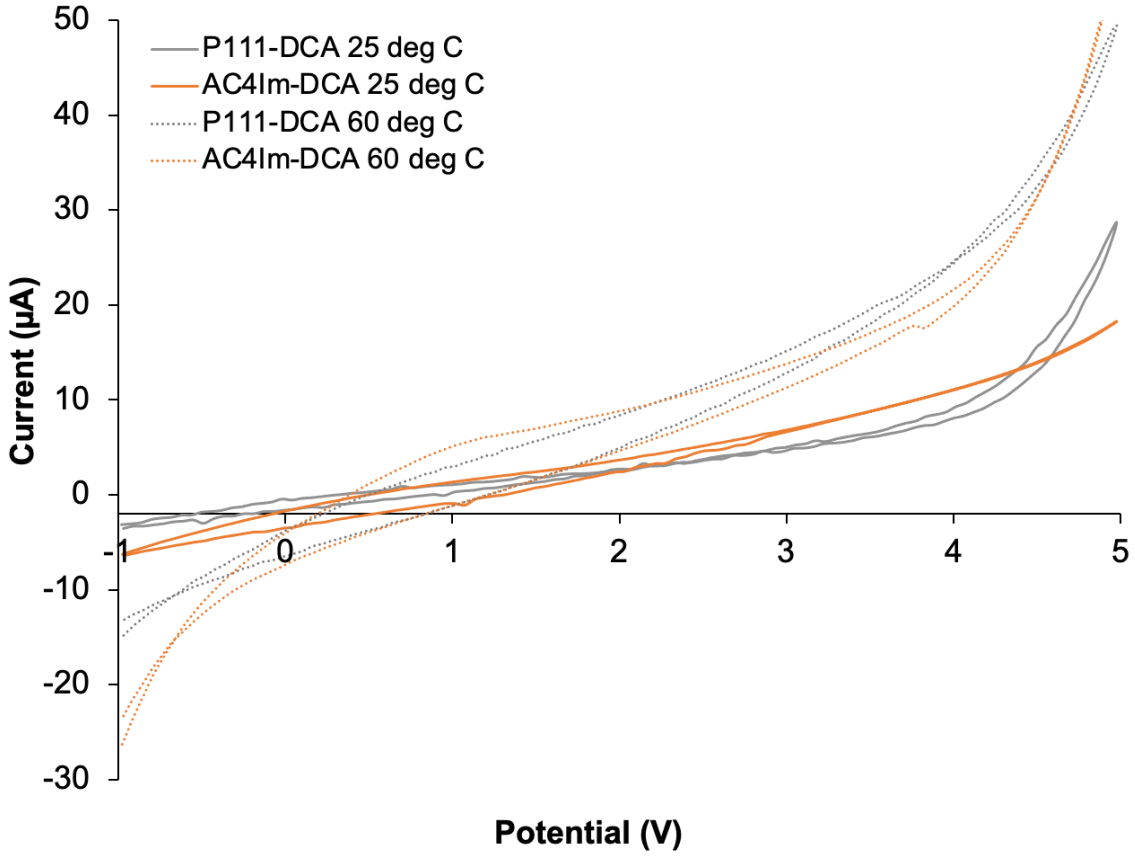

Fig. 5.3 Cyclic Voltammogram of P111-DCA and AC_4Im-DCA at 25 and 60 °C. Dotted lines represent data taken at 60 °C.

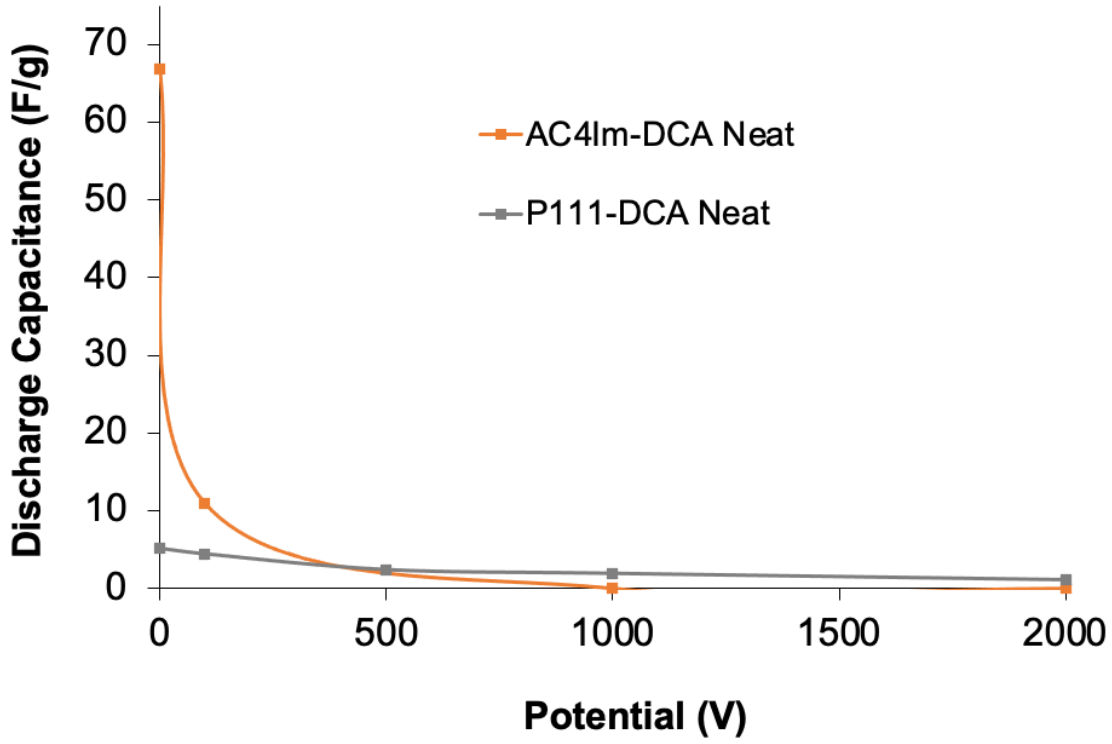

Fig. 5.4 Discharge Capacitance of AC_4Im-DCA and P111-DCA RTIL electrolytes in activated carbon electrode supercapacitors at 60 ^oC.

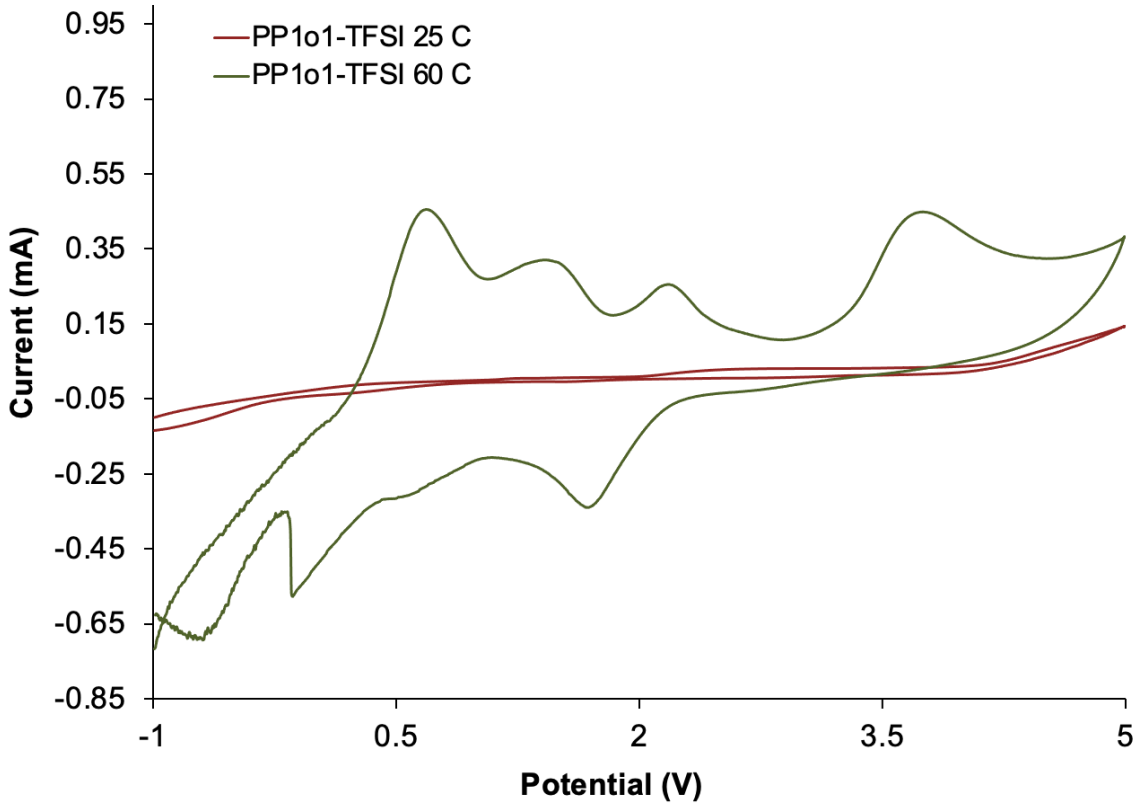

Fig. 5.5 Cyclic voltammograms of PP1o1-TFSI at 25 and 60 °C.

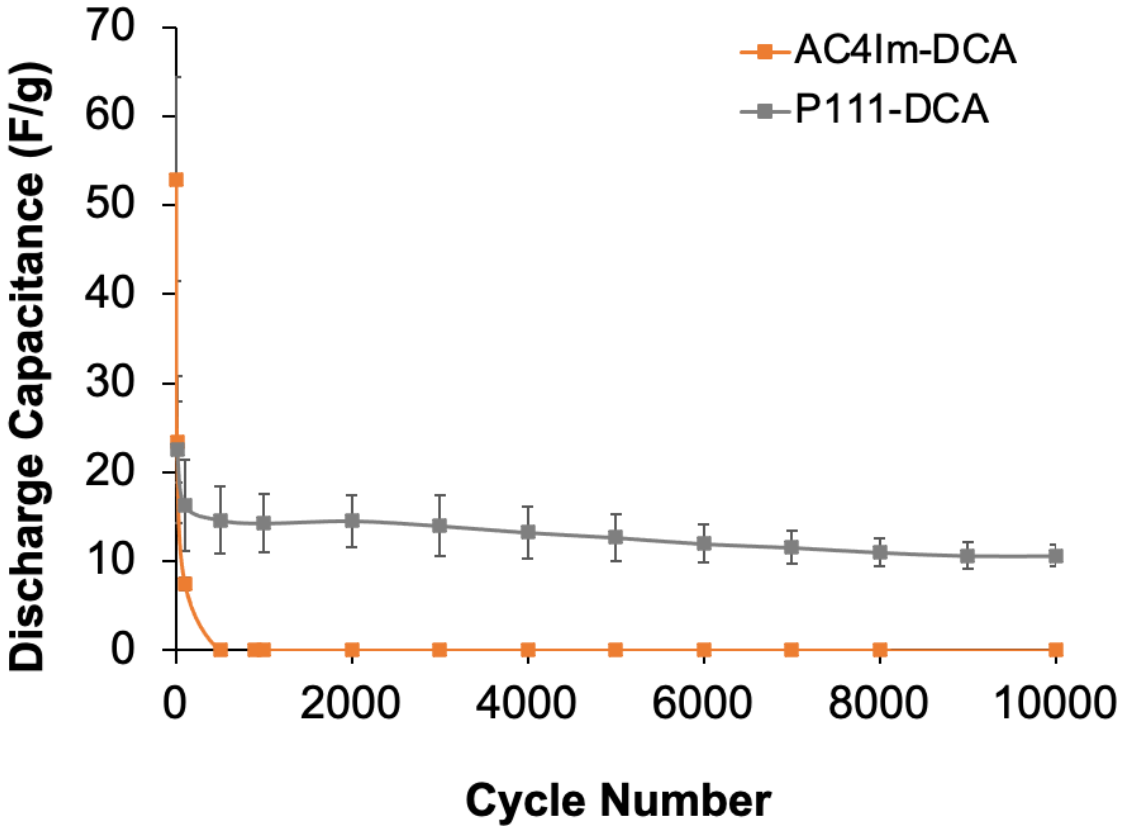

Fig. 5.6 Discharge Capacitance of AC_4Im-DCA and P111-DCA RTIL electrolytes in 30 wt% PP1o1-TFSI infused activated carbon electrode supercapacitors at 60 ºC (N = 3).

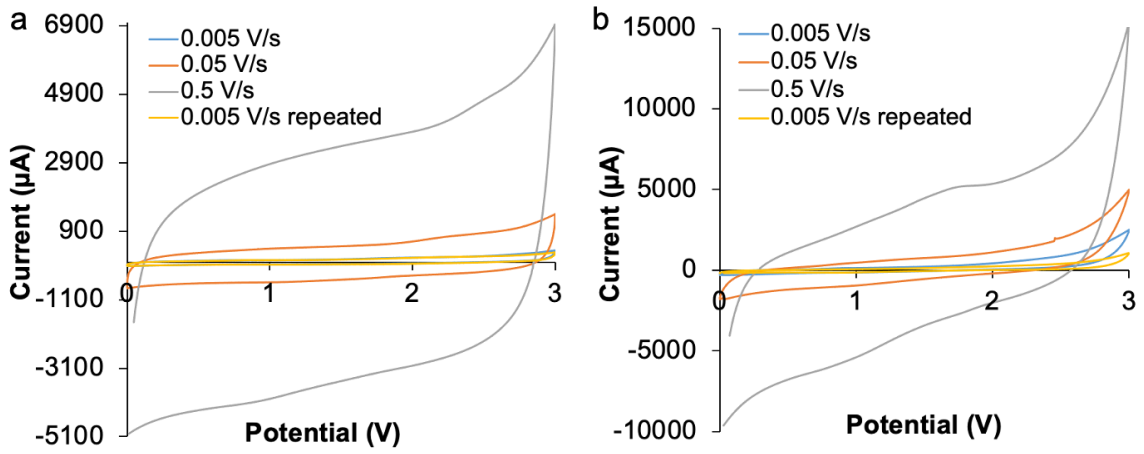

Fig. 5.7 (a) P111-DCA RTIL electrolyte in 30 wt% PP1o1-TFSI infused activated carbon electrode supercapacitor cyclic voltammogram at cycle 10 of various scan rates. (b) AC_4Im-DCA RTIL electrolyte in 30 wt% PP1o1-TFSI infused activated carbon electrodes supercapacitor cyclic voltammogram at cycle 10 of various scan rates.

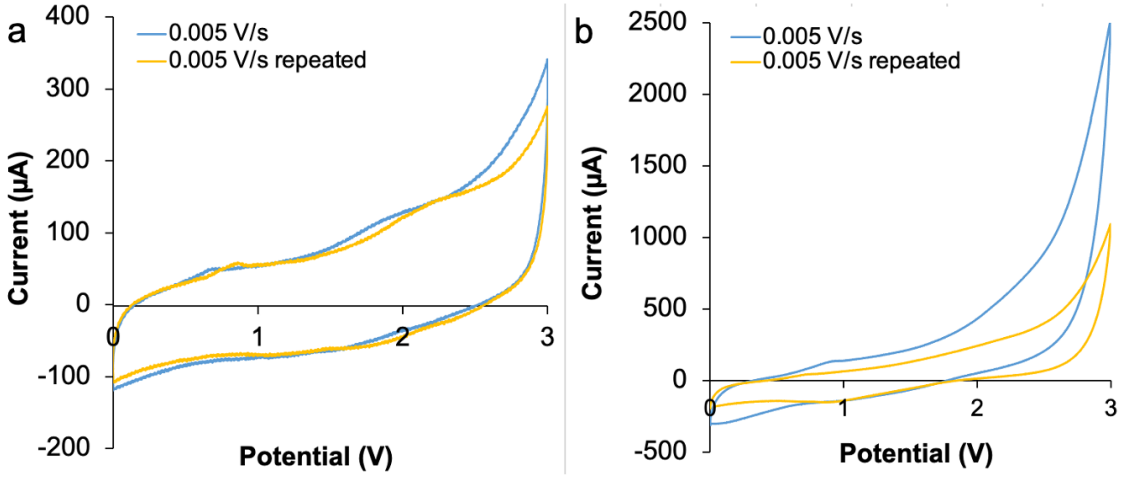

Fig. 5.8 (a) P111-DCA RTIL electrolyte in 30 wt% PP1o1-TFSI infused AC electrodes supercapacitor cyclic voltammogram at cycle 10 and cycle 40. (b) AC_4Im-DCA RTIL electrolyte in 30 wt% PP1o1-TFSI infused AC electrodes supercapacitor cyclic voltammogram at cycle 10 and cycle 40.

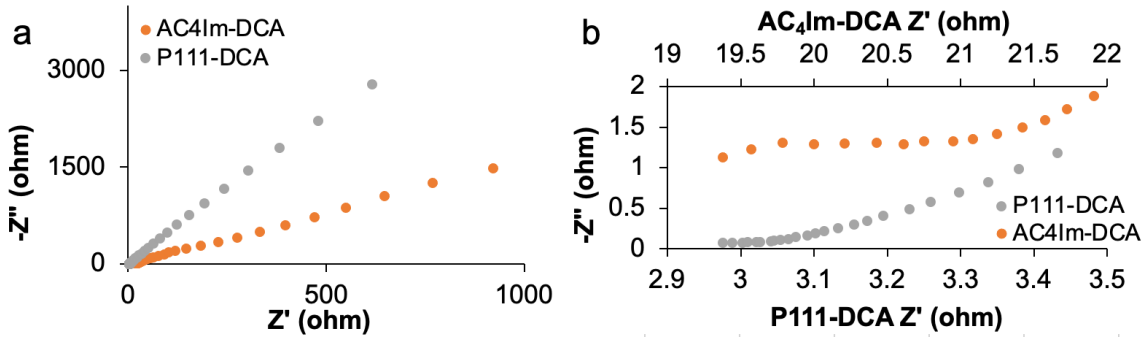

Fig. 5.9 (a) Nyquist plots of 30 wt% PP1o1-TFSI activated carbon electrode supercapacitors with RTIL electrolytes at 60 °C. (b) High Frequency region of Nyquist plot of 30 wt% PP1o1-TFSI activated carbon electrode supercapacitors with RTIL electrolytes at 60 °C.

Summary and Discussion

The safe operation of supercapacitors and lithium ion batteries at ambient and elevated temperatures is an integral component of future renewable energy and conversative initiatives. The design of high temperature energy storage (EES) devices requires the synthesis and characterization of novel thermally stable electrolyte solvents. Room temperature ionic liquids (RTILs) represent ideal replacement electrolytes with high thermal stability and inherent conductivity. Unfortunately, due to the strong ionic interaction present in RTILs, they tend to be highly viscous, resulting in high internal resistance in an EES device and low power and energy density. As such, low viscosity, highly conductive RTILs are required of candidate electrolyte solvents.

To design a RTIL with the necessary physiochemical properties, we synthesized and characterized three series of phosphonium based ILs to elucidate a structure-function relationship for future RTIL design. Each series of phosphonium ILs featured the incorporation of either a fluoro, sulfonyl or ether functional group into one side arm of the cation. By characterizing the thermal properties such as crystallization, melting, and thermal degradation temperature, as well as conductivity and viscosity, three key physical components of the RTIL structure design, which enable facile control of the physiochemical properties, were identified. 1). Inclusion of a large anion with a delocalized negative charge; 2). Tight control of alkyl chain lengths between 2 to 3 carbons long; and 3). Incorporation of ether functional group. By combining the three design features into a single RTIL structure we were able to generate a RTIL which features improved melting temperatures and conductivity viscosity. For example, P1o1-

TFSI features an ether moiety, the TFSI anion, and all alkyl chains are between 2 or 3 carbons long resulting in a RTIL that is a liquid at room temperature with high thermal stability, and the highest conductivity of all sixteen ILs synthesized, 3.14 mS/cm at 25 ^{o}C.

Using the three key structural components of RTILs, we designed a piperidinium based IL study which emulated the phosphonium study. Three RTILs were tested which contained a different number of ether moieties: no ether groups (1), one ether group (2), and two ether groups (3). The incorporation of the ether moiety, as established in the phosphonium series, lowers the melting point and viscosity while simultaneously increasing the conductivity of the system. The lowering of the viscosity enabled the generation of an RTIL electrolyte with 1.0 M LiTFSI salt that still displayed a moderate viscosity and conductivity (0.03 Pa.s and 9.2 mS/cm at 100 ^{o}C). When 2 with 1.0 M LiTFSI was equipped in an activated carbon supercapacitor, the coin cell functioned for over 10,000 cycles at 100 ^{o}C with a final discharge capacitance of 28 F/g and only a 30 % decrease in capacitance, whereas the common carbonate solvent electrolyte (propylene carbonate) with 1.0 M LiTFSI failed at cycle 3200 at the same temperature. Unfortunately, at room temperature, the RTIL electrolyte equipped cell had only moderate discharge capacitance under 10 F/g, while the carbonate solvent performed as expected.

By utilizing the structure-function relationship developed through the incorporation of the electronegative elements into the phosphonium structure in a new cation (piperidinium), we were able to validate the structure-function relationship. However, both the phosphonium and piperidinium studies were limited in scope as we only

manipulated one side chain in the phosphonium and piperidinium series. To further elucidate the effects the fluoro and sulfonyl functionalities have on the IL, the incorporation of an electronegative moiety onto two, three or four chains of the phosphonium cation is necessary. Moreover, while the manipulation of the cationic structure did result in an RTIL electrolyte system that increased the working temperature of the EES devices, the changes in viscosity and conductivity were moderate at ambient temperatures; resulting in an EES device with limited functionality at room temperature.

To further manipulate the resultant physical properties of the RTILs, an investigation into the effects of cation and anion pairing as well as the addition of lithium salts, on the physiochemical properties of the RTIL was completed. Three cations and four anions were mixed and matched to create nine unique ILs. The thermal stability, viscosity, conductivity and electrochemical stability of these ILs were measured and compared. It was found that the symmetrical phosphonium cation, compared to the asymmetrical imidazolium cation, tended to generate ILs with high melting points, and thus, solid compounds at ambient temperatures. The systems containing the dicyanamide anion (DCA) were found to have the highest conductivity and lowest viscosity of the generated ILs. And the ILs with an DCA anion and a cation that featured an ether moiety further displayed higher conductivity. Unfortunately, the introduction of the ether group into the RTILs lowered the electrochemical stability of the RTILs. Furthermore, it was observed that the electrochemical stability of the RTILs heavily depended on the pairings of the cation/anion. Both the TFSI and PF_6 anion displayed large and varied instabilities

regardless of the paired cation, while DCA displayed various stabilities depending on the cation paired.

Additional research is necessary to fully understand the effects ion pairing has on the electrochemical stability of the resultant RTILs. And more specifically, to elucidate why and the ether functionality drastically reduces the electrochemical stability of the RTIL while an olefin functionality has a minimal effect. Moreover, precise control of the water content of the various RTILs as well as a quantification of how water in the RTILs affects the electrochemical stability of the RTILs would further improve batch to batch variability.

From the above study, two RTILs were identified that have high conductivity, low viscosity, and a wide electrochemical stability window at room temperature and 60 ^{o}C: P111-DCA and AC_4Im-DCA. P111-DCA and AC_4Im-DCA both displayed the highest and lowest conductivities and viscosities of all the generated ILs at room temperature, 7.13 mS/cm and 0.043 Pa.s and 6.13 mS/cm and 0.054 Pa.s, respectively. Moreover, both neat RTILs are electrochemically stable from -1 to 5 V at 25 ^{o}C and from -1 to 4 V at 60 ^{o}C. Since both RTILs displayed such high electrochemical stability and moderate conductivity, it was rationalized that they could function as an electrolyte in a supercapacitor without the need for lithium salts. Using activated carbon electrodes that features the incorporation of 30 wt% N-methyl-methoxy-methyl-piperidinium bis(trifluoro-methane-sulfonyl)-imide (PP1o1-TFSI), to facilitate the movement of the RTILs into the electrode surface, supercapacitors were generated that functioned at 60 ^{o}C for over 10,000 cycles. The cells equipped with AC_4Im-DCA displayed quick capacity

fade and failure after 4,000 cycles, however the P111-DCA equipped cells functioned for 10,000 cycles with an average discharge capacity of 10 F/g.

The rapid discharge capacity exhibited by the AC_4Im-DCA anion is thought to be caused by the instability of the AC_4Im cation on the electrode surface. CV and EIS experiments corroborated this proposal, however, further experimentation focused on the electrode:electrolyte interface will elucidate two factors; 1). Why did the relatively electrochemically unstable piperidinium RTILs inclusion into the electrode enabled cycling of the cell while salts and different RTILs did not? And 2). Why did the AC_4Im cation display different electrochemical stability to lithium metal than to activated carbon? The development of novel RTIL electrolytes suitable for use at elevated and ambient temperatures will accelerate with a deeper understanding of cation and anion stability in RTILs in different environments and electrodes.

Bibliography

1. Simon, P.; Gogotsi, Y.; Dunn, B., Where Do Batteries End and Supercapacitors Begin? *Science* **2014,** *343*, 1210-1211.

2. Gogotsi, Y.; Penner, R. M., Energy Storage in Nanomaterials - Capacitive, Pseudocapacitive, or Battery-like? *ACS Nano* **2018,** *12*, 2081-2083.

3. Lin, X.; Salari, M.; Arava, L. M. R.; Ajayan, P. M.; Grinstaff, M. W., High Temperature Electrical Energy Storage: Advances, Challenges, and Frontiers. *Chemical Society Reviews* **2016,** *45*, 5848-5887.

4. Rogers, R. D.; Seddon, K. R., Chemistry. Ionic Liquids—Solvents of the Future? *Science* **2003,** *302*, 792-3.

5. Lian, C.; Liu, H.; Li, C.; Wu, J., Hunting Ionic Liquids with Large Electrochemical Potential Windows. *AIChE Journal* **2019,** *65*, 804-810.

6. Armand, M.; Endres, F.; MacFarlane, D. R.; Ohno, H.; Scrosati, B., Ionic-liquid Materials for the Electrochemical Challenges of the Future. *Nature Materials* **2009,** *8*, 621-629.

7. Ma, Z.; Yu, J.; Dai, S., Preparation of Inorganic Materials Using Ionic Liquids. *Advanced Materials* **2010,** *22*, 261-285.

8. Huang, J.-F.; Luo, H.; Dai, S., A New Strategy for Synthesis of Novel Classes of Room-Temperature Ionic Liquids Based on Complexation Reaction of Cations. *Journal of the Electrochemical Society* **2006,** *153*, J9-J13.

9. Luo, H. D., Sheng, A New Strategy Toward Synthesis of Room Temperature Ionic Liquids Based on Complexation Reactions of Cations. *ECS Proceedings Volumes* **2004,** *2004-24*, 340-345.

10. Tamura, T.; Yoshida, K.; Hachida, T.; Tsuchiya, M.; Nakamura, M.; Kazue, Y.; Tachikawa, N.; Dokko, K.; Watanabe, M., Physicochemical Properties of Glyme-Li Salt Complexes as a New Family of Room-Temperature Ionic Liquids. *Chemistry Letters* **2010,** *39*, 753-755.

11. Maton, C.; De Vos, N.; Stevens, C. V., Ionic Liquid Thermal Stabilities: Decomposition Mechanisms and Analysis Tools. *Chemical Society Reviews* **2013,** *42*, 5963-5977.

12. Lin, X.; Kavian, R.; Lu, Y.; Hu, Q.; Shao-Horn, Y.; Grinstaff, M. W., Thermally-Responsive, Nonflammable Phosphonium Ionic Liquid Electrolytes for Lithium Metal Batteries: Operating at 100 Degrees Celsius. *Chemical Science* **2015,** *6*, 6601-6606.

13. Watanabe, M.; Thomas, M. L.; Zhang, S.; Ueno, K.; Yasuda, T.; Dokko, K., Application of Ionic Liquids to Energy Storage and Conversion Materials and Devices. *Chemical Reviews* **2017,** *117*, 7190-7239.

14. Okoturo, O. O.; VanderNoot, T. J., Temperature Dependence of Viscosity for Room Temperature Ionic Liquids. *Journal of Electroanalytical Chemistry* **2004,** *568*, 167-181.

15. Feng, G.; Chen, M.; Bi, S.; Goodwin, Z. A. H.; Postnikov, E. B.; Brilliantov, N.; Urbakh, M.; Kornyshev, A. A., Free and Bound States of Ions in Ionic Liquids, Conductivity, and Underscreening Paradox. *Physical Review X* **2019,** *9*, 021024.

16. Yonekura, R.; Grinstaff, M. W., The Effects of Counterion Composition on the Rheological and Conductive Properties of Mono- and Diphosphonium Ionic Liquids. *Physical Chemistry Chemical Physics* **2014,** *16*, 20608-20617.

17. Matsumoto, R.; Thompson, M. W.; Cummings, P. T., Ion Pairing Controls Physical Properties of Ionic Liquid-Solvent Mixtures. *Journal of Physical Chemistry B* **2019,** *123*, 9944-9955.

18. Ruiz, V.; Huynh, T.; Sivakkumar, S. R.; Pandolfo, A. G., Ionic Liquid-Solvent Mixtures as Supercapacitor Electrolytes for Extreme Temperature Operation. *RSC Advances* **2012,** *2*, 5591-5598.

19. Kalhoff, J. G. E., Gebrekidan; Bresser, Dominic; Passerini, Stephano, Safer Electrolytes for Lithium-Ion Batteries: State of the Art and Perspectives. *ChemSUSChem* **2015,** *8*, 2154-2175.

20. Every, H.; Bishop, A. G.; Forsyth, M.; MacFarlane, D. R., Ion Diffusion in Molten Salt Mixtures. *Electrochimica Acta* **2000,** *45*, 1279-1284.

21. Montanino, M.; Moreno, M.; Alessandrini, F.; Appetecchi, G. B.; Passerini, S.; Zhou, Q.; Henderson, W. A., Physical and Electrochemical Properties of Binary Ionic Liquid Mixtures: (1–x) PYR14TFSI–(x) PYR14IM14. *Electrochimica Acta* **2012,** *60*, 163-169.

22. Brennecke, J. F.; Maginn, E. J., Ionic Liquids: Innovative Fluids for Chemical Processing. *AIChE Journal* **2001,** *47*, 2384-2389.

23. Taige, M. A.; Hilbert, D.; Schubert, T. J. S., Mixtures of Ionic Liquids as Possible Electrolytes for Lithium Ion Batteries. *Zeitschrift fuer Physikalische Chemie* **2012,** *226*, 129-139.

24. Lin, R.; Taberna, P.-L.; Fantini, S.; Presser, V.; Perez, C. R.; Malbosc, F.; Rupesinghe, N. L.; Teo, K. B. K.; Gogotsi, Y.; Simon, P., Capacitive Energy Storage from -50°C to 100°C Using an Ionic Liquid Electrolyte. *Journal of Physical Chemistry Letters* **2011,** *2*, 2396-2401.

25. Lian, C.; Liu, K.; Van Aken, K. L.; Gogotsi, Y.; Wesolowski, D. J.; Liu, H. L.; Jiang, D. E.; Wu, J. Z., Enhancing the Capacitive Performance of Electric Double-Layer Capacitors with Ionic Liquid Mixtures. *ACS Energy Letters* **2016,** *1*, 21-26.

26. Zhou, Y.; Ghaffari, M.; Lin, M.; Xu, H.; Xie, H.; Koo, C. M.; Zhang, Q. M., High Performance Supercapacitor Under Extremely Low Environmental Temperature. *RSC Advances* **2015,** *5*, 71699-71703.

27. Kornyshev, A. A., Double-Layer in Ionic Liquids: Paradigm Change? *Journal of Physical Chemistry B* **2007,** *111*, 5545-5557.

28. Kilic, M. S.; Bazant, M. Z.; Ajdari, A., Steric Effects in the Dynamics of Electrolytes at Large Applied Voltages. I. Double-Layer Charging. *Physical Review E: Statistical Physics, Plasmas, Fluids, and Related Interdisciplinary Topics* **2007,** *75*, 021502/1-021502/16.

29. Jiang, D.-e.; Meng, D.; Wu, J., Density Functional Theory for Differential Capacitance of Planar Electric Double Layers in Ionic Liquids. *Chemical Physics Letters* **2011,** *504*, 153-158.

30. Wu, J.; Jiang, T.; Jiang, D.-e.; Jin, Z.; Henderson, D., A Classical Density Functional Theory for Interfacial Layering of Ionic Liquids. *Soft Matter* **2011,** *7*, 11222-11231.

31. Bazant, M. Z.; Storey, B. D.; Kornyshev, A. A., Double Layer in Ionic Liquids. Overscreening versus Crowding. *Physical Review Letters* **2011,** *106*, 046102/1-046102/4.

32. Mezger, M.; Schroeder, H.; Reichert, H.; Schramm, S.; Okasinski, J. S.; Schoeder, S.; Honkimaeki, V.; Deutsch, M.; Ocko, B. M.; Ralston, J.; Rohwerder, M.; Stratmann, M.; Dosch, H., Molecular Layering of Fluorinated Ionic Liquids at a Charged Sapphire (0001) Surface. *Science* **2008,** *322*, 424-428.

33. Zhou, H.; Rouha, M.; Feng, G.; Lee, S. S.; Docherty, H.; Fenter, P.; Cummings, P. T.; Fulvio, P. F.; Dai, S.; McDonough, J.; Presser, V.; Gogotsi, Y., Nanoscale

Perturbations of Room Temperature Ionic Liquid Structure at Charged and Uncharged Interfaces. *ACS Nano* **2012,** *6*, 9818-9827.

34. Elbourne, A.; McDonald, S.; Voichovsky, K.; Endres, F.; Warr, G. G.; Atkin, R., Nanostructure of the Ionic Liquid-Graphite Stern Layer. *ACS Nano* **2015,** *9*, 7608-7620.

35. Hayes, R.; Borisenko, N.; Tam, M. K.; Howlett, P. C.; Endres, F.; Atkin, R., Double Layer Structure of Ionic Liquids at the Au(111) Electrode Interface: An Atomic Force Microscopy Investigation. *Journal of Physical Chemistry C* **2011,** *115*, 6855-6863.

36. Li, H.; Endres, F.; Atkin, R., Effect of Alkyl Chain Length and Anion Species on the Interfacial Nanostructure of Ionic Liquids at the Au(111)–Ionic Liquid Interface as a Function of Potential. *Physical Chemistry Chemical Physics* **2013,** *15*, 14624-14633.

37. Smith, A. M.; Lovelock, K. R. J.; Gosvami, N. N.; Licence, P.; Dolan, A.; Welton, T.; Perkin, S., Monolayer to Bilayer Structural Transition in Confined Pyrrolidinium-Based Ionic Liquids. *Journal of Physical Chemistry Letters* **2013,** *4*, 378-382.

38. Fedorov, M. V.; Georgi, N.; Kornyshev, A. A., Double Layer in Ionic Liquids: The Nature of the Camel Shape of Capacitance. *Electrochemistry Communications* **2010,** *12*, 296-299.

39. Tsai, W.-Y.; Come, J.; Zhao, W.; Wang, R.; Feng, G.; Prasad Thapaliya, B.; Dai, S.; Collins, L.; Balke, N., Hysteretic Order-Disorder Transitions of Ionic Liquid Double Layer Structure on Graphite. *Nano Energy* **2019,** *60*, 886-893.

40. Su, Y.-Z.; Fu, Y.-C.; Yan, J.-W.; Chen, Z.-B.; Mao, B.-W., Double Layer of Au(100)/Ionic Liquid Interface and Its Stability in Imidazolium-Based Ionic Liquids. *Angewandte Chemie, International Edition* **2009,** *48*, 5148-5151.

41. Uysal, A.; Zhou, H.; Feng, G.; Lee, S. S.; Li, S.; Cummings, P. T.; Fulvio, P. F.; Dai, S.; McDonough, J. K.; Gogotsi, Y.; Fenter, P., Interfacial Ionic 'Liquids': Connecting Static and Dynamic Structures. *Journal of Physics: Condensed Matter* **2014,** *27*, 032101.

42. Black, J. M.; Baris Okatan, M.; Feng, G.; Cummings, P. T.; Kalinin, S. V.; Balke, N., Topological Defects in Electric Double Layers of Ionic Liquids at Carbon Interfaces. *Nano Energy* **2015,** *15*, 737-745.

43. Lauw, Y.; Horne, M. D.; Rodopoulos, T.; Lockett, V.; Akgun, B.; Hamilton, W. A.; Nelson, A. R. J., Structure of [C4mpyr][NTf2] Room-Temperature Ionic Liquid at Charged Gold Interfaces. *Langmuir* **2012,** *28*, 7374-7381.

44. Wen, R.; Rahn, B.; Magnussen, O. M., Potential-Dependent Adlayer Structure and Dynamics at the Ionic Liquid/Au(111) Interface: A Molecular-Scale In Situ Video-STM Study. *Angewandte Chemie, International Edition* **2015,** *54*, 6062-6066.

45. Chu, M.; Miller, M.; Dutta, P., Crowding and Anomalous Capacitance at an Electrode-Ionic Liquid Interface Observed Using Operando X-Ray Scattering. *ACS Central Science* **2016,** *2*, 175-180.

46. Nishi, N.; Uchiyashiki, J.; Ikeda, Y.; Katakura, S.; Oda, T.; Hino, M.; Yamada, N. L., Potential-Dependent Structure of the Ionic Layer at the Electrode Interface of an Ionic Liquid Probed Using Neutron Reflectometry. *Journal of Physical Chemistry C* **2019,** *123*, 9223-9230.

47. Zhan, C.; Zhang, Y.; Cummings, P. T.; Jiang, D.-e., Computational Insight into the Capacitive Performance of Graphene Edge Planes. *Carbon* **2017,** *116*, 278-285.

48. Dyatkin, B.; Zhang, Y.; Mamontov, E.; Kolesnikov, A. I.; Cheng, Y.; Meyer, H. M.; Cummings, P. T.; Gogotsi, Y., Influence of Surface Oxidation on Ion Dynamics and Capacitance in Porous and Nonporous Carbon Electrodes. *Journal of Physical Chemistry C* **2016,** *120*, 8730-8741.

49. Dyatkin, B.; Osti, N. C.; Zhang, Y.; Wang, H.-W.; Mamontov, E.; Heller, W. T.; Zhang, P.; Rother, G.; Cummings, P. T.; Wesolowski, D. J.; Gogotsi, Y., Ionic Liquid Structure, Dynamics, and Electrosorption in Carbon Electrodes with Bimodal Pores and Heterogeneous Surfaces. *Carbon* **2018,** *129*, 104-118.

50. Kerisit, S.; Schwenzer, B.; Vijayakumar, M., Effects of Oxygen-Containing Functional Groups on Supercapacitor Performance. *Journal of Physical Chemistry Letters* **2014,** *5*, 2330-2334.

51. Zhang, Y.; Dyatkin, B.; Cummings, P. T., Molecular Investigation of Oxidized Graphene: Anatomy of the Double-Layer Structure and Ion Dynamics. *Journal of Physical Chemistry C* **2019,** *123*, 12583-12591.

52. Chmiola, J.; Yushin, G.; Gogotsi, Y.; Portet, C.; Simon, P.; Taberna, P. L., Anomalous Increase in Carbon Capacitance at Pore Sizes Less Than 1 Nanometer. *Science* **2006,** *313*, 1760-1763.

53. Largeot, C.; Portet, C.; Chmiola, J.; Taberna, P.-L.; Gogotsi, Y.; Simon, P., Relation between the Ion Size and Pore Size for an Electric Double-Layer Capacitor. *Journal of the American Chemical Society* **2008,** *130*, 2730-2731.

54. Wang, X.; Zhou, H.; Sheridan, E.; Walmsley, J. C.; Ren, D.; Chen, D., Geometrically Confined Favourable Ion Packing for High Gravimetric Capacitance in

Carbon-Ionic Liquid Supercapacitors. *Energy & Environmental Science* **2016,** *9*, 232-239.

55. Kondrat, S.; Perez, C. R.; Presser, V.; Gogotsi, Y.; Kornyshev, A. A., Effect of Pore Size and its Dispersity on the Energy Storage in Nanoporous Supercapacitors. *Energy & Environmental Science* **2012,** *5*, 6474-6479.

56. Druschler, M.; Borisenko, N.; Wallauer, J.; Winter, C.; Huber, B.; Endres, F.; Roling, B., New Insights Into the Interface Between a Single-Crystalline Metal Electrode and an Extremely Pure Ionic Liquid: Slow Interfacial Processes and the Influence of Temperature on Interfacial Dynamics. *Physical Chemistry Chemical Physics* **2012,** *14*, 5090-9.

57. Umebayashi, Y.; Mori, S.; Fujii, K.; Tsuzuki, S.; Seki, S.; Hayamizu, K.; Ishiguro, S.-i., Raman Spectroscopic Studies and Ab Initio Calculations on Conformational Isomerism of 1-Butyl-3-methylimidazolium Bis-(trifluoromethanesulfonyl)amide Solvated to a Lithium Ion in Ionic Liquids: Effects of the Second Solvation Sphere of the Lithium Ion. *Journal of Physical Chemistry B* **2010,** *114*, 6513-6521.

58. Ishihara, Y.; Miyazaki, K.; Fukutsuka, T.; Abe, T., Lithium-Ion Transfer at the Interface between High Potential Negative Electrodes and Ionic Liquids. *Journal of the Electrochemical Society* **2014,** *161*, A1939-A1942.

59. Matsumoto, H.; Sakaebe, H.; Tatsumi, K., Li/LiCoO2 Cell Performance Using Ionic Liquids Composed of N,N-diethyl-N-methyl-N-(2-methoxyethyl)ammonium - Effect of Anionic Structure. *ECS Transactions*. **2009,** *16*, 59-66.

60. Ishikawa, M.; Sugimoto, T.; Kikuta, M.; Ishiko, E.; Kono, M., Pure Ionic Liquid Electrolytes Compatible with a Graphitized Carbon Negative Electrode in Rechargeable Lithium-Ion Batteries. *Journal of Power Sources* **2006,** *162*, 658-662.

61. Balducci, A.; Schmuck, M.; Kern, W.; Rupp, B.; Passerini, S.; Winter, M., Ionic Liquids as Electrolyte in Lithium Batteries: in situ FTIRS Studies on the Use of Electrolyte Additives. *ECS Transactions* **2008,** *11*, 109-114.

62. Mun, J.; Jung, Y. S.; Yim, T.; Lee, H. Y.; Kim, H.-J.; Kim, Y. G.; Oh, S. M., Electrochemical Stability of Bis(trifluoromethanesulfonyl)imide-Based Ionic Liquids at Elevated Temperature as a Solvent for a Titanium Oxide Bronze Electrode. *Journal of Power Sources* **2009,** *194*, 1068-1074.

63. Garcia, B.; Lavallee, S.; Perron, G.; Michot, C.; Armand, M., Room Temperature Molten Salts as Lithium Battery Electrolyte. *Electrochimica Acta* **2004,** *49*, 4583-4588.

64. Wang, Y.; Zaghib, K.; Guerfi, A.; Bazito, F. F. C.; Torresi, R. M.; Dahn, J. R., Accelerating Rate Calorimetry Studies of the Reactions Between Ionic Liquids and Charged Lithium Ion Battery Electrode Materials. *Electrochimica Acta* **2007,** *52*, 6346-6352.

65. Waldmann, T.; Wilka, M.; Kasper, M.; Fleischhammer, M.; Wohlfahrt-Mehrens, M., Temperature Dependent Ageing Mechanisms in Lithium-Ion Batteries - A Post-Mortem Study. *Journal of Power Sources* **2014,** *262*, 129-135.

66. Markevich, E.; Salitra, G.; Rosenman, A.; Talyosef, Y.; Aurbach, D.; Garsuch, A., High Performance of Thick Amorphous Columnar Monolithic Film Silicon Anodes in Ionic Liquid Electrolytes at Elevated Temperature. *RSC Advances* **2014,** *4*, 48572-48575.

67. Ababtain, K.; Babu, G.; Lin, X.; Rodrigues, M.-T. F.; Gullapalli, H.; Ajayan, P. M.; Grinstaff, M. W.; Arava, L. M. R., Ionic Liquid-Organic Carbonate Electrolyte Blends To Stabilize Silicon Electrodes for Extending Lithium Ion Battery Operability to 100 °C. *ACS Applied Materials & Interfaces* **2016,** *8*, 15242-15249.

68. Rodrigues, M.-T. F.; Sayed, F. N.; Gullapalli, H.; Ajayan, P. M., High-Temperature Solid Electrolyte Interphases (SEI) in Graphite Electrodes. *Journal of Power Sources* **2018,** *381*, 107-115.

69. Kerr, R.; Mazouzi, D.; Eftekharnia, M.; Lestriez, B.; Dupre, N.; Forsyth, M.; Guyomard, D.; Howlett, P. C., High-Capacity Retention of Si Anodes Using a Mixed Lithium/Phosphonium Bis(fluorosulfonyl)imide Ionic Liquid Electrolyte. *ACS Energy Letters* **2017,** *2*, 1804-1809.

70. Gowda, S. R.; Pushparaj, V.; Herle, S.; Girishkumar, G.; Gordon, J. G.; Gullapalli, H.; Zhan, X.; Ajayan, P. M.; Reddy, A. L. M., Three-Dimensionally Engineered Porous Silicon Electrodes for Li Ion Batteries. *Nano Letters* **2012,** *12*, 6060-6065.

71. Griffin, J. M.; Forse, A. C.; Wang, H.; Trease, N. M.; Taberna, P.-L.; Simon, P.; Grey, C. P., Ion Counting in Supercapacitor Electrodes Using NMR Spectroscopy. *Faraday Discussions* **2014,** *176*, 49-68.

72. Sakaebe, H.; Matsumoto, H., N-Methyl-N-Propyliperidinium Bis(trifluoromethanesulfonyl)imide (PP13-TFSI) - Novel Electrolyte Base for Li Battery. *Electrochemistry Communications* **2003,** *5*, 594-598.

73. Cho, J.; Jeong, S.; Kim, Y., Commercial and Research Battery Technologies for Electrical Energy Storage Applications. *Progress in Energy and Combustion Science* **2015,** *48*, 84-101.

74. Vioux, A.; Coasne, B., From Ionogels to Biredox Ionic Liquids: Some Emerging Opportunities for Electrochemical Energy Storage and Conversion Devices. *Advanced Energy Materials* **2017,** *7*, 1700883-n/a.

75. Goodenough, J. B.; Kim, Y., Challenges for Rechargeable Li Batteries. *Chemistry of Materials* **2010,** *22*, 587-603.

76. Choi, N.-S.; Chen, Z.; Freunberger, S. A.; Ji, X.; Sun, Y.-K.; Amine, K.; Yushin, G.; Nazar, L. F.; Cho, J.; Bruce, P. G., Challenges Facing Lithium Batteries and Electrical Double-Layer Capacitors. *Angewandte Chemie, International Edition* **2012,** *51*, 9994-10024.

77. Tarascon, J. M.; Armand, M., Issues and Challenges Facing Rechargeable Lithium Batteries. *Nature* **2001,** *414*, 359-367.

78. Yang, Q.; Zhang, Z.; Sun, X.-G.; Hu, Y.-S.; Xing, H.; Dai, S., Ionic Liquids and Derived Materials for Lithium and Sodium Batteries. *Chemical Society Reviews* **2018,** *47*, 2020-2064.

79. Zhang, L.; Tsay, K.; Bock, C.; Zhang, J., Ionic Liquids as Electrolytes for Non-Aqueous Solutions Electrochemical Supercapacitors in a Temperature Range of 20 °C-80 °C. *Journal of Power Sources* **2016,** *324*, 615-624.

80. Alcicek, G.; Gualous, H.; Venet, P.; Gallay, R.; Miraoui, A., *Experimental Study of Temperature Effect on Ultracapacitor Ageing*. 2007 European Conference on Power Electronics and Applications, Aalborg: Aalbog, Denmark, 2007; p 1-7.

81. Aricò, A. S.; Bruce, P.; Scrosati, B.; Tarascon, J.-M.; van Schalkwijk, W., Nanostructured Materials for Advanced Energy Conversion and Storage Devices. *Nature Materials* **2005,** *4*, 366-377.

82. Etacheri, V.; Marom, R.; Elazari, R.; Salitraa, G.; Aurbach, D., Challenges in the Development of Advanced Li-Ion Batteries: A Review. *Energy & Environmental Science* **2011,** *4*, 3243-3262.

83. Goodenough, J. B.; Park, K.-S., The Li-Ion Rechargeable Battery: A Perspective. *Journal of the American Chemical Society* **2013,** *135*, 1167-1176.

84. Simon, P.; Gogotsi, Y., Materials for Electrochemical Capacitors. *Nature Materials* **2008,** *7*, 845-854.

85. Cheng, F.; Liang, J.; Tao, Z.; Chen, J., Functional Materials for Rechargeable Batteries. *Advanced Materials* **2011,** *23*, 1695-1715.

86. Shi, C.; Dai, J.; Shen, X.; Peng, L.; Li, C.; Wang, X.; Zhang, P.; Zhao, J., A High-Temperature Stable Ceramic-Coated Separator Prepared with Polyimide Binder/Al2O3 Particles for Lithium-Ion Batteries. *Journal of Membrane Science* **2016,** *517*, 91-99.

87. l'Abee, R.; DaRosa, F.; Armstrong, M. J.; Hantel, M. M.; Mourzagh, D., High Temperature Stable Li-Ion Battery Separators Based on Polyetherimides with Improved Electrolyte Compatibility. *Journal of Power Sources* **2017,** *345*, 202-211.

88. Lin, X.; Varela, J. C.; Grinstaff, M. W., Synthesis of Ionic Liquid Based Electrolytes, Assembly of Li-ion Batteries, and Measurements of Performance at High Temperature. *Journal of Visualized Experiments* **2016**, e54864-e54864.

89. Lane, G. H.; Bayley, P. M.; Clare, B. R.; Best, A. S.; MacFarlane, D. R.; Forsyth, M.; Hollenkamp, A. F., Ionic Liquid Electrolyte for Lithium Metal Batteries: Physical, Electrochemical, and Interfacial Studies of N-Methyl-N-butylmorpholinium Bis(fluorosulfonyl)imide. *Journal of Physical Chemistry C* **2010,** *114*, 21775-21785.

90. Gao, X.; Qu, Q.; Zhu, G.; Gao, T.; Qian, F.; Shi, Q.; Zheng, H., Piperidinium-Based Ionic Liquid Electrolyte with Linear Solvent and LiODFB for LiFePO4/Li Cells at Room and High Temperature. *RSC Advances* **2017,** *7*, 50135-50142.

91. Abbott, A.; Aldous, L.; Borisenko, N.; Coles, S.; Fontaine, O.; Gamarra Garcia, J. D.; Gardas, R.; Hammond, O.; Hardwick, L. J.; Haumesser, P.-H.; Hausen, F.; Horwood, C.; Jacquemin, J.; Jones, R.; Jonsson, E.; Lahiri, A.; MacFarlane, D.; Marlair, G.; May, B.; Medhi, H.; Paschoal, V. H.; Reid, J. E. S. J.; Schoetz, T.; Tamura, K.; Thomas, M. L.; Tiwari, S.; Uralcan, B.; van den Bruinhorst, A.; Watanabe, M.; Wishart, J., Electrochemistry: General Discussion. *Faraday Discussions* **2018,** *206*, 405-426.

92. Bhosale, V. K.; Kulkarni, P. S., Ultrafast Igniting, Imidazolium Based Hypergolic Ionic Liquids with Enhanced Hydrophobicity. *New Journal of Chemistry* **2017,** *41*, 1250-1258.

93. Tsunashima, K.; Sugiya, M., Physical and Electrochemical Properties of Low-Viscosity Phosphonium Ionic Liquids as Potential Electrolytes. *Electrochemistry Communications* **2007,** *9*, 2353-2358.

94. Salari, M.; Cooper, B. G.; Zhang, H.; Grinstaff, M. W., Synthesis of an Environmentally Friendly Alkyl Carbonate Electrolyte Based on Glycerol for Lithium-Ion Supercapacitor Operation at 100 °C. *Advanced Sustainable Systems* **2017,** *1*, 1700067-n/a.

95. Gray, F. M., *Solid Polymer Electrolytes: Fundamentals and Technological Applications*. VCH Publishers: New York, 1991.

96. Konieczynska, M. D.; Lin, X.; Zhang, H.; Grinstaff, M. W., Synthesis of Aliphatic Poly(ether 1,2-glycerol carbonate)s via Copolymerization of CO2 with Glycidyl Ethers Using a Cobalt Salen Catalyst and Study of a Thermally Stable Solid Polymer Electrolyte. *ACS Macro Letters* **2015,** *4*, 533-537.

97. Fang, L.; Hu, Y.; Qi, J.; Chen, Y.; Zhang, H.; Huang, H., The Physical and Electrochemical Properties of the Ionic Liquids Based on N-Ethylpiperidinium Cations and TFSI Anion. *Electrochimica Acta* **2014,** *133*, 440-445.

98. Belhocine, T.; Forsyth, S. A.; Gunaratne, H. Q. N.; Nieuwenhuyzen, M.; Nockemann, P.; Puga, A. V.; Seddon, K. R.; Srinivasan, G.; Whiston, K., 3-Methylpiperidinium Ionic Liquids. *Physical Chemistry Chemical Physics* **2015,** *17*, 10398-10416.

99. Matsumoto, H.; Sakaebe, H.; Tatsumi, K.; Kikuta, M.; Ishiko, E.; Kono, M., Fast Cycling of Li/LiCoO2 Cell with Low-Viscosity Ionic Liquids Based on Bis(fluorosulfonyl)imide [FSI]−. *Journal of Power Sources* **2006,** *160*, 1308-1313.

100. Yim, T.; Lee, H. Y.; Kim, H.-J.; Mun, J.; Kim, S.; Oh, S. M.; Kim, Y. G., Synthesis and Properties of Pyrrolidinium and Piperidinium Bis(trifluoromethanesulfonyl)imide Ionic Liquids with Allyl Substituents. *Bulletin of the Korean Chemical Society* **2007,** *28*, 1567-1572.

101. Tot, A.; Podlipnik, Č.; Bešter-Rogač, M.; Gadžurić, S.; Vraneš, M., Influence of Oxygen Functionalization on Physico-Chemical Properties of Imidazolium Based Ionic Liquids – Experimental and Computational Study. *Arabian Journal of Chemistry* **2017**.

102. Kim, J.-H.; Woo, H.-S.; Jin, S.-J.; Lee, J. S.; Kim, W.; Ryu, K.; Kim, D.-W., Lithium-Oxygen Batteries with Ester-Functionalized Ionic Liquid-Based Electrolytes. *RSC Advances* **2015,** *5*, 80014-80021.

103. Seki, S.; Hayamizu, K.; Tsuzuki, S.; Takahashi, K.; Ishino, Y.; Kato, M.; Nozaki, E.; Watanabe, H.; Umebayashi, Y., Density, Viscosity, Ionic Conductivity, and Self-Diffusion Coefficient of Organic Liquid Electrolytes: Part I. Propylene Carbonate + Li, Na, Mg and Ca Cation Salts. *Journal of the Electrochemical Society* **2018,** *165*, A542-A546.

104. Nokami, T.; Matsumoto, K.; Itoh, T.-a.; Fukaya, Y.; Itoh, T., Synthesis of Ionic Liquids Equipped with 2-Methoxyethoxymethyl/Methoxymethyl Groups Using a Simple Microreactor System. *Organic Process Research & Development* **2014,** *18*, 1367-1371.

105. Neale, A. R.; Murphy, S.; Goodrich, P.; Hardacre, C.; Jacquemin, J., Thermophysical and Electrochemical Properties of Ethereal Functionalised Cyclic Alkylammonium-based Ionic Liquids as Potential Electrolytes for Electrochemical

Applications. *Chemphyschem : a European journal of chemical physics and physical chemistry* **2017,** *18*, 2040-2057.

106. Grimme, S.; Ehrlich, S.; Goerigk, L., Effect of the Damping Function in Dispersion Corrected Density Functional Theory. *Journal of Computational Chemistry* **2011,** *32*, 1456-1465.

107. Lage-Estebanez, I.; del Olmo, L.; Lopez, R.; Garcia de la Vega, J. M., The Role of Errors Related to DFT Methods in Calculations Involving Ion Pairs of Ionic Liquids. *Journal of Computational Chemistry* **2017,** *38*, 530-540.

108. Izgorodina, E. I.; Bernard, U. L.; MacFarlane, D. R., Ion-Pair Binding Energies of Ionic Liquids: Can DFT Compete with ab initio-Based Methods? *Journal of Physical Chemistry A* **2009,** *113*, 7064-72.

109. Curtiss, L. A.; Redfern, P. C.; Raghavachari, K., Assessment of Gaussian-3 and Density-Functional Theories on the G3/05 Test Set of Experimental Energies. *Journal of Chemical Physics* **2005,** *123*, 124107/1-12.

110. Kötz, R.; Hahn, M.; Gallay, R., Temperature Behavior and Impedance Fundamentals of Supercapacitors. *Journal of Power Sources* **2006,** *154*, 550-555.

111. Hung, K.; Masarapu, C.; Ko, T.; Wei, B., Wide-Temperature Range Operation Supercapacitors from Nanostructured Activated Carbon Fabric. *Journal of Power Sources* **2009,** *193*, 944-949.

112. Wright, D. R.; Garcia-Araez, N.; Owen, J. R., Review on High Temperature Secondary Li-Ion Batteries. *Energy Procedia* **2018,** *151*, 174-181.

113. Li, M.; Lu, J.; Chen, Z.; Amine, K., 30 Years of Lithium-Ion Batteries. *Advanced Materials* **2018,** *30*, 1800561.

114. Chen, S.; Wen, K.; Fan, J.; Bando, Y.; Golberg, D., Progress and Future Prospects of High-Voltage and High-Safety Electrolytes in Advanced Lithium Batteries: From Liquid to Solid Electrolytes. *Journal of Materials Chemistry A* **2018,** *6*, 11631-11663.

115. Chapman Varela, J.; Sankar, K.; Hino, A.; Lin, X.; Chang, W.-s.; Coker, D.; Grinstaff, M., Piperidinium Ionic Liquids as Electrolyte Solvents for Sustained High Temperature Supercapacitor Operation. *Chemical Communications* **2018,** *54*, 5590-5593.

116. Liu, Y.-S.; Pan, G.-B., Ionic Liquids for the Future Electrochemical Applications. In *Ionic Liquids: Applications and Perspectives*, Kokorin, A., Ed. InTech: 2011; pp 627-642.

117. Tsunashima, K.; Kodama, S.; Sugiya, M.; Kunugi, Y., Physical and Electrochemical Properties of Room-Temperature Dicyanamide Ionic Liquids Based on Quaternary Phosphonium Cations. *Electrochimica Acta* **2010,** *56*, 762-766.

118. Dunstan, T. D. J.; Caja, J., Development of Low Melting Ionic Liquids Using Eutectic Mixtures of Imidazolium and Pyrazolium Ionic Liquids. *ECS Transactions* **2007,** *3*, 21-32.

119. Moreno, M.; Simonetti, E.; Appetecchi, G. B.; Carewska, M.; Montanino, M.; Kim, G. T.; Loeffler, N.; Passerini, S., Ionic Liquid Electrolytes for Safer Lithium Batteries. *Journal of the Electrochemical Society* **2016,** *164*, A6026-A6031.

120. Lane, G. H.; Best, A. S.; MacFarlane, D. R.; Hollenkamp, A. F.; Forsyth, M., An Azo-Spiro Mixed Ionic Liquid Electrolyte for Lithium Metal–LiFePO[sub 4] Batteries. *Journal of the Electrochemical Society* **2010,** *157*, A876.

121. Neale, A. R.; Schütter, C.; Wilde, P.; Goodrich, P.; Hardacre, C.; Passerini, S.; Balducci, A.; Jacquemin, J., Physical–Chemical Characterization of Binary Mixtures of 1-Butyl-1-methylpyrrolidinium Bis{(trifluoromethyl)sulfonyl}imide and Aliphatic Nitrile Solvents as Potential Electrolytes for Electrochemical Energy Storage Applications. *Journal of Chemical & Engineering Data* **2017,** *62*, 376-390.

122. Vogl, T.; Passerini, S.; Balducci, A., The Impact of Mixtures of Protic Ionic Liquids on the Operative Temperature Range of Use of Battery Systems. *Electrochemistry Communications* **2017,** *78*, 47-50.

123. Navia, P.; Troncoso, J.; Romani, L., Viscosities for Ionic Liquid Binary Mixtures with a Common Ion. *Journal of Solution Chemistry* **2008,** *37*, 677-688.

124. Martins, V. L.; Sanchez-Ramirez, N.; Ribeiro, M. C. C.; Torresi, R. M., Two Phosphonium Ionic Liquids with High Li+ Transport Number. *Physical Chemistry Chemical Physics* **2015,** *17*, 23041-23051.

125. Fraser, K. J.; MacFarlane, D. R., Phosphonium-Based Ionic Liquids: An Overview. *Australian Journal of Chemistry* **2009,** *62*, 309-321.

126. Tsunashima, K.; Kawabata, A.; Matsumiya, M.; Kodama, S.; Enomoto, R.; Sugiya, M.; Kunugi, Y., Low Viscous and Highly Conductive Phosphonium Ionic Liquids Based on Bis(fluorosulfonyl)amide Anion as Potential Electrolytes. *Electrochemistry Communications* **2011,** *13*, 178-181.

127. Bradaric, C. J.; Downard, A.; Kennedy, C.; Robertson, A. J.; Zhou, Y., Industrial Preparation of Phosphonium Ionic Liquids. *Green Chemistry* **2003,** *5*, 143-152.

128. Zhang, Q.; Ma, X.; Liu, S.; Yang, B.; Lu, L.; He, Y.; Deng, Y., Hydrophobic 1-Allyl-3-Alkylimidazolium Dicyanamide Ionic Liquids with Low Densities. *Journal of Materials Chemistry* **2011,** *21*, 6864-6868.

129. Nguyen, D. Q.; Bae, H. W.; Jeon, E. H.; Lee, J. S.; Cheong, M.; Kim, H.; Kim, H. S.; Lee, H., Zwitterionic Imidazolium Compounds with High Cathodic Stability as Additives for Lithium Battery Electrolytes. *Journal of Power Sources* **2008,** *183*, 303-309.

130. Wilken, S.; Xiong, S.; Scheers, J.; Jacobsson, P.; Johansson, P., Ionic Liquids in Lithium Battery Electrolytes: Composition Versus Safety and Physical Properties. *Journal of Power Sources* **2015,** *275*, 935-942.

131. Kazemiabnavi, S.; Zhang, Z.; Thornton, K.; Banerjee, S., Electrochemical Stability Window of Imidazolium-Based Ionic Liquids as Electrolytes for Lithium Batteries. *The Journal of Physical Chemistry B* **2016,** *120*, 5691-5702.

132. Fang, S.; Zhang, Z.; Jin, Y.; Yang, L.; Hirano, S.-i.; Tachibana, K.; Katayama, S., New Functionalized Ionic Liquids Based on Pyrrolidinium and Piperidinium Cations with Two Ether Groups as Electrolytes for Lithium Battery. *Journal of Power Sources* **2011,** *196*, 5637-5644.

133. Rodrigues, M.-T. F.; Lin, X.; Gullapalli, H.; Grinstaff, M. W.; Ajayan, P. M., Rate Limiting Activity of Charge Transfer During Lithiation from Ionic Liquids. *Journal of Power Sources* **2016,** *330*, 84-91.

134. Chen, Z. J.; Xue, T.; Lee, J.-M., What Causes the Low Viscosity of Ether-Functionalized Ionic Liquids? Its Dependence on the Increase of Free Volume. *RSC Advances* **2012,** *2*, 10564-10574.

135. Zheng, J.; Engelhard, M. H.; Mei, D.; Jiao, S.; Polzin, B. J.; Zhang, J.-G.; Xu, W., Electrolyte Additive Enabled Fast Charging and Stable Cycling Lithium Metal Batteries. *Nature Energy* **2017,** *2*, 17012.

136. Tran, A. N.; Van Do, T.-N.; Le, L.-P. M.; Le, T. N., Synthesis of New Fluorinated Imidazolium Ionic Liquids and their Prospective Function as the Electrolytes for Lithium-Ion Batteries. *Journal of Fluorine Chemistry* **2014,** *164*, 38-43.

137. Yoon, H.; Lane, G. H.; Shekibi, Y.; Howlett, P. C.; Forsyth, M.; Best, A. S.; MacFarlane, D. R., Lithium Electrochemistry and Cycling Behaviour of ionic Liquids Using Cyano Based Anions. *Energy & Environmental Science* **2013,** *6*, 979-986.

138. Huang, Q.; Lourenço, T. C.; Costa, L. T.; Zhang, Y.; Maginn, E. J.; Gurkan, B., Solvation Structure and Dynamics of Li+ in Ternary Ionic Liquid–Lithium Salt Electrolytes. *The Journal of Physical Chemistry B* **2019,** *123*, 516-527.

139. Forsyth, M.; Hilder, M.; Zhang, Y.; Chen, F.; Carre, L.; Rakov, D. A.; Armand, M.; Macfarlane, D. R.; Pozo-Gonzalo, C.; Howlett, P. C., Tuning Sodium Interfacial Chemistry with Mixed-Anion Ionic Liquid Electrolytes. *ACS Applied Materials & Interfaces* **2019,** *11*, 43093-43106.

140. MacFarlane, D. R.; Golding, J.; Forsyth, S.; Forsyth, M.; Deacon, G. B., Low Viscosity Ionic Liquids Based on Organic Salts of the Dicyanamide Anion. *Chemical Communications* **2001**, 1430-1431.

141. Lerch, S.; Strassner, T., Expanding the Electrochemical Window: New Tunable Aryl Alkyl Ionic Liquids (TAAILs) with Dicyanamide Anions. *Chemistry – A European Journal* **2019,** *25*, 16251-16256.

142. Yoshida, Y.; Baba, O.; Saito, G., Ionic Liquids Based on Dicyanamide Anion: Influence of Structural Variations in Cationic Structures on Ionic Conductivity. *The Journal of Physical Chemistry B* **2007,** *111*, 4742-4749.

143. Zarrougui, R.; Hachicha, R.; Rjab, R.; Messaoudi, S.; Ghodbane, O., Physicochemical Characterizations of Novel Dicyanamide-Based Ionic Liquids Applied as Electrolytes for Supercapacitors. *RSC Advances* **2018,** *8*, 31213-31223.

144. Fillion, J. J.; Brennecke, J. F., Viscosity of Ionic Liquid-Ionic Liquid Mixtures. *Journal of Chemical & Engineering Data* **2017,** *62*, 1884-1901.

145. Chatel, G.; Pereira, J. F. B.; Debbeti, V.; Wang, H.; Rogers, R. D., Mixing Ionic Liquids - “Simple Mixtures" or “Double Salts"? *Green Chemistry* **2014,** *16*, 2051-2083.

146. Lui, M. Y.; Crowhurst, L.; Hallett, J. P.; Hunt, P. A.; Niedermeyer, H.; Welton, T., Salts Dissolved in Salts: Ionic Liquid Mixtures. *Chemical Science* **2011,** *2*, 1491-1496.

147. Thoms, E.; Sippel, P.; Reuter, D.; Weiß, M.; Loidl, A.; Krohns, S., Dielectric Study on Mixtures of Ionic Liquids. *Scientific Reports* **2017,** *7*, 7463.

148. Kwon, K.; Evans, J. W., Viscosity Changes of Li Battery Electrolytes and Their Long-Term Effect on the Frequency of EQCM Electrodes. *Electrochemical and Solid-State Letters* **2002,** *5*, A59-A61.

149. Hu, F.; Song, T., Application of Functionalized Ether in Lithium Ion Batteries. *RSC Advances* **2017,** *7*, 54203-54212.

150. Kishimura, H.; Kohki, E.; Nakada, A.; Tamatani, K.; Abe, H., Ether Bond Effects in Quaternary Ammonium and Phosphonium Ionic Liquid-Propanol Solutions. *Chemical Physics* **2018,** *502*, 87-95.

151. Reckeweg, O.; Di Salvo, F. J.; Schulz, A.; Blaschkowski, B.; Jagiella, S.; Schleid, T., Synthesis, Crystal Structure, and Vibrational Spectra of the Anhydrous Lithium Dicyanamide Li[N(CN)2]. *Zeitschrift fuer Anorganische und Allgemeine Chemie* **2014,** *640*, 851-855.

152. Shin, J. H.; Rupert, B. L.; Irwin, L. J.; Beer, L.; Worlikar, S. A.; Shi, S. Z. Electrolyte Compositions, Methods of Making and Battery Devices Formed There From. US20130095392A1, 2013.

153. Chanson, C. W., J-P, The European Association for Advanced Rechargeable Batteries: Safety of Lithium Ion Batteries. *RECHARGE aisbl* **2013**, 1-25.

154. Roth, E. P.; Orendorff, C. J., How Electrolytes Influence Battery Safety. *Electrochemical Society Interface* **2012,** *21*, 45-49.

155. Rodrigues, M.-T. F.; Babu, G.; Gullapalli, H.; Kalaga, K.; Sayed, F. N.; Kato, K.; Joyner, J.; Ajayan, P. M., A Materials Perspective on Li-Ion Batteries at Extreme Temperatures. *Nature Energy* **2017,** *2*, 17108.

156. Waqas, M.; Tan, C.; Lv, W.; Ali, S.; Boateng, B.; Chen, W.; Wei, Z.; Feng, C.; Ahmed, J.; Goodenough, J. B.; He, W., A Highly-Efficient Composite Separator with Strong Ligand Interaction for High-Temperature Lithium-Ion Batteries. *ChemElectroChem* **2018,** *5*, 2722-2728.

157. Scrosati, B.; Hassoun, J.; Sun, Y.-K., Lithium-Ion Batteries. A look into the Future. *Energy & Environmental Science* **2011,** *4*, 3287-3295.

158. Li, Q.; Chen, J.; Fan, L.; Kong, X.; Lu, Y., Progress in Electrolytes for Rechargeable Li-Based Batteries and Beyond. *Green Energy & Environment 1* **2016,** *1*, 18-42.

159. Xu, K., Nonaqueous Liquid Electrolytes for Lithium-Based Rechargeable Batteries. *Chemical Reviews* **2004,** *104*, 4303-4417.

160. Wang, A.; Kadam, S.; Li, H.; Shi, S.; Qi, Y., Review on Modeling of the Anode Solid Electrolyte Interphase (SEI) for Lithium-Ion Batteries. *npj Computational Materials* **2018,** *4*, 15.

161. Agubra, V. A.; Fergus, J. W., The Formation and Stability of the Solid Electrolyte Interface on the Graphite Anode. *Journal of Power Sources* **2014,** *268*, 153-162.

162. Wang, S.; Liu, Q.; Zhao, C.; Lv, F.; Qin, X.; Du, H.; Kang, F.; Li, B., Advances in Understanding Materials for Rechargeable Lithium Batteries by Atomic Force Microscopy. *Energy & Environmental Materials* **2018,** *1*, 28-40.

163. Gebresilassie Eshetu, G.; Armand, M.; Scrosati, B.; Passerini, S., Energy Storage Materials Synthesized from Ionic Liquids. *Angewandte Chemie, International Edition* **2014,** *53*, 13342-13359.

164. Oltean, G.; Plylahan, N.; Ihrfors, C.; Wei, W.; Xu, C.; Edstroem, K.; Nyholm, L.; Johansson, P.; Gustafsson, T., Towards Li-Ion Batteries Operating at 80 °C: Ionic Liquid Versus Conventional Liquid Electrolytes. *Batteries* **2018,** *4*, 2/1-2/6.

165. Savilov, S. V.; Artemova, A. O.; Ivanov, A. S.; Shen, Z.; Aldoshin, S. M.; Lunin, V. V., Stability of a High-Voltage Ionic Liquid with a Substituted Piperidinium Cation and a TFSI Anion, Promising for Electrochemical Applications. *Mendeleev Communications* **2016,** *26*, 240-242.

166. Zhang, Z. Z., Sheng Shui, Materials, Technologies, and New Trends. In *Rechargeable Batteries* Springer International Publishing: 2015.

167. Zhang, Z.; Hu, L.; Wu, H.; Weng, W.; Koh, M.; Redfern, P. C.; Curtiss, L. A.; Amine, K., Fluorinated Electrolytes for 5 V Lithium-Ion Battery Chemistry. *Energy & Environmental Science* **2013,** *6*, 1806-1810.

168. Smart, M. C.; Ratnakumar, B. V.; Ryan-Mowrey, V. S.; Surampudi, S.; Prakash, G. K. S.; Hu, J.; Cheung, I., Improved Performance of Lithium-Ion Cells with the Use of Fluorinated Carbonate-Based Electrolytes. *Journal of Power Sources* **2003,** *119-121*, 359-367.

169. Suo, L.; Xue, W.; Gobet, M.; Greenbaum, S. G.; Wang, C.; Chen, Y.; Yang, W.; Li, Y.; Li, J., Fluorine-Donating Electrolytes Enable Highly Reversible 5-V-Class Li Metal Batteries. *Proceedings of the National Academy of Sciences* **2018,** *115*, 1156.

170. Shao, N.; Sun, X.-G.; Dai, S.; Jiang, D.-e., Electrochemical Windows of Sulfone-Based Electrolytes for High-Voltage Li-Ion Batteries. *Journal of Physical Chemistry B* **2011,** *115*, 12120-12125.

171. Sun, X.-G.; Austen Angell, C., New Sulfone Electrolytes. *Solid State Ionics* **2004,** *175*, 257-260.

172. Abouimrane, A.; Belharouak, I.; Amine, K., Sulfone-Based Electrolytes for High-Voltage Li-Ion Batteries. *Electrochemistry Communications* **2009,** *11*, 1073-1076.

173. Ren, X.; Chen, S.; Lee, H.; Mei, D.; Engelhard, M. H.; Burton, S. D.; Zhao, W.; Zheng, J.; Li, Q.; Ding, M. S.; Schroeder, M.; Alvarado, J.; Xu, K.; Meng, Y. S.; Liu, J.; Zhang, J.-G.; Xu, W., Localized High-Concentration Sulfone Electrolytes for High-Efficiency Lithium-Metal Batteries. *Chem* **2018,** *4*, 1877-1892.

174. Xie, J.-D.; Liu, W.-J.; Li, C.; Patra, J.; Gandomi, Y. A.; Dong, Q.-F.; Chang, J.-K., Superior Coulombic Efficiency of Lithium Anodes for Rechargeable Batteries Utilizing High-Concentration Ether Electrolytes. *Electrochimica Acta* **2019,** *319*, 625-633.

175. Matsumiya, M.; Suda, S.; Tsunashima, K.; Sugiya, M.; Kishioka, S.-y.; Matsuura, H., Electrochemical Behaviors of Multivalent Complexes in Room Temperature Ionic Liquids Based on Quaternary Phosphonium Cations. *Journal of Electroanalytical Chemistry* **2008,** *622*, 129-135.

176. Blundell, R. K.; Licence, P., Quaternary Ammonium and Phosphonium Vased Ionic Liquids: A Comparison of Common Anions. *Physical Chemistry Chemical Physics* **2014,** *16*, 15278-15288.

177. Pinson, M. B.; Bazant, M. Z., Theory of SEI Formation in Rechargeable Batteries: Capacity Fade, Accelerated Aging and Lifetime Prediction. *Journal of the Electrochemical Society* **2012,** *160*, A243-A250.

178. Lin, X.; Navailles, L.; Nallet, F.; Grinstaff, M. W., Influence of Phosphonium Alkyl Substituents on the Rheological and Thermal Properties of Phosphonium-PAA-Based Supramolecular Polymeric Assemblies. *Macromolecules* **2012,** *45*, 9500-9506.

179. Xue, Z.; Qin, L.; Jiang, J.; Mu, T.; Gao, G., Thermal, Electrochemical and Radiolytic Stabilities of Ionic Liquids. *Physical Chemistry Chemical Physics* **2018,** *20*, 8382-8402.

180. Wanger, T. C., The Lithium Future—Resources, Recycling, and the Environment. *Conservation Letters* **2011,** *4*, 202-206.

181. Flexer, V.; Baspineiro, C. F.; Galli, C. I., Lithium Recovery from Brines: A Vital Raw Material for Green Energies with a Potential Environmental Impact in its Mining and Processing. *Science of the Total Environment* **2018,** *639*, 1188-1204.

182. Agusdinata, D. B.; Liu, W.; Eakin, H.; Romero, H., Socio-Environmental Impacts of Lithium Mineral Extraction: Towards a Research Agenda. *Environmental Research Letters* **2018,** *13*, 123001.

183. Heredia, F.; Martinez, A. L.; Surraco Urtubey, V., The Importance of Lithium for Achieving a Low-Carbon Future: Overview of the Lithium Extraction in the 'Lithium Triangle'. *Journal of Energy & Natural Resources Law* **2020,** *38*, 213-236.

184. Lee, S.-Y.; Yong, H. H.; Lee, Y. J.; Kim, S. K.; Ahn, S., Two-Cation Competition in Ionic-Liquid-Modified Electrolytes for Lithium Ion Batteries. *The Journal of Physical Chemistry B* **2005,** *109*, 13663-13667.

185. Yamada, Y.; Wang, J.; Ko, S.; Watanabe, E.; Yamada, A., Advances and Issues in Developing Salt-Concentrated Battery Electrolytes. *Nature Energy* **2019,** *4*, 269-280.

186. Santos, M. C. G.; Silva, G. G.; Santamaría, R.; Ortega, P. F. R.; Lavall, R. L., Discussion on Operational Voltage and Efficiencies of Ionic-Liquid-Based Electrochemical Capacitors. *The Journal of Physical Chemistry C* **2019,** *123*, 8541-8549.

187. Ortega, P. F. R.; Santos, G. A. d.; Trigueiro, J. P. C.; Silva, G. G.; Quintanal, N.; Blanco, C.; Lavall, R. L.; Santamaría, R., Insights on the Behavior of Imidazolium Ionic Liquids as Electrolytes in Carbon-Based Supercapacitors: An Applied Electrochemical Approach. *The Journal of Physical Chemistry C* **2020,** *124*, 15818-15830.

188. Pal, B.; Yang, S.; Ramesh, S.; Thangadurai, V.; Jose, R., Electrolyte Selection for Supercapacitive Devices: A Critical Review. *Nanoscale Advances* **2019,** *1*, 3807-3835.

189. Lane, G. H., Electrochemical Reduction Mechanisms and Stabilities of Some Cation Types Used in Ionic Liquids and Other Organic Salts. *Electrochimica Acta* **2012,** *83*, 513-528.

190. Wishart, J. F., Radiation and Radical Chemistry of Ionic Liquids for Energy Applications. In Ionic Liquids: Current State and Future Directions. American Chemical Society: Washington, DC, 2017; Vol. 1250.

191. Tian, Y.-H.; Goff, G. S.; Runde, W. H.; Batista, E. R., Exploring Electrochemical Windows of Room-Temperature Ionic Liquids: A Computational Study. *The Journal of Physical Chemistry B* **2012,** *116*, 11943-11952.

192. Shkrob, I. A.; Wishart, J. F., Charge Trapping in Imidazolium Ionic Liquids. *The Journal of Physical Chemistry B* **2009,** *113*, 5582-5592.

Curriculum Vitae